

Spring 5-2014

# A Study of Scattering Characteristics for Micro-scale Rough Surface

Yonghee Won

*Rose-Hulman Institute of Technology*, wony@rose-hulman.edu

Follow this and additional works at: [http://scholar.rose-hulman.edu/optics\\_grad\\_theses](http://scholar.rose-hulman.edu/optics_grad_theses)



Part of the [Optics Commons](#), and the [Other Physics Commons](#)

---

## Recommended Citation

Won, Yonghee, "A Study of Scattering Characteristics for Micro-scale Rough Surface" (2014). *Graduate Theses - Physics and Optical Engineering*. Paper 3.

This Thesis is brought to you for free and open access by the Graduate Theses at Rose-Hulman Scholar. It has been accepted for inclusion in Graduate Theses - Physics and Optical Engineering by an authorized administrator of Rose-Hulman Scholar. For more information, please contact [bernier@rose-hulman.edu](mailto:bernier@rose-hulman.edu).

**A STUDY OF SCATTERING CHARACTERISTICS  
FOR MICRO-SCALE ROUGH SURFACES**

A Thesis

Submitted to the Faculty

of

Rose-Hulman Institute of Technology

by

Yonghee Won

In Partial Fulfillment of the Requirements for the Degree

of

Master of Science in Optical Engineering

May 2014

© 2014 Yonghee Won



**ROSE-HULMAN INSTITUTE OF TECHNOLOGY**

**Final Examination Report**

Yonghee Won

Name

Optical Engineering

Graduate Major

Thesis Title A Study of Scattering Characteristics for Micro-Scale Rough Surfaces

**DATE OF EXAM:**

May 13, 2014

**EXAMINATION COMMITTEE:**

	<b>Thesis Advisory Committee</b>	<b>Department</b>
Thesis Advisor:	Robert Bunch	PHOE
	Zachariah Chambers	ME
	Paul Leisher	PHOE
	Wonjong Joo	
	Kibom Kim	

**PASSED**     X    

**FAILED**

## **ABSTRACT**

Yonghee Won

M.S.O.E

Rose-Hulman Institute of Technology

May 2014

A Study of Scattering Characteristics for Micro-scale Rough Surface

Dr. Robert M. Bunch

Defining the scatter characteristics of surfaces plays an important role in various technology industries such as the semiconductor, automobile, and military industries. Scattering can be used to inspect products for problems created during the manufacturing process and to generate the specifications for engineers. In particular, scattering measurement systems and models have been developed to define the surface properties of a wide variety of materials used in manufacturing. However, most previous research has been focused on very smooth surfaces as a nano-scale roughness. The research in this paper uses the Bidirectional Reflectance Distribution Function (BRDF) and focuses on defining the scattering properties of micro-scale rough and textured surfaces for three different incident angles. Also, the parameters of ABg and Harvey-Shack models are obtained for input into optical design software.

## ACKNOWLEDGEMENTS

There have been a number of people throughout my career as a graduate student who have helped me, inspired me, and generally made it all worthwhile. To these people, I give my heartfelt thanks.

First, I would like to thank my advisor, Robert M. Bunch, for the opportunity to work with you on my thesis project while pursuing my master's degree. It was truly an honor for me. Your insight, enthusiasm, and dedication to me were very helpful in my studies. I have thoroughly enjoyed all of our discussions, both educational and technical, and am grateful that your door was always open. I could not have finished this study without you. I also thank Brant Potter in Valeo Sylvania for supporting my thesis

I would also like to thank Professor Wonjong Joo and Kibom Kim, my advisors in Seoultech. They have always believed in me and inspired me that I can do everything.

I thank the Physics and Optical Engineering and the Graduate Departments at Rose-Hulman Institute of Technology, and Manufacturing Systems and Design Engineering Department at Seoultech for their support and the opportunities that they have given to me.

I would like to offer thanks to my friend, Benjamin Hall, for helping my life in the United States. I also thank my Korean friends in the same class.

Finally, I would like to thank my family and girlfriend for their support and encouragement. I could not have finished my thesis project if they did not support and believe in me.

## TABLE OF CONTENTS

### CONTENTS

<b>LIST OF FIGURES .....</b>	<b>iii</b>
<b>LIST OF TABLES .....</b>	<b>ix</b>
<b>LIST OF ABBREVIATIONS .....</b>	<b>x</b>
<b>LIST OF SYMBOLS .....</b>	<b>xi</b>
<b>1. INTRODUCTION.....</b>	<b>1</b>
<b>2. THEORY .....</b>	<b>4</b>
2.1 Radiometry.....	4
2.1.1 Solid angle .....	4
2.1.2 Elements of Radiometry .....	6
2.2 Reflection of light .....	10
2.3 Bidirectional Reflectance Distribution Function (BRDF) .....	11
2.4 Useful theories to measure surface scattering.....	14
<b>3. MEASUREMENT SYSTEM DESIGN.....</b>	<b>17</b>
3.1 Layout of the BRDF measurement system .....	17
3.2 Goniometer configuration.....	19
3.3 Light source .....	21
3.4 Detection system.....	22
3.5 Lock-in Amplifier detection .....	24
3.6 Data acquisition using LabView .....	26

3.6.1 Operation procedure.....	28
<b>4. RESULTS AND DISCUSSIONS.....</b>	<b>32</b>
4.1 Surface roughness measurement of samples.....	32
4.2 Scattering effects with respect to the incident angle.....	35
4.3 Scattering effects with respect to the surface roughness .....	45
4.4 Comparison of the BRDF with the ABg model to obtain the Harvey-Shack model.....	54
4.5 Error analysis .....	62
<b>5. CONCLUSIONS.....</b>	<b>64</b>
<b>6. FUTURE WORKS.....</b>	<b>67</b>
<b>LIST OF REFERENCES.....</b>	<b>68</b>
<b>APPENDICES.....</b>	<b>71</b>
<b>Appendix A.....</b>	<b>72</b>
<b>Appendix B.....</b>	<b>74</b>
<b>Appendix C.....</b>	<b>81</b>
<b>Appendix D.....</b>	<b>91</b>

## LIST OF FIGURES

<b>Figure 1</b>	Schematic of solid angle (a) Theoretical definition of solid angle, (b) Solid angle of our System.....	5
<b>Figure 2</b>	Two types of radiant flux density (a) Irradiance, (b) Radiant exitance	6
<b>Figure 3</b>	Definition of surface area for radiance (a) Differential solid angle $d\Omega$ , (b) Projected area .....	8
<b>Figure 4</b>	Characteristics of different reflections .....	10
<b>Figure 5</b>	Geometry for the definition of BRDF [9].....	11
<b>Figure 6</b>	Derivation of the Harvey-Shack model .....	14
<b>Figure 7</b>	Example of ABg model of the sample A at the $60^\circ$ incident angle ...	16
<b>Figure 8</b>	Setup for the BRDF measurement [19] .....	17
<b>Figure 9</b>	Schematic of incident and scattering angles.....	18
<b>Figure 10</b>	Modified BRDF measurement apparatus .....	20
<b>Figure 11</b>	Linearity curve of Photomultiplier tube (PMT) .....	23
<b>Figure 12</b>	Modification of laser power after chopper .....	24
<b>Figure 13</b>	The front of the Lock-in Amplifier.....	25
<b>Figure 14</b>	Schematic of NI USB-6009 (a) Terminal of USB-6009 (b) Referenced Single-Ended Voltage signal .....	26
<b>Figure 15</b>	The GUI for measuring the scattered voltage and the BRDF.....	29
<b>Figure 16</b>	The GUI for drawing the BRDF graphs .....	31



<b>Figure 17</b> Comparison of the BRDF with the three different incident angles in Sample A (1 $\mu\text{m}$ ).....	37
<b>Figure 18</b> Comparison of the BRDF with the three different incident angles, expressed by the log-log plot for Sample A (1 $\mu\text{m}$ ).....	37
<b>Figure 19</b> Comparison of the BRDF with the three different incident angles in Sample B (3 $\mu\text{m}$ ).....	38
<b>Figure 20</b> Comparison of the BRDF with the three different incident angles, expressed by the log-log plot for Sample B (3 $\mu\text{m}$ ).....	38
<b>Figure 21</b> Comparison of the BRDF with the three different incident angles in Sample C (6 $\mu\text{m}$ ).....	41
<b>Figure 22</b> Comparison of the BRDF with the three different incident angles, expressed by the log-log plot for Sample C (6 $\mu\text{m}$ ). $\theta_0$ for 45° incident angle was modified to 46° and $\theta_0$ for 60° incident angle was modified to 64°.....	41
<b>Figure 23</b> Comparison of the BRDF with the three different incident angles in Sample D (12 $\mu\text{m}$ ).....	42
<b>Figure 24</b> Comparison of the BRDF with the three different incident angles, expressed by the log-log plot for Sample D (12 $\mu\text{m}$ ). $\theta_0$ for 45° incident angle was modified to 52° and $\theta_0$ for 60° incident angle was modified to 70°.....	42
<b>Figure 25</b> Comparison of the BRDF with the three different incident angles in Sample E (19 $\mu\text{m}$ ).....	43

<b>Figure 26</b> Comparison of the BRDF with the three different incident angles, expressed by the log-log plot for Sample E (19 $\mu\text{m}$ ). $\theta_0$ for 45° incident angle was modified to 52° and $\theta_0$ for 60° incident angle was modified to 70°.....	43
<b>Figure 27</b> Comparison of the BRDF for samples with a wide range of surface roughness for a 15° incident angle .....	45
<b>Figure 28</b> Comparison of the BRDF for samples with a wide range of surface roughness for (a) 45° and (b) 60° incident angles .....	47
<b>Figure 29</b> Comparison of the BRDF for samples with a wide range of surface roughness, expressed by the log-log plot for 15° incident angle .....	49
<b>Figure 30</b> Comparison of the BRDF for samples with a wide range of surface roughness, expressed by the log-log plot for 45° incident angle .....	50
<b>Figure 31</b> Comparison of the BRDF for samples with a wide range of surface roughness, expressed by the log-log plot for 60° incident angle .....	51
<b>Figure 32</b> Relationship between surface roughness and peak scattering angle. Samples D and E have the same peak angle. ....	53
<b>Figure 33</b> Comparison between the BRDF and the ABg model of Sample C at the 60° incident angle.....	55
<b>Figure 34</b> Comparison between the BRDF and ABg model of Sample D at the 60° incident angle.....	56
<b>Figure 35</b> Comparison between the BRDF and ABg model of Sample E at the 60° incident angle.....	57

<b>Figure 36</b> Comparison of the ABg model in (a) Sample A, (b) Sample D, (c) Sample E .....	60
<b>Figure 37</b> Comparison of the Harvey-Shack with the ABg model of Sample E at the 60° incident angle .....	61
<b>Figure 38</b> GUI programming source for calculating the BRDF using the scattered voltage.....	74
<b>Figure 39</b> Sub VI for measuring the incident voltage and the scattered voltage .....	75
<b>Figure 40</b> Sub VI for $\beta - \beta_0$ .....	76
<b>Figure 41</b> Programming source for drawing the BRDF graphs using the text file. (Part A) .....	77
<b>Figure 42</b> Programming source for drawing the BRDF graphs using the text file. (Part B) .....	78
<b>Figure 43</b> Front panel of GUI for the BRDF .....	79
<b>Figure 44</b> Front panel of GUI for drawing the BRDF graphs.....	80
<b>Figure 45</b> The ABg model of Sample A at the 15° incident angle.....	81
<b>Figure 46</b> The ABg model of Sample A at the (a) 45° and (b) 60° incident angles .....	82
<b>Figure 47</b> The ABg model of Sample B at the (a) 15° and (b) 45° incident angles .....	83
<b>Figure 48</b> The ABg model of Sample B at the 60° incident angle.....	84
<b>Figure 49</b> The ABg model of Sample C at the 15° incident angle.....	85

<b>Figure 50</b> The ABg model of Sample C at the (a) 45° and (b) 60° incident angles. The specular angles are shifted to 46° and 64° respectively .....	86
<b>Figure 51</b> The ABg model of Sample D at the 15° incident angle.....	87
<b>Figure 52</b> The ABg model of Sample D at the (a) 45° and (b) 60° incident angles. The specular angles are shifted to 46° and 64° respectively. ....	88
<b>Figure 53</b> The ABg model of Sample E at the 15° incident angle .....	89
<b>Figure 54</b> The ABg model of Sample E at the (a) 45° and (b) 60° incident angles. The specular angles are shifted to 46° and 64° respectively. ....	90
<b>Figure 55</b> Comparison of the Harvey-Shack model with the ABg model of Sample A at the 15° incident angle .....	91
<b>Figure 56</b> Comparison of the Harvey-Shack model with the ABg model of Sample A at the (a) 45° and (b) 60° incident angles .....	92
<b>Figure 57</b> Comparison of the Harvey-Shack model with the ABg model of Sample B at the (a) 15° and (b) 45° incident angles.....	93
<b>Figure 58</b> Comparison of the Harvey-Shack model with the ABg model of Sample B at the 60° incident angle .....	94
<b>Figure 59</b> Comparison of the Harvey-Shack model with the ABg model of Sample C at the (a) 15° and (b) 45° incident angles.....	95
<b>Figure 60</b> Comparison of the Harvey-shack model with the ABg model of Sample C at the 60° incident angle .....	96
<b>Figure 61</b> Comparison of the Harvey-Shack model with the ABg model of Sample D at the (a) 15° and (b) 45° incident angles .....	97

**Figure 62** Comparison of the Harvey-Shack model with the ABg model of  
Sample D at the 60° incident angle ..... 98

**Figure 63** Comparison of the Harvey-Shack model with the ABg model of  
Sample E at the (a) 15° and (b) 45° incident angles ..... 99

**Figure 64** Comparison of the Harvey-Shack model with the ABg model of  
Sample E at the 60° incident angle..... 100

## LIST OF TABLES

<b>Table 1</b>	The graphical user interface for the system .....	28
<b>Table 2</b>	Graphical surface roughness and RMS roughness of 5 experimental samples.....	34
<b>Table 3</b>	The peak value of BRDF with respect to all experimental variations	52
<b>Table 4</b>	The average error of BRDF data for all samples and incident angles	63
<b>Table 5</b>	Optical density value for each ND filter. The percent error is with respect to the given OD filter value. ....	72
<b>Table 6</b>	Optical density value for two ND filters. The percent error is with respect to the given OD filter value. ....	73

**LIST OF ABBREVIATIONS**

AI	Analog Input
AO	Analog Output
BSDF	Bidirectional Scatter Distribution Function
BRDF	Bidirectional Reflectance Distribution Function
BTDF	Bidirectional Transmittance Distribution Function
DAQ	Data Acquisition-Unit
GND	Ground Input
PSD	Phase Sensitive Detector
RMS	Root Mean Square

## LIST OF SYMBOLS

### Mathematical Symbols

$Q$	Radiant Energy
$E_e$	Irradiance
$M_e$	Radiant Exitance
$L$	Radiance

### Greek Symbols

$\Omega$	Solid Angle
$\Phi$	Radiant Flux
$\sigma_{rms}$	RMS Roughness
$\lambda$	Wavelength of Light Source

### English Symbols

$sr$	Steradian
$V$	Voltage





## 1. INTRODUCTION

The relationship between surface roughness and light scattering plays an important role in many areas of technology and industry. Surface scattering measurement is widely used in quality inspection or process control to check appearance and limit roughness, contamination, and other defects. It is proving to be particularly useful in the semiconductor industry to inspect during device manufacture and in the automobile industry to analyze the surface characteristics of head and tail lamps. Aside from the above applications, surface scatter measurement is widely applied in various industry fields.

### Background

If light is incident upon a mirror-like surface, the reflected light is concentrated in the specular reflection direction which is determined by the law of reflection. Another idealized surface shows the perfectly diffuse reflection which is called Lambertian surface. A more realistic surface shows both the specular and diffuse reflection.

Earlier investigation into surface scattering was focused on the smooth surface; roughness ( $\sigma_{rms}$ ) is less than the wavelength ( $\lambda$ ) of the light source. Of course, some researchers studied scattering characteristics of rough surface [1], [2], [3], [4]. However, there is little scattering data for micro-scale rough and random surfaces. Also, they were

explained using difficult mathematical methods. A micro-scale rough surface is defined when the roughness is much larger than the wavelength ( $\sigma_{rms} \gg \lambda$ ) in this thesis.

This thesis used the Bidirectional Reflectance Distribution Function (BRDF) to quantify scattered light from a micro-scale rough surface [5]. Because the mathematical definition of the BRDF is easy to understand, and because the BRDF variations are familiar to the user, it is defined as a quantity which completely describes the scattering properties of a given surface and is commonly used to define the surface characteristics. Also, it can be used to generate scattering specifications that enable designers, manufacturers, and users of optics to communicate and check requirements. The ABg and the Harvey-Shack models are also developed to predict scattering characteristics of surfaces, and these models can be defined by the measured BRDF data.

### Thesis contents

This research studies the micro-scale rough surface characteristics using light scattering measurement because scatter specifications of micro-scale rough surface are needed in various industries and in optical design software. It uses the BRDF, the ABg model and the Harvey-Shack scattering models which are the most common models to measure scattering. We used five different micro-scale samples which were coated with aluminum metal with a range of roughness from around 1 to 19  $\mu\text{m}$ . The scattering measurement was operated at different incident angles (15°, 45°, and 60°).

The primary objective of this study is to check whether or not the theories for a smooth surface can be applied to a micro-scale rough surface and to define the surface characteristics of micro-scale rough and random surfaces. Also, by using the measured scattering data, we want to derive the scatter parameters for use in optical design software such as Zemax, Code V, and ASAP.

## 2. THEORY

### 2.1 Radiometry

Before describing the Bidirectional Reflectance Distribution Function (BRDF), some radiometric terms have to be defined and discussed in order to understand it. Radiometry is the quantitative analysis of the flux transfer of light. There are four fundamental quantities in radiometry: radiant flux, irradiance, radiant intensity, and radiance. This thesis focuses on irradiance and radiance in radiometry [6], [7].

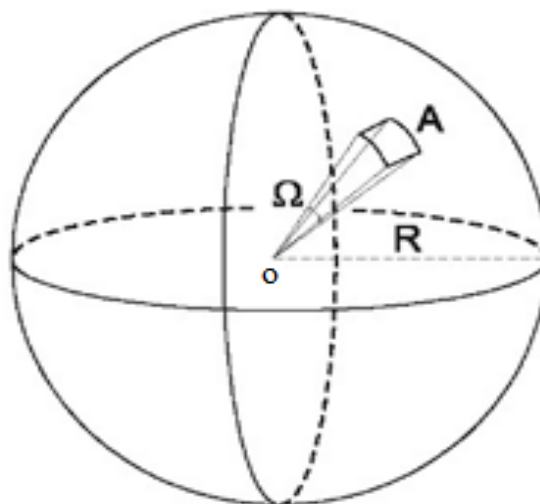
#### 2.1.1 Solid angle

Before defining the basic radiometric quantities, solid angle will be examined. The solid angle  $d\Omega$  is defined as a quantity that subtends a surface  $dA$  at a distance  $R$ ,  $d\Omega = dA/R^2$ . The solid angle equals the projection area  $A$  on the sphere divided by the square of the radius of the sphere as illustrated in Figure 1 (a). It has a given unit, called the *steradian*, abbreviated *sr*.

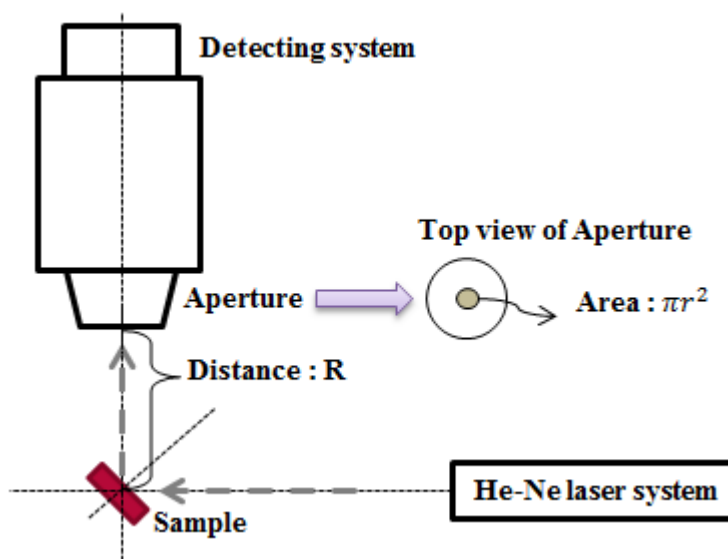
The solid angle is described as

$$\Omega = \frac{\pi r^2}{R^2} \quad (1)$$

In our case, surface area  $A = \pi r^2$  is the aperture area of the detecting system radius  $r$  and  $R$  indicates the distance from the sample surface to the aperture. Figure 1 (b) shows the solid angle in our system.



(a)



(b)

**Figure 1** Schematic of solid angle (a) Theoretical definition of solid angle, (b) Solid angle of our System

### 2.1.2 Elements of Radiometry

#### Irradiance

In general, light is described in terms of *radiant energy* which is indicated by  $Q(t)$  and measured in Joules (J). For easy understanding, it can be thought of as how much light has been emitted or received from a surface at a time  $t$ . The main quantity used in radiometry is *optical power*, indicating the rate of light energy emitted or absorbed by an object. This quantity of time-variation, called *radiant flux*, is measured in Joules per second ( $\text{J} \cdot \text{s}^{-1}$  or Watts (W)). Flux is denoted by  $\Phi(t)$ :

$$\Phi(t) = \frac{dQ(t)}{dt} \quad (2)$$

The light received (or emitted) by an object is distributed over the surface of the object. This is important for reflectance measurements because the light reflected from its surface depends on surface position and characteristics of the surface of an object.

Formally, light flux arriving from any direction above the surface is referred to as the *irradiance* falling on the surface,  $E_e = d\Phi_e/dA$ , as shown in Figure 2 (a). On the other hand, the light leaving the surface is referred to as *radiant exitance*,  $M_e = d\Phi_e/dA$ , as shown in Figure 2 (b).

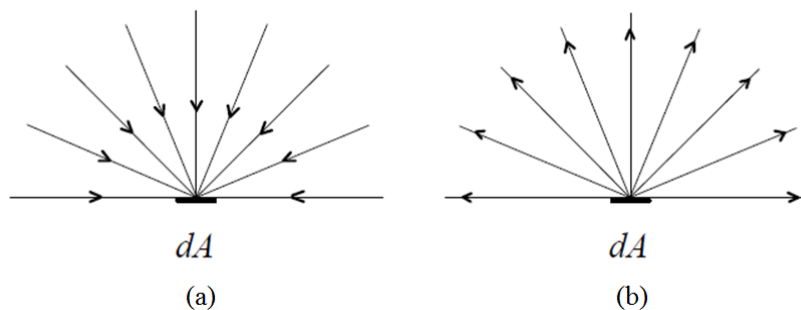


**Figure 2** Two types of radiant flux density (a) Irradiance, (b) Radiant exitance

Irradiance, the density of radiant flux, is denoted by  $E(\bar{p})$  as a function of surface position  $\bar{p}$ . Because the number of photons received at a single point is commonly zero, we cannot represent the amount of light received at a single point on a surface. Therefore, we can say that irradiance is the spatial derivative of flux. Irradiance can be expressed as

$$E(\bar{p}) = \frac{d\Phi}{dA} \quad (3)$$

where  $dA$  indicates the differential area surrounding the specified surface. Irradiance is power per unit surface area ( $W \cdot m^{-2}$ ), incident on a surface.



### Radiance

The light arriving at or emitting from an object depends not only on the given direction but also on the surface position of an object. *Radiance* is defined as a measure of light flux emitted from a surface in a specific direction and is represented as a function of surface position ( $\vec{p}$ ) and specific direction ( $\vec{d}$ ), and is denoted by  $L$  (or  $L(\vec{p}, \vec{d})$ ).

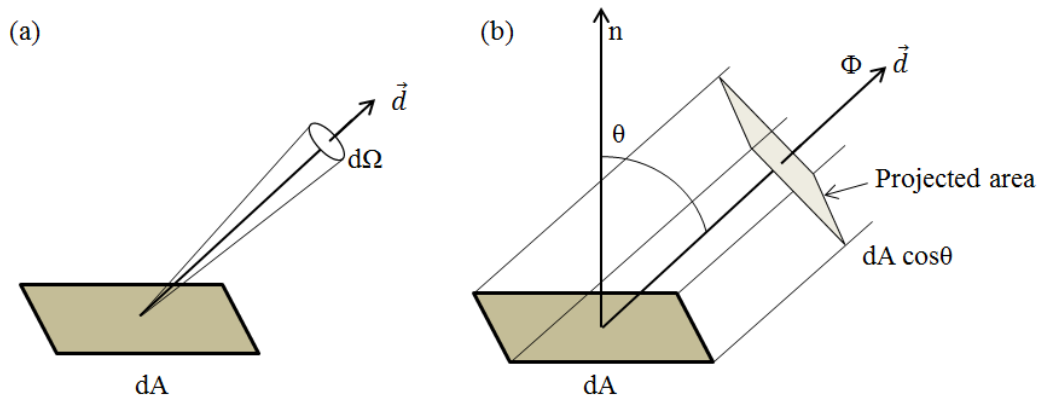


**Figure 3** Definition of surface area for radiance (a) Differential solid angle  $d\Omega$ , (b) Projected area

For a formal definition of radiance, we can imagine of an amount light passing through a narrow cone with its apex at a surface and this cone has a differential solid angle  $d\Omega$  as shown in Figure 3 (a). We should also understand the concept of projected area which is defined as  $dA \cos\theta$ , where  $\theta$  is the angle between normal direction of surface and the direction  $\vec{d}$ , as shown in Figure 3 (b).

Using the above explanations, radiance can be denoted as

$$L = \frac{d^2\Phi}{[dA(d\Omega\cos\theta)]} \quad (4)$$

where  $\Phi$  is the radiant flux and  $d\Omega\cos\theta$  is called the projected solid angle at area  $dA$ . It is expressed by power per solid angle (*steradian*) per surface area ( $W \cdot sr^{-1} \cdot m^{-2}$ ).

To summarize, radiance is the power from the source per area in a specific direction. In contrast, irradiance is the power per surface area; it is not related to a direction. Second, they have different units: radiance ( $W \cdot sr^{-1} \cdot m^{-2}$ ) and irradiance ( $W \cdot m^{-2}$ ). Finally, irradiance indicates light received at the surface of an object, and radiance indicates light emitted from the surface.

## 2.2 Reflection of light

The law of reflection indicates that the angle of reflected light will be equal to the angle of incident light, which is called the *specular reflection*. Both angles are measured with respect to the normal of the surface. In this thesis, the geometrical specular angle is used when the incident angle is equal to the specular reflection angle.

The reflection depends on the characteristics of the surface as illustrated in Figure 4. For smooth surfaces such as a mirror, the light illuminates the surface and is reflected in a specular direction following the law of reflection as shown in Figure 4 (a). A Lambertian surface results in perfectly diffuse reflection. In this case, light will be reflected from the surface equally in all directions as shown in Figure 4 (b). On the other hand, most physically realistic surfaces display some mixed reflection as shown in Figure 4 (c). There exist both the coherent components such as a specular reflection and the incoherent components like a diffuse scattering [8].

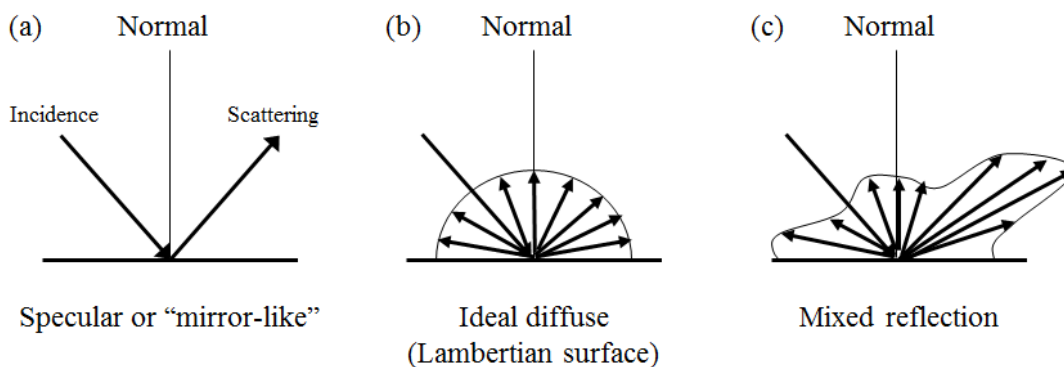


**Figure 4** Characteristics of different reflections

### 2.3 Bidirectional Reflectance Distribution Function (BRDF)

The bidirectional scatter distribution function (BSDF) depends on four parameters (or four dimensional functions): two input and two output angles in the spherical coordinate system. When the scattering of the transmitted beam is measured, it is called BTDF (Bidirectional Transmittance Distribution Function), and when the scattering of the reflected beam is measured, it is called BRDF (Bidirectional Reflectance Distribution Function). These are merely subsets of the BSDF. Among these different types of scattering measurement methods, this thesis focuses on the BRDF, which is widely used to quantify the roughness of optical surfaces with very high sensitivity.

The derivation and notation for BRDF was first developed by F.E. Nicodemus et al. (1977), who made an effort to examine the problem of measuring and defining the reflectance of optics that are neither completely diffuse nor completely specular. Figure 5 shows the geometry definition of BRDF, and subscripts  $i$  and  $s$  are used to indicate incident and scattered values, respectively.

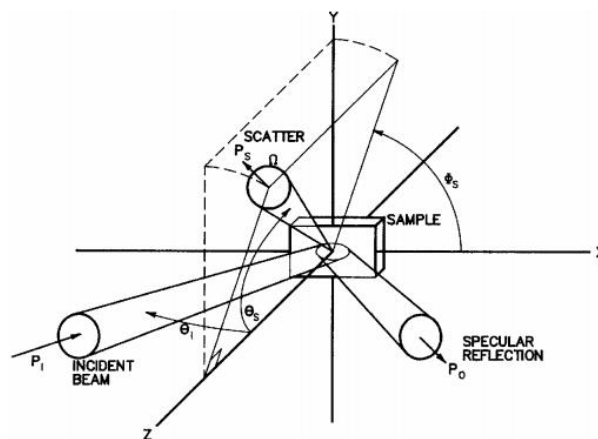


**Figure 5** Geometry for the definition of BRDF [9]

Nicodemus further simplified his derivation and theory through some assumptions because it is fairly complicated and restricted. He assumed that the beam has a uniform cross-section, that the reflected surface is isotropic, and that all scattered light comes from the surface and none from the bulk.

The BRDF can be defined in radiometric terms as the scattered radiance divided by incident irradiance. Radiometric terms have already been explained. The irradiance received at surface is the light flux per surface area, and the radiance scattered from surface is the scattered light flux through solid angle  $\Omega$  per surface area per projected solid angle, which is the solid angle multiplied by  $\cos\theta_s$ .

Thus, the BRDF can be denoted as

$$BRDF = f(\theta_s, \phi_s; \theta_i, \phi_i) = \frac{\text{differential radiance}}{\text{differential irradiance}} \cong \frac{dP_s/d\Omega}{P_i \cos\theta_s} \cong \frac{P_s/\Omega}{P_i \cos\theta_s} \quad (5)$$

where  $P_s$  and  $P_i$  are the scattered and incident measured power respectively, and  $\theta_s$  is the scattered angle from the normal to the surface. The BRDF value can be derived for all incident angles and all scatter angles. Note that the BRDF has units of *inverse steradians* and, depending on the  $P_s$  and  $\Omega$  quantities, can take on either very large or very small values. For instance, the power ratio between  $P_s$  and  $P_i$  is almost 1 if the specular reflection is measured from a mirror. Away from the specular reflection, however, the power ratio is very small.

Of course, the differential form of the BRDF equation is more precise; it is only approximated when measurements are taken with a finite-diameter aperture. However, the approximation is very good when the flux density is reasonably constant over the measuring aperture but can be very poor when using a large aperture to measure focused specular beams.

The assumptions from Nicodemus about uniform cross section and isotropic surfaces are not completely valid in most measurement situations. For instance, the incident laser beam has a Gaussian intensity cross section instead of a uniform cross section. There is no truly isotropic surface, and some bulk scatter exists at even good reflectors. However, it still makes sense to specify and measure the quantities of Equation 5 [10].

In this research, the scattered and incident powers used to derive BRDF quantity have to be modified by their voltages because the signal voltage from detector is proportional to the power for all incident and scattered angles. Thus, the above BRDF equation is modified

$$BRDF \cong \frac{P_s/\Omega}{P_i \cos \theta_s} \cong \frac{V_s/\Omega}{V_i \cos \theta_s} \quad (6)$$

where  $V_s$  and  $V_i$  denote the scattered and incident voltages, respectively. It has the same units as *inverse steradians*.

## 2.4 Useful theories to measure surface scattering

The two scattering models used in this thesis are called the Harvey-Shack model and the ABg model [11]. The Harvey-Shack model was developed to predict scattering characteristics of surfaces. The importance of the Harvey-Shack model is that the BRDF depends on the difference between the sine of the specular angle and the sine of the scattered angle rays, but it does not depend on the incident angle. This means that the BRDF in this model is defined as a linear-shift invariant function [12], [13]. Figure 6 shows the geometry used in the derivation of this model.

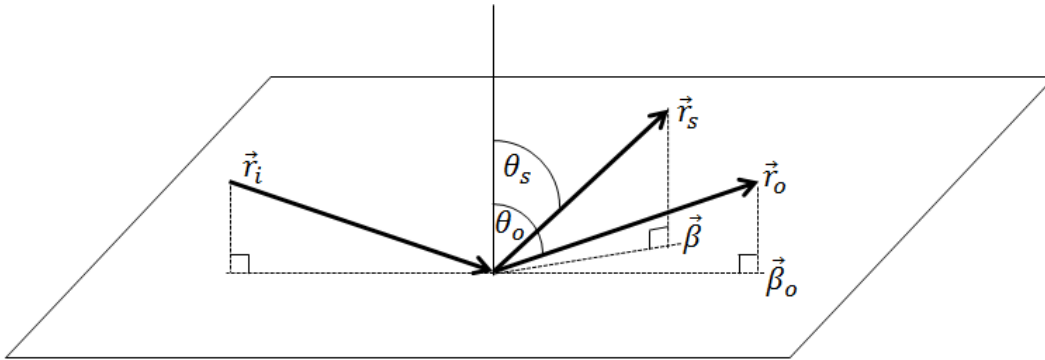


**Figure 6** Derivation of the Harvey-Shack model

The projected vectors of scattered and specular directions are

$$\vec{\beta} = \vec{r}_s \sin(\theta_s); \vec{\beta}_o = \vec{r}_o \sin(\theta_o) \quad (7)$$

where  $\vec{\beta}$  indicates the vector in scatter reflection direction, and  $\vec{\beta}_o$  indicates the vector in the specular reflection direction.  $\theta_s$  and  $\theta_o$  are the scatter angle and specular angle, respectively, and are measured relative to the surface normal. The vector  $\vec{r}_i$  is the

incident light ray,  $\vec{r}_o$  is the specular ray, and  $\vec{r}_s$  is the vector of the scattering ray. All of these vectors are unit vectors.  $\vec{\beta}$  and  $\vec{\beta}_o$  are taken in the incident plane. So, the BRDF can be described as a function of  $|\vec{\beta} - \vec{\beta}_o|$  which can also express the specular range effectively.

The Harvey-Shack scattering model is defined as

$$BRDF_{Harvey-Shack}(\vec{\beta}, \vec{\beta}_o) = b_0 \left( 1 + \left( \frac{\beta - \beta_o}{L} \right)^2 \right)^{S/2} \quad (8)$$

where  $b_0$  is the specular peak value of BRDF when  $\beta - \beta_o$  is zero,  $L$  is the knee of the BRDF curve, and  $S$  is the slope of a logarithmic BRDF plot [14].

The ABg scattering model is defined as

$$BRDF_{ABg}(\vec{\beta}, \vec{\beta}_o) = \frac{A}{B + |\vec{\beta} - \vec{\beta}_o|^g} \quad (9)$$

In the ABg scattering model,  $A$  is the amplitude parameter determined at the specular direction, where  $A/B$  is the specular peak of BRDF.  $B$  is the roll-off (knee) parameter, which determines when the function transitions into an exponential decay form. The parameter  $g$  determines the slope on a logarithmic plot of BRDF as shown in Figure 7. If a slope is zero, it indicates the Lambertian surface which is the perfectly diffuse reflection [15].



In Equations 8 and 9, the unit vectors  $\vec{r}_o$  and  $\vec{r}_s$  of  $|\vec{\beta} - \vec{\beta}_o|$  are not considered because a simpler model is enough to get the BRDF value. The ABg scattering model is very similar to the Harvey-Shack model derived empirically from measurement, and is widely used to measure scatter from an isotropic surface. These models are wavelength invariant. Also both models can be transformed into each other [16]:

$$\text{ABg} \rightarrow \text{Harvey - Shack} : b_0 = \frac{A}{B}; \quad S = -g; \quad L = B^{\frac{1}{g}}$$

$$\text{Harvey - Shack} \rightarrow \text{ABg} : A = Bb_0; \quad B = L^{-S}; \quad g = -S$$

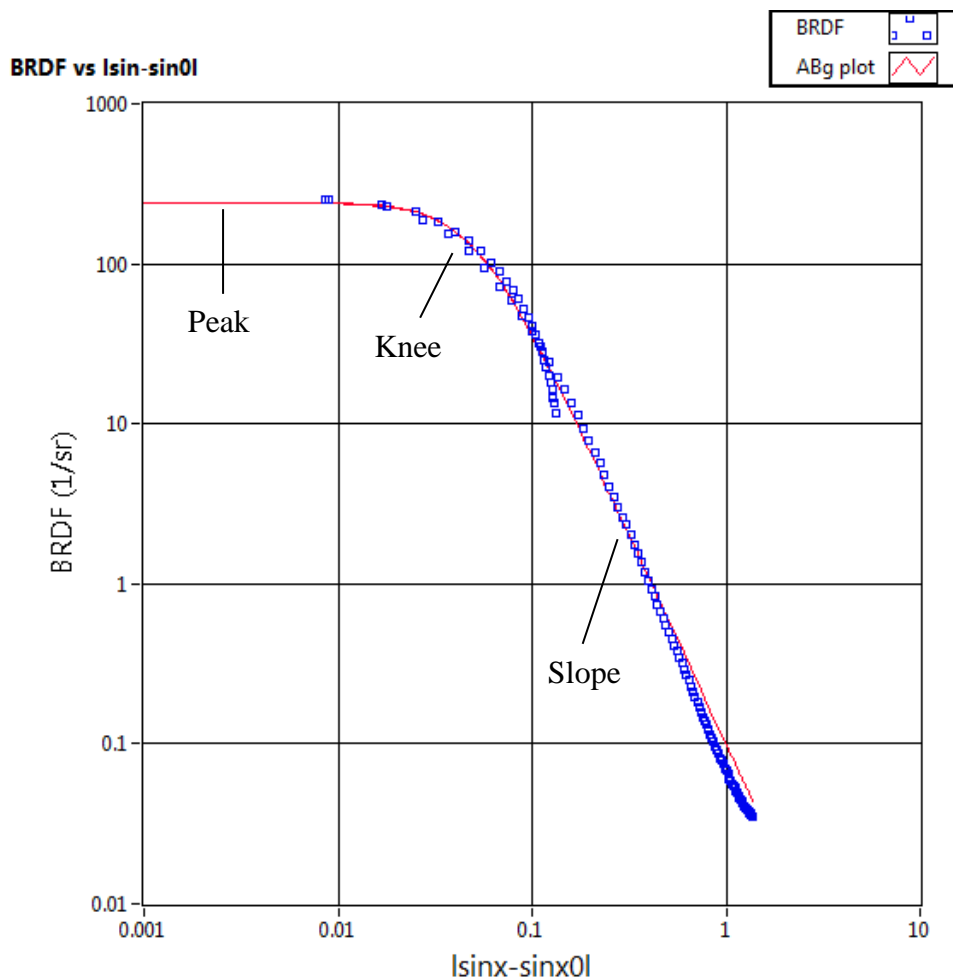


**Figure 7** Example of ABg model of the sample A at the 60° incident angle

### 3. MEASUREMENT SYSTEM DESIGN

#### 3.1 Layout of the BRDF measurement system

There are numerous models for BRDF measurement systems in the literature [17], [18]. All systems are based on some type of goniometer. For a basic scattering measurement system, the goniometer was configured as shown in Figure 8 [19]. Note that in this configuration the detector arm has one degree of rotational freedom. This implies that beam alignment to the axis of rotation is critical.

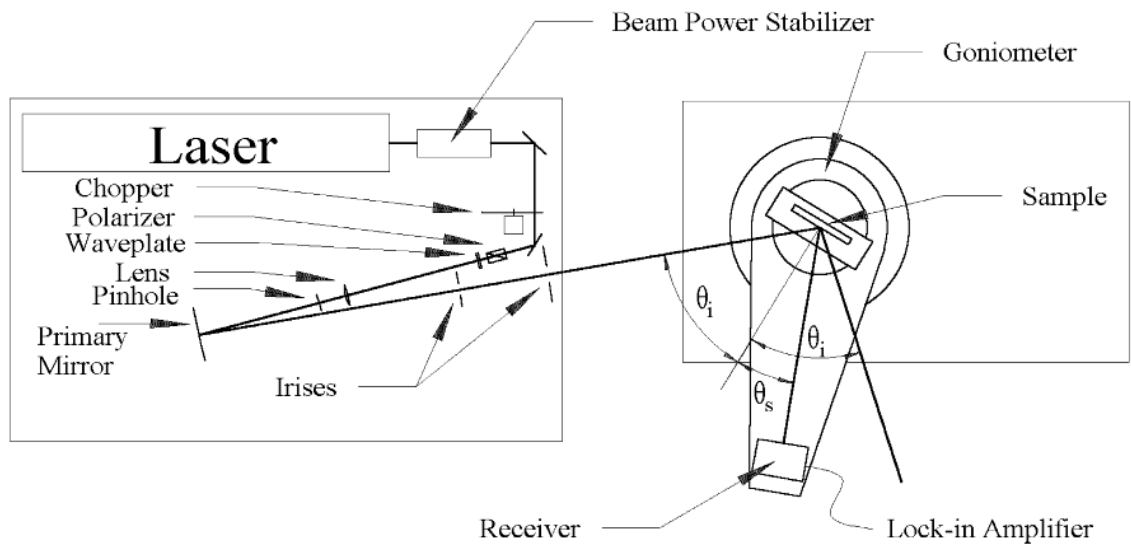


**Figure 8** Setup for the BRDF measurement [19]

The incident angle and scattering angles of the BRDF experiment are defined as shown in Figure 9. Through this figure, zero degree indicates the normal to the sample surface and the incident angle is between normal axis and the light source. The specular

angle has the same angle value as the incident angle; however, the direction is opposite. Also, the scattering angle was defined by two types based on the specular angle: back and front scattering angle. The scattering angle has a negative sign as well as positive because the scattering angle was regarded as a negative sign from the normal of the sample to the light source axis.

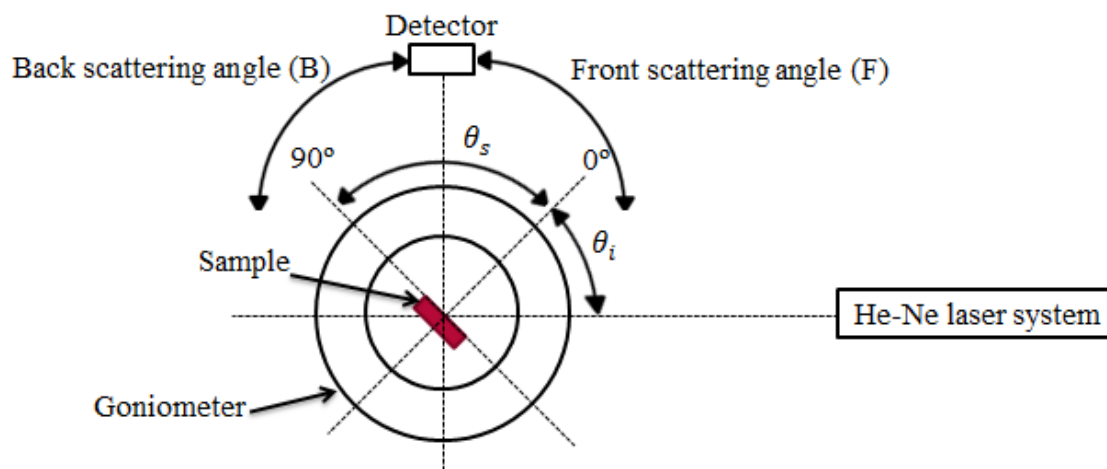


**Figure 9** Schematic of incident and scattering angles

### 3.2 Goniometer configuration

For this thesis, the earlier scattering goniometer design was modified as shown in Figure 10. This scatterometer essentially suggests a well-expanded laser beam on the sample surface at a well-defined incident angle. The light source arrangement of the former design was modified in order to obtain another degree of freedom (DOF) in pointing the incident beam to assist with ease of alignment and to enable measurement of a wider range of scattering angles. Angular resolution of this goniometer is  $0.5^\circ$ . The total angular range of the scattering angle is different depending on the specified incident angle because the rotation angle of the detector arm was limited by the mechanical mounts. At  $45^\circ$  and  $60^\circ$  incident angles, the ranges are from  $-16^\circ$  to  $90^\circ$  and from  $-31^\circ$  to  $90^\circ$ , respectively. On the other hand, at  $15^\circ$  of incident, there are no negative angles possible. The range of scattering angle is only between  $+14^\circ$  and  $90^\circ$  because the laser source is blocked by the goniometer arm.

In the scattering goniometer apparatus, the sample mount has three degrees of rotational freedom and three degrees of translational freedom for the sample in order to locate the sample at the center of the goniometer and in the correct position to the laser source. At first, three translational DOF allow the sample surface to be located at the rotation axis of the photomultiplier tube (PMT) detector and the light source is illuminated. Next, three rotational DOF allow the sample to be reoriented and realigned for a specific angle of incidence. The PMT detector and sample mount have to be

equipped to enable us to confirm the alignment of the sample. The same location of the sample has to be observed at any scattering angle.

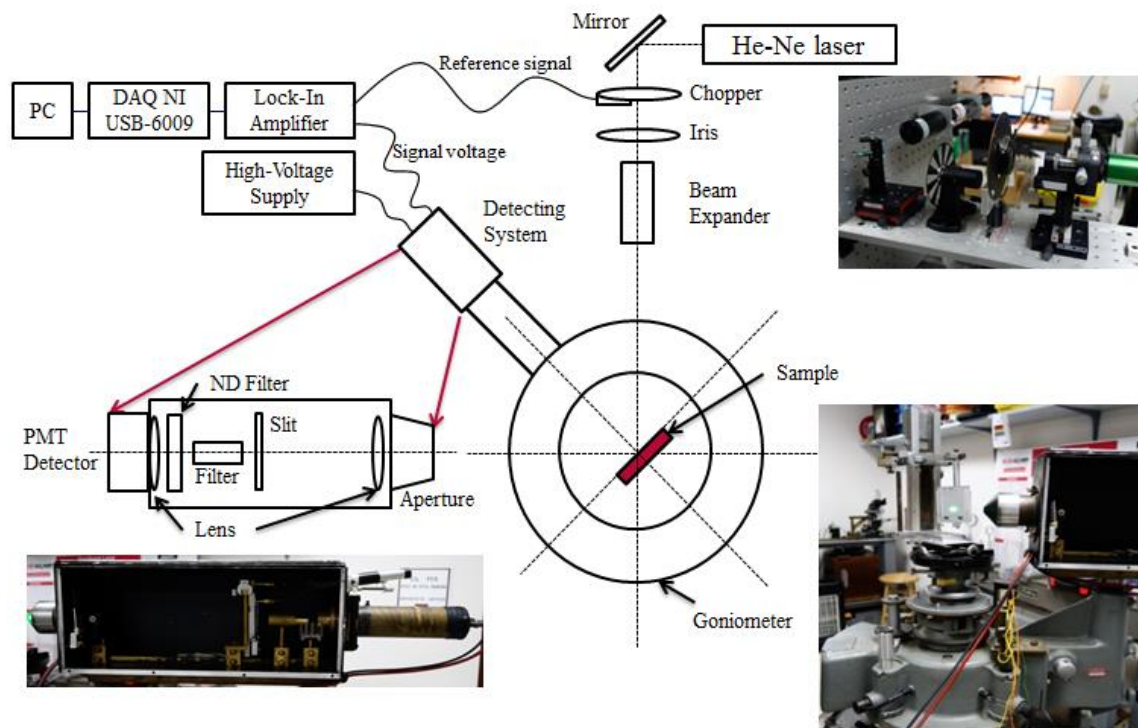


**Figure 10** Modified BRDF measurement apparatus

### 3.3 Light source

In the BRDF system, many different types of lasers can be used. We chose a green He-Ne laser (540 nm wavelength) because it is easy to handle and supplies sufficient optical power for measuring. It also has enhanced scattering power for the range of structures which we were examining over the smaller wavelength than a red He-Ne laser (630 nm wavelength).

The green He-Ne laser source was chopped in order to reduce both optical and electronic noise. The chopper alternates between blocking the incident laser and allowing it to pass. On the bottom of the chopper is an LED and photo-detector pair, which sends the square-wave signal at frequency ( $f_c$ ) to the lock-in amplifier as a reference signal. The details of lock-in will be explained in section 3.5. An iris is used to prevent the stray light of the laser from reaching the PMT detector. The spot size on the sample surface is precisely determined by the expander and can be conveniently adjusted by changing the location of the expander. The expander with a spatial filter pinhole enables us to get more and easily scatter light to the detector. Through this equipment, our system provides a well-collimated laser beam on the sample surface at a well-defined incident angle.

### 3.4 Detection system

There are many kinds of detectors for measuring scattering light such as silicon detectors, avalanche photodiode detectors, camera detectors and so on. In our experiment, we chose the photomultiplier tube (PMT) detector. It is an extremely sensitive detector of light in the ultraviolet, visible, and near-infrared ranges of the electromagnetic spectrum. Also it is useful for detecting very low scattering signals because this detector can amplify a signal without any other instruments.

An image system in the detector arm ensures that the illuminated point on the sample surface is projected to the slit in the detector system, and the scattering light passing through the slit is collected by the lens and detected by the PMT detector. This detector is connected to the lock-in amplifier. Through the lock-in amplifier, we can determine the scattered voltage with respect to each angle.

The scattered light flux from the sample surface varies by several orders of magnitude over the angular range to be measured. Hence, the linearity of the PMT was measured using several neutral density (ND) filters to vary incident flux. The calibration regarding the neutral density filter can be found in the Appendix A. The resulting linearity curve of our PMT detector is shown in Figure 11, and indicates a deviation of less than 1% over a range of three orders of magnitude of the incident flux [12].

Since the neutral density filter factor is the power of ten for the attenuation, using the ND filter for plotting already means taking the logarithm. Hence, to investigate the linearity of a tube over a large range of light intensities, the plot should be drawn as the logarithm of the output peak voltage versus ND filter [20].

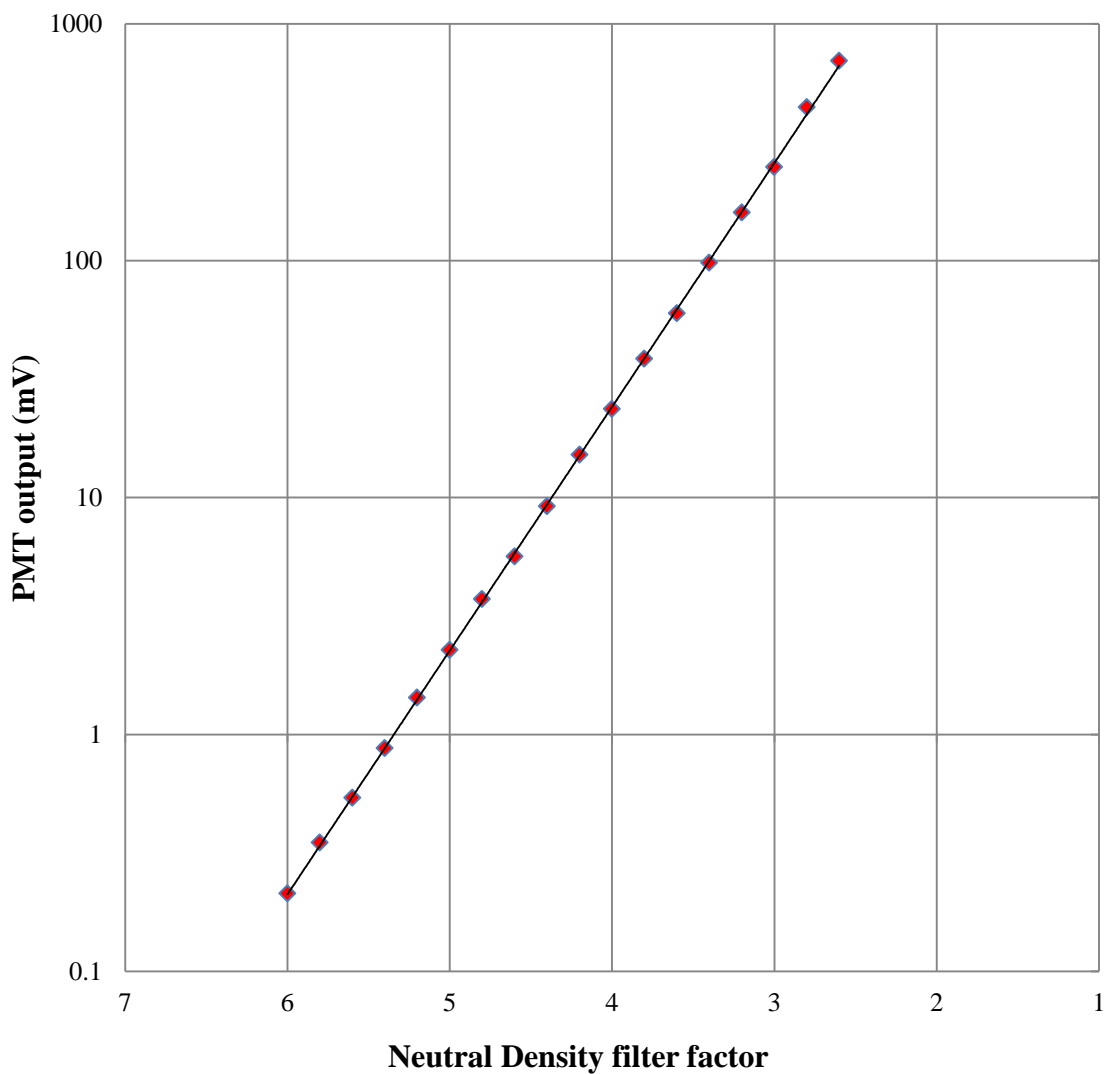


**Figure 11** Linearity curve of Photomultiplier tube (PMT)



### 3.5 Lock-in Amplifier detection

A lock-in amplifier is a device which is useful for measuring the amplitude and phase of a signal. In most cases of the BRDF measurement, the reduction of the scattering signal to noise ratio is very important because signal filtration and subsequent amplification can still negatively affect this ratio. The lock-in amplifier is a device created to surmount this problem by modulating the input signal by a reference signal  $f_c$  (created by a chopper), and upon signal detection, measuring only the voltage input modulated by  $f_c$  [21]. The phase sensitive detector (PSD), in general, is the most important part of the lock-in amplifier because it is in charge of separating the signal which we want to examine from the background noise.

The modification of laser power passing through the chopper is shown in Figure 12. Laser power is changed into a square wave signal by the chopper. The lock-in amplifier then converts this square wave signal into sinusoidal signal form, for use in processing the input signal.

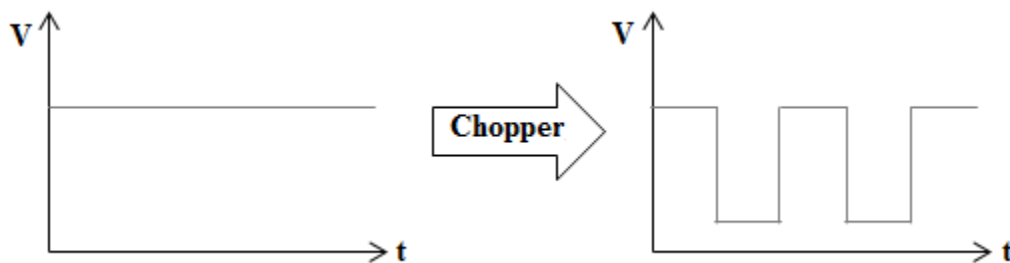


**Figure 12** Modification of laser power after chopper

As illustrated in Figure 13, the scattered signal from the PMT detector is connected to the signal input, and the reference signal is connected to the reference input. For measuring scattered voltage, the Channel 1 display is changed from X to R; R is phase dependent. The Channel 2 display is also changed from Y to  $\theta$ . When  $\theta$  value becomes a steady state, the voltage value is measured. Measured scattered voltage from the PMT detector is shown on the Channel 1 display on the front of the lock-in amplifier, and the unit depends on the sensitivity values.

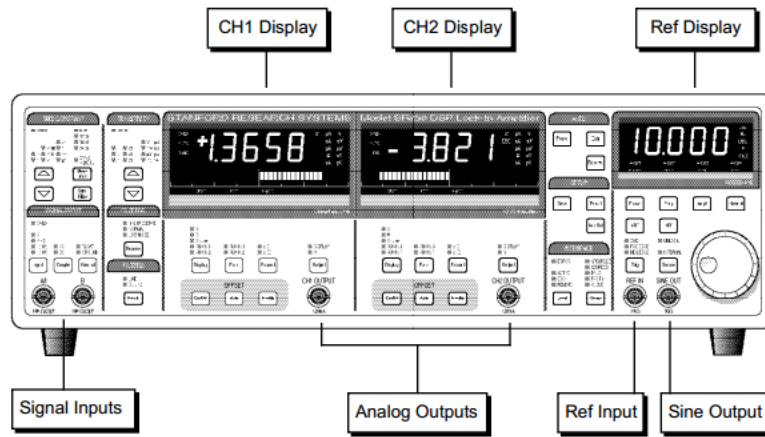


**Figure 13** The front of the Lock-in Amplifier

The voltage, CH1 OUTPUT provides an analog output proportional to the Display (R) value. This output is determined by

$$\text{CH1 OUTPUT (V)} = \left( \frac{\text{Scattered value in Display}}{\text{Sensitivity}} - \text{offset} \right) \times \text{Expand} \times 10V \quad (10)$$

where the sensitivity, offset, and expand values can be chosen with respect to the experiment situation [22]. The output range is normally  $\pm 10$  V. This output is connected to the Data Acquisition-unit (DAQ) device to record voltages proportional to the scattered power leading to the BRDF.

### 3.6 Data acquisition using LabView

The Data Acquisition-Unit (DAQ) NI USB-6009 was used to interface the lock-in amplifier with a computer to record the scattered voltage [23]. This device has analog inputs (AI), analog output (AO), and digital I/O lines. For this thesis, one analog input and ground are needed.

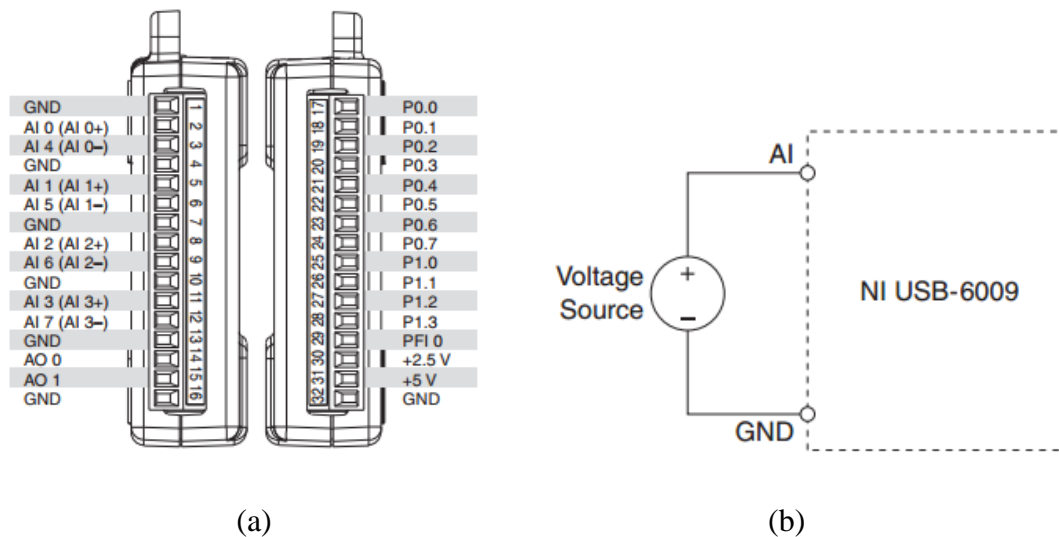


**Figure 14** Schematic of NI USB-6009 (a) Terminal of USB-6009 (b) Referenced Single-Ended Voltage signal

Figure 14 (a) shows the information for all pinouts of the DAQ device. Analog input signal names are listed as single-ended analog, AI x, or differential analog, AI <x +/->. Ground (GND) is the reference point for the single-ended analog input measurements. For single-ended measurements, each signal is fed to an analog input voltage channel. For differential measurements, AI 0 and AI 4 indicate the positive and

negative inputs respectively and both inputs indicate the differential analog input channel 0. The following positive and negative input signals (AI1 & 5, 2 & 6, and 3 & 7 as shown in Figure 14) also indicate differential analog input channels: channel 1, 2, and 3, respectively.

To record the scattered voltage, the CH1 output from the lock-in and DAQ device were connected using a single cable. One side of the cable is separated into positive and negative output. The positive output is connected to AI 0 (2<sup>nd</sup> pin) and the negative output is connected to GND (1<sup>st</sup> pin). This measurement method is called the referenced single-ended (RSE) as shown in Figure 14 (b). With the DAQ device connected to the computer, this scattered voltage, which is proportional to the BRDF, can be recorded using a customized software program written in LabView.

The software for measuring the BRDF was programmed using the visual programming software LabView. Through the software, we can reduce the experiment time and gain a more precise value for the BRDF. The graphical user interface (GUI) of the system is explained in Table 1.

The manual measuring mode used in this program means that the goniometer must be manually set to a scattering angle prior to data collection. The input parameters are needed in order to calculate the BRDF. Output parameters can be separated into two types: System Output and Calculated Output. The system output parameters can be

defined directly through the detector and DAQ device. The calculated parameters can be achieved from the system parameters.

**Table 1** The graphical user interface for the system

<b>Mode</b>	Manual measuring
<b>Input parameter</b>	Incident and scattered angles: $\theta_i$ and $\theta_s$ Radius of Aperture: $r$ Distance from the sample surface to the aperture: $R$ Incident beam voltage: $V_i$
<b>System Output</b>	Scattered beam voltage: $V_s$ Error value for each scattered voltage
<b>Calculated Output</b>	BRDF Graphs: BRDF vs Scattering angle and BRDF vs $ \sin \theta - \sin \theta_o $

### 3.6.1 Operation procedure

Figure 15 shows the LabView program used to determine the scattered voltage and to calculate the BRDF. This program is repeatedly operated to record the scattered voltage from each scattering angle and to tabulate and record the BRDF. Future plans for this instrument include adding an input to automatically read the scattering angle and automating the goniometer rotation with a stepper motor.

In the first step, the incident voltage ( $V_i$ ) of the beam is measured using the program. After that, the input parameters including the measured incident voltage are filled in using the program's GUI interface. The DAQ device is also controlled by the System Setting GUI of the program.

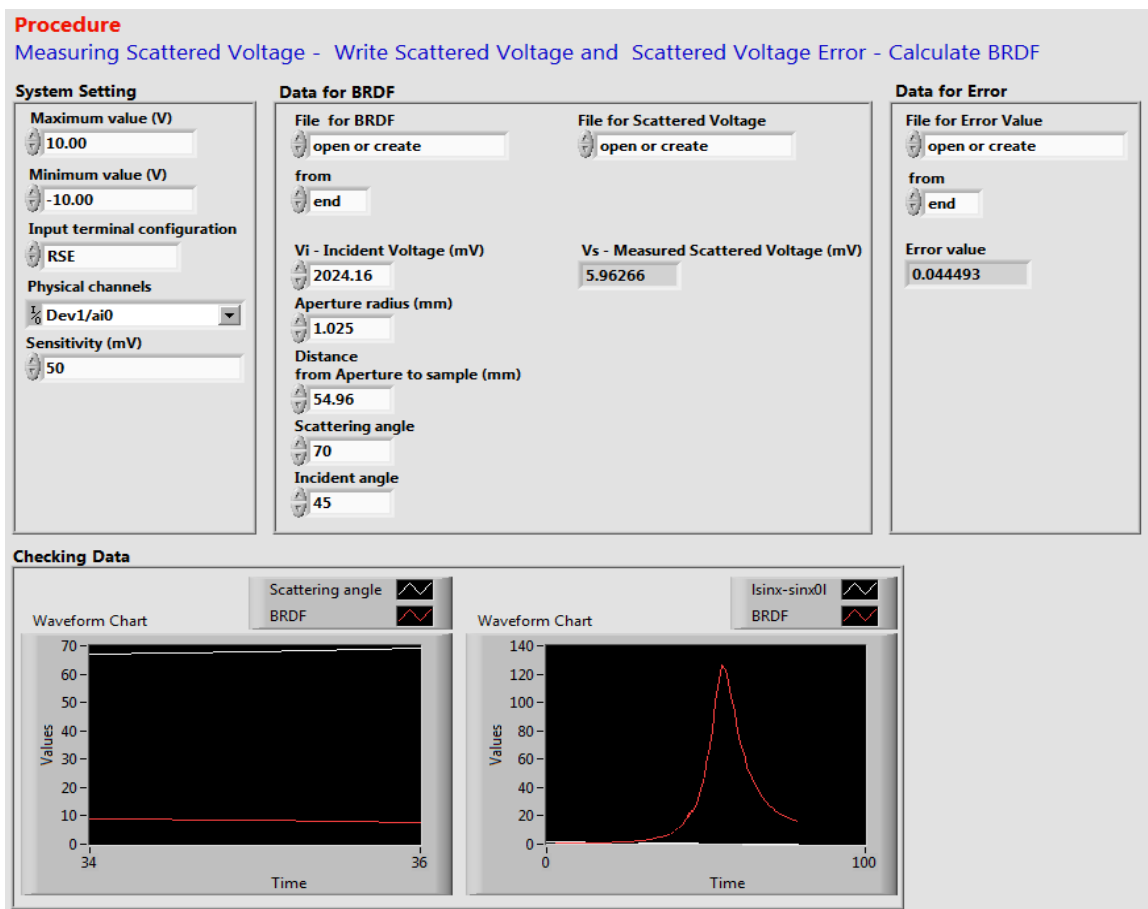


**Figure 15** The GUI for measuring the scattered voltage and the BRDF

In order for the GUI  $V_s$  display to show the same voltage reading as the lock-in display, the CH1 value must be modified. This was done using Equation 11 so that it

would be easy to compare  $V_s$  with the value on the lock-in amplifier and make it easy to check when some errors occurred.

$$\text{Scattered value in Display} = \left( \frac{\text{CH1 OUTPUT}}{\text{Expand} \times 10\text{V}} + \text{offset} \right) \times \text{Sensitivity} \quad (11)$$

Note that the expand and offset values are not considered because those values were not used in the experiment.

In this program, the scattered voltage is measured 20 times to record the average voltage and error value with respect to each scattering angle because the scattered voltage from the detector is slightly unstable. Twenty samples were chosen experimentally to average fluctuations in the output signal from the lock-in amplifier. This data, the average value, and error value, is accumulated and stored in a simple text file. Simultaneously, the program also calculates the BRDF using the measured average scattered voltage.

In other words, we can get the scattered voltage and the BRDF together with respect to the changing of each scattering angle. The BRDF, scattering angle, and  $|\vec{\beta} - \vec{\beta}_o|$  are also recorded in a second text file. By using this second text file, we can draw the BRDF graph through another LabView program as shown in Figure 16. This process provides two sets of redundant data but preserves the original data of the scattering voltage as a function of angle if needed for further analysis.

In Figure 16, the left graph displays the calculated BRDF with respect to the scattering angle, and displays the data in linear (x-axis) and logarithmic (y-axis) plot. The

right graph displays the BRDF with respect to the  $|\vec{\beta} - \vec{\beta}_o|$ , which is log-log plot. Also, the ABg model can be displayed with the BRDF plot after the A, B, and g values are derived using Excel program. More details regarding the algorithm and functions about the GUI programs can be found in Appendix B.

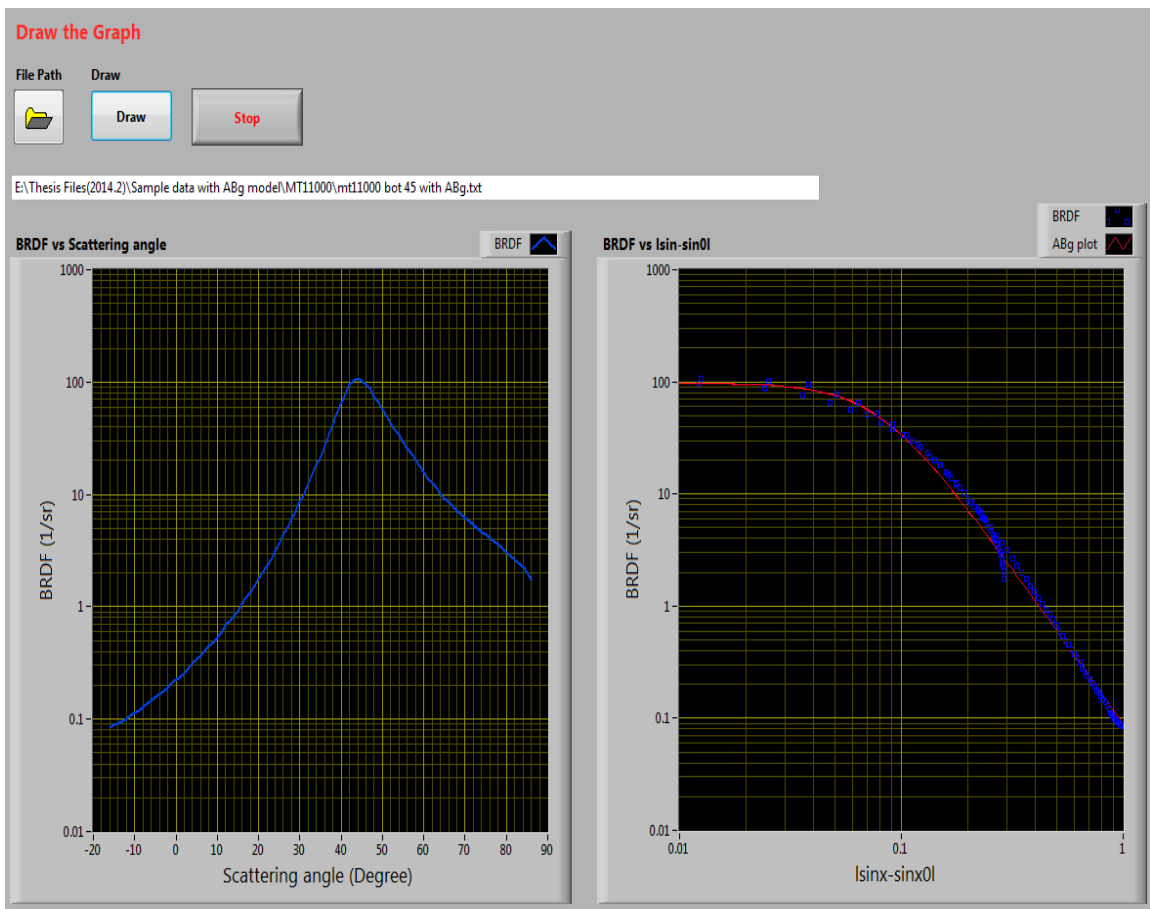


**Figure 16** The GUI for drawing the BRDF graphs



## 4. RESULTS AND DISCUSSIONS

The scattered light measured from a variety of surface roughness and angles of incidence are reported in this chapter. The results from the experiments are then compared with the ABg model and the Harvey-Shack model.

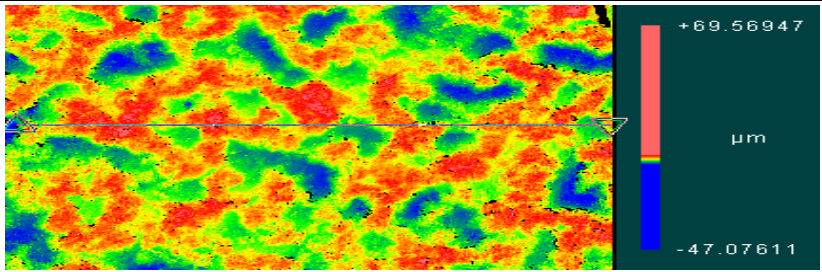
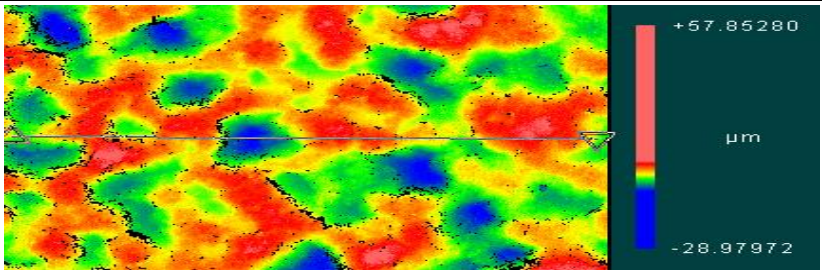
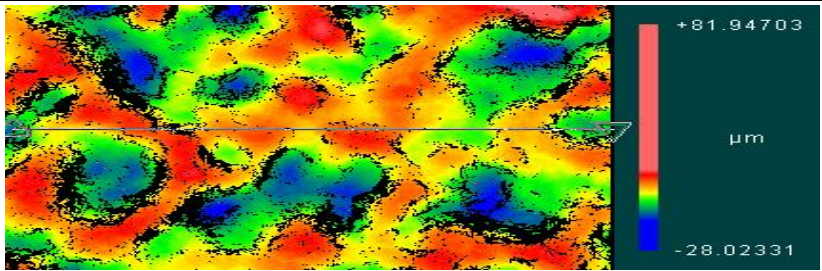
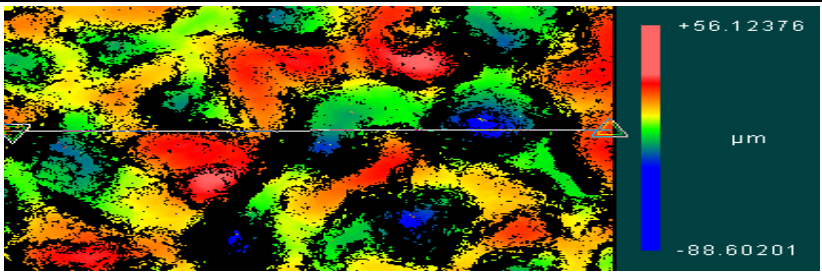
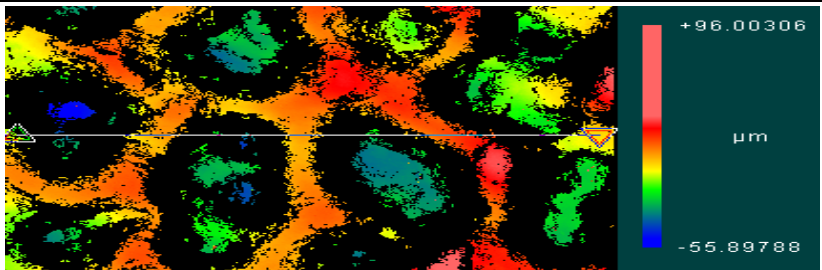
### 4.1 Surface roughness measurement of samples

To define the scattering characteristics of experimental samples, the roughness and surface structure were analyzed. In this study, ZYGO NEWVIEW™ equipment was used to analyze the three dimensional surface structure of five samples. It provides graphic images and high resolution numerical analysis to accurately characterize the surface structure of the samples without contacting the surfaces [24]. This device uses scanning white light interferometry to image and measure the micro structure and topography of surfaces in three dimensions. A wide variety of surfaces can be measured.

Five experimental samples in this thesis are coated by aluminum metal and have different Root Mean Square (RMS) roughness as a micro-size. The RMS roughness is measured 10 times at different positions of sample surface because only a small area of each sample is measured. By using measured RMS roughness, the average value and error are defined. Table 2 shows the graphical surface structure and RMS roughness of the experimental samples.

As can be seen from the Table 2, these five samples have random surface structure regardless of RMS roughness value. The right position of the figures in Table 2 indicates the range of peak value in each sample. These figures explain that the experimental samples are not uniform in structure because the depth and height of the texture in each sample is very different. These results predict that the cross-section profile of samples will fluctuate greatly. Because of the random surface structure, the error value of each RMS roughness is larger. Also, the surface structure is larger when the RMS roughness value is increased. Through the roughness data, we can predict how the scattering characteristics are affected by the surface roughness.

**Table 2** Graphical surface roughness and RMS roughness of 5 experimental samples

Sample	RMS Roughness	Graphical surface
A	$1 \pm 0.13 \mu\text{m}$	
B	$3 \pm 0.33 \mu\text{m}$	
C	$6 \pm 0.52 \mu\text{m}$	
D	$12 \pm 1.9 \mu\text{m}$	
E	$19 \pm 2.4 \mu\text{m}$	

#### 4.2 Scattering effects with respect to the incident angle

In this section, the relationship between the BRDF and the incident angle is discussed using experimental data for five different samples. The scattering angle at the peak of the BRDF should be the specular angle. However, it was observed that in some samples there was a difference between the specular angle predicted from geometrical optics and the peak scattering angle. In general, as surface roughness increases the scattering angle peak shifts to larger angles away from the specular direction.

Two types of graphs are shown for each sample comparing the scattering data for three different incident angles (15°, 45°, and 60°). One shows the BRDF with respect to the scattering angle and the other graph is a plot of BRDF with respect to  $|\vec{\beta} - \vec{\beta}_o|$ . To observe the specular region precisely, the second BRDF graph is expressed as a log-log plot. When the detector is moving to the specular angle region, the x-coordinate is smaller and vice versa. The reason for using this kind of graph is to better illustrate the scattering effects close to the specular region. This specular region is the flat part of the log-log plot.

The peak of the scattering BRDF of sample A (roughness of 1  $\mu\text{m}$ ) is well defined and coincides with the geometric specular angle as shown in Figure 17. This means that the geometrical specular angle is equal to the analyzed specular angle for sample A. The BRDF peak value at specular angle becomes larger as the angle of incidence is increased. This effect is also observed in Figure 18 where the flat portion of the log-log plot

increases with increasing incident angle. It is noted that some deviations exist between the back and front scattering directions (section 3.1) at the  $45^\circ$  and  $60^\circ$  incident angles.

As can be seen from Figure 19, sample B also shows that the geometrical specular angle coincides with the incident angles such as in sample A. The specular regions as seen in the log-log plot (Figure 20) of sample B are wider than in sample A. However, the peak BRDF value at the specular angle is less than in sample A.

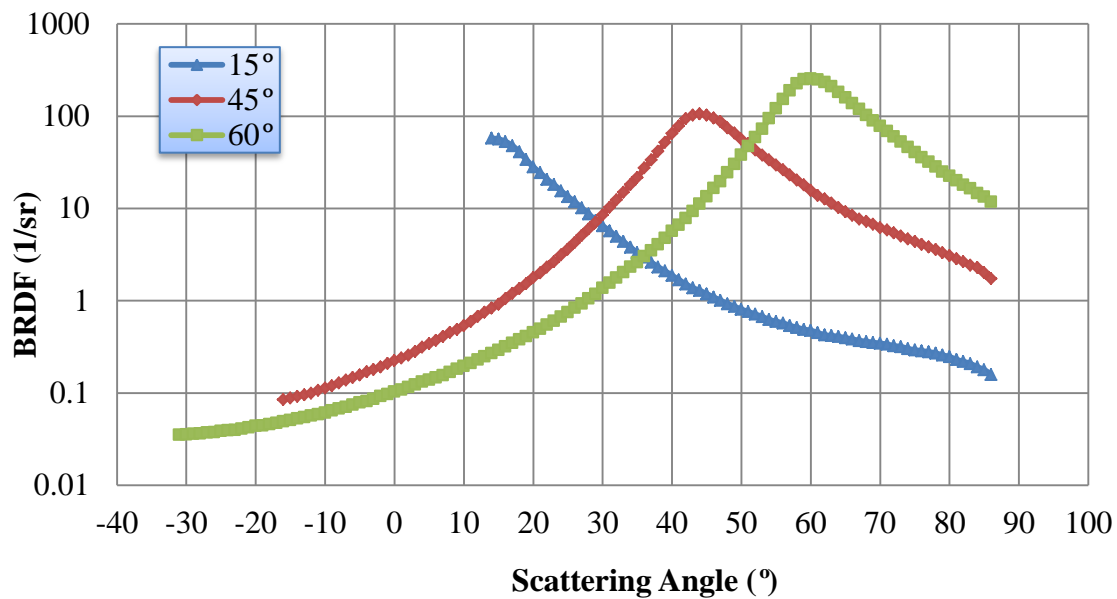


**Figure 17** Comparison of the BRDF with the three different incident angles in Sample A

(1  $\mu\text{m}$ )

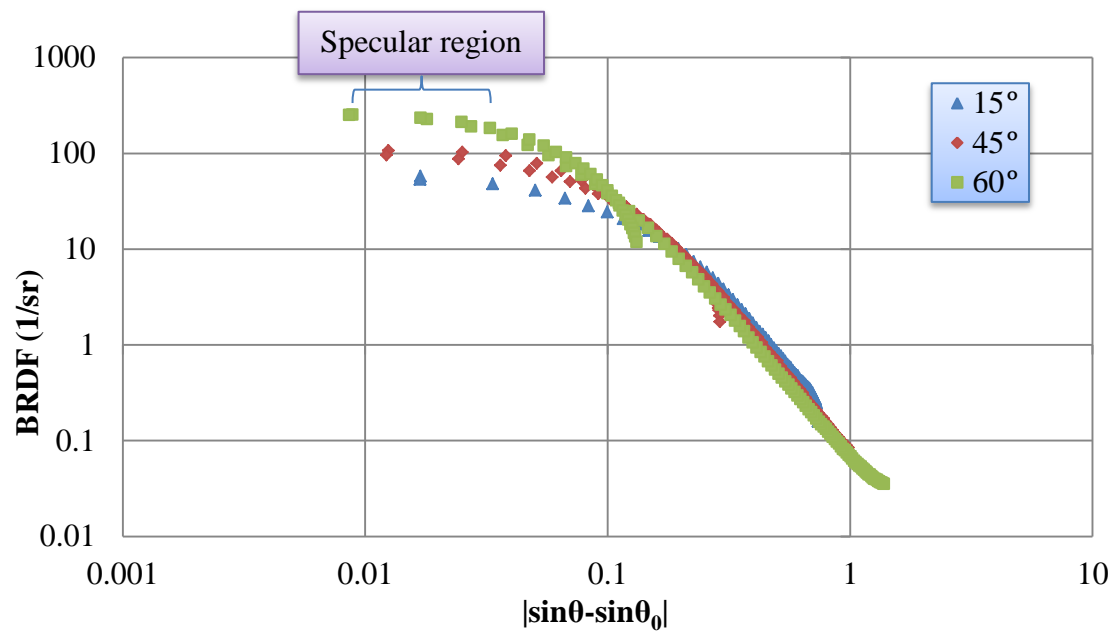


**Figure 18** Comparison of the BRDF with the three different incident angles, expressed by the log-log plot for Sample A (1  $\mu\text{m}$ )

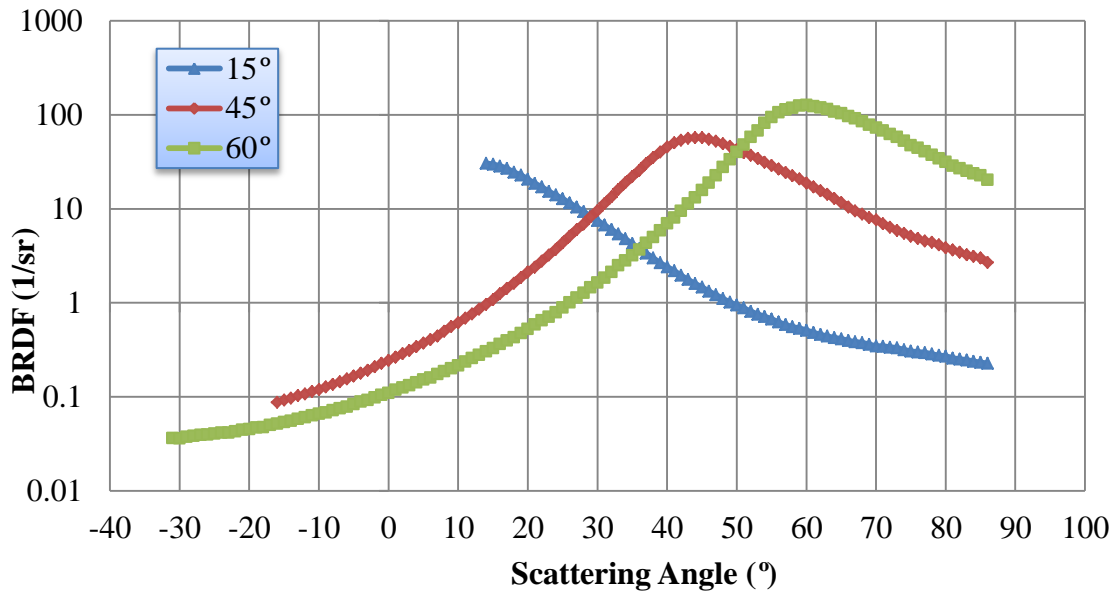


**Figure 19** Comparison of the BRDF with the three different incident angles in Sample B

(3  $\mu\text{m}$ )

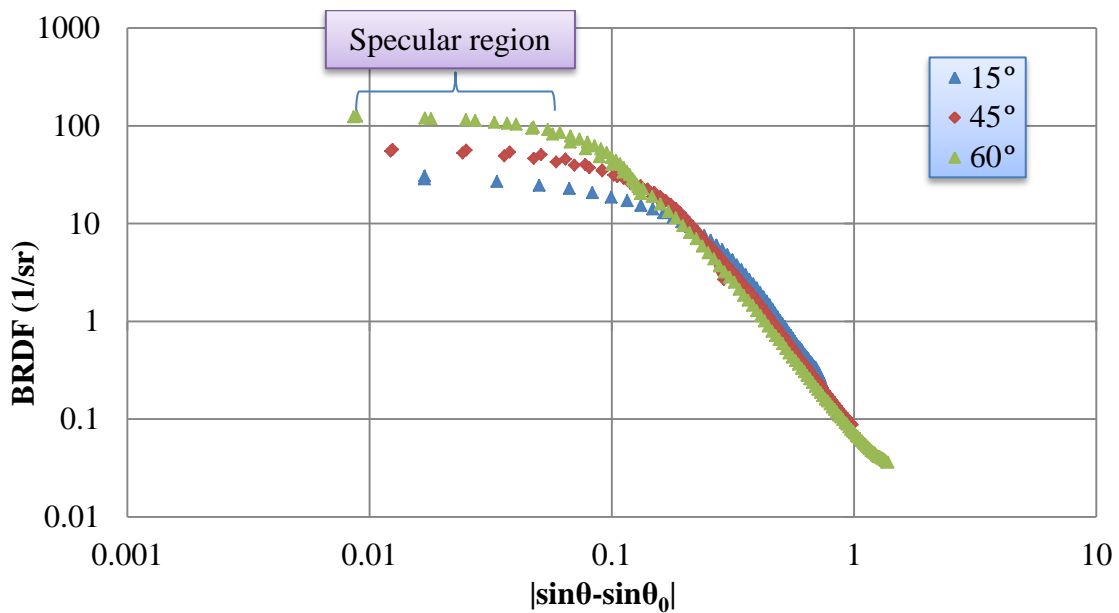


**Figure 20** Comparison of the BRDF with the three different incident angles, expressed by the log-log plot for Sample B (3  $\mu\text{m}$ ).

In the graph of sample C in Figure 21, the geometrical specular angles are well defined at the 15° incident angle. However, the scattering angle at the peak value of BRDF is shifted compared with the geometrical specular angle at the 45° and 60° incident angles. In these cases, the shifted specular angle at the 45° and 60° incident angles are 46° and 64° respectively. This observed shift in the peak could be considered simply an error in angle measurement. However, as will be seen, this shift was the first indication of an effect due to increasing surface roughness. The specular region of sample C is also wider than both samples A and B as shown in Figure 22. When the specular angle,  $\theta_0$ , is changed to the shifted specular angle value, there is no deviation between the back and front scattering direction.

The BRDF graph of sample D is shown in Figure 23. The peak BRDF value is shifted at 52° scattering angle because the geometrical specular angle is moved from 45° to 52°. In the 60° incident angle, the BRDF value is continuously increased almost to the maximum scattering angle. Because of this reason, we did not analyze the peak BRDF value at the specular angle precisely. We considered that the specular angle is shifted from 60° to 70° in this sample at the 60° incident angle. In Figure 24, there is a branch at the 60° incident angle.

As can be seen from the result of sample E, this sample has some different characteristics compared with other samples. At first, the BRDF graph shows a flat portion after around 45° scattering angle, and the BRDF graph shows a slight increase



after around  $60^\circ$  scattering angle as shown in Figure 25. Because of these BRDF values, we considered that the specular angle at the  $45^\circ$  and  $60^\circ$  incident angles are shifted from  $45^\circ$  to  $52^\circ$  and  $60^\circ$  to  $70^\circ$  respectively. So, when the BRDF graph with respect to  $|\vec{\beta} - \vec{\beta}_o|$  is drawn using these results as shown in Figure 26, there are also branches between the back and front scattering direction. We could predict that these observed branches in the BRDF graphs could appear when the BRDF values do not decrease away from the geometrical specular angle.

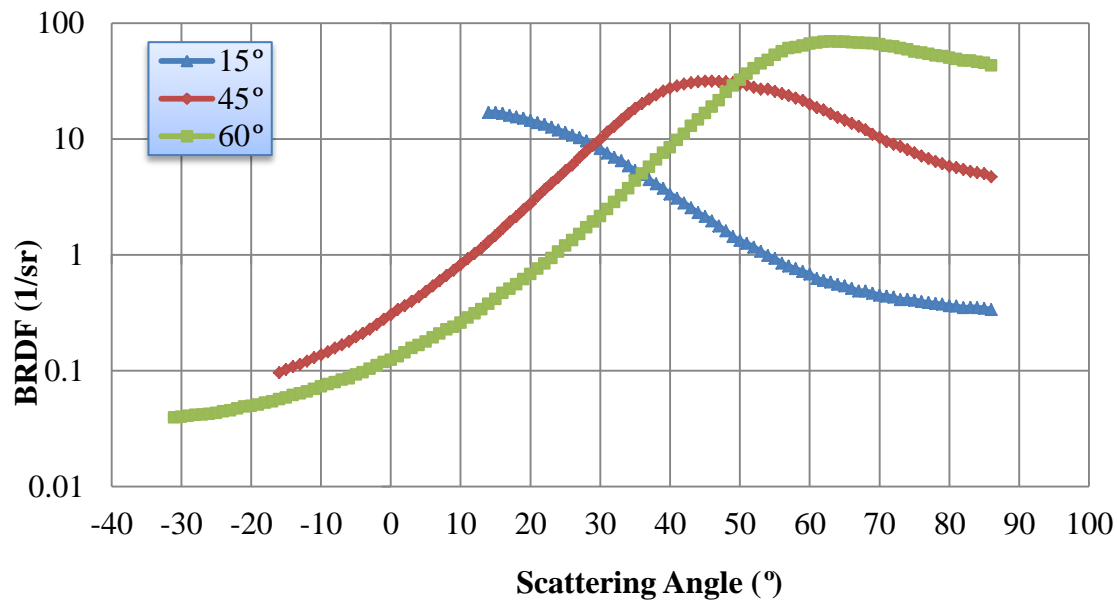


**Figure 21** Comparison of the BRDF with the three different incident angles in Sample C

(6  $\mu\text{m}$ )

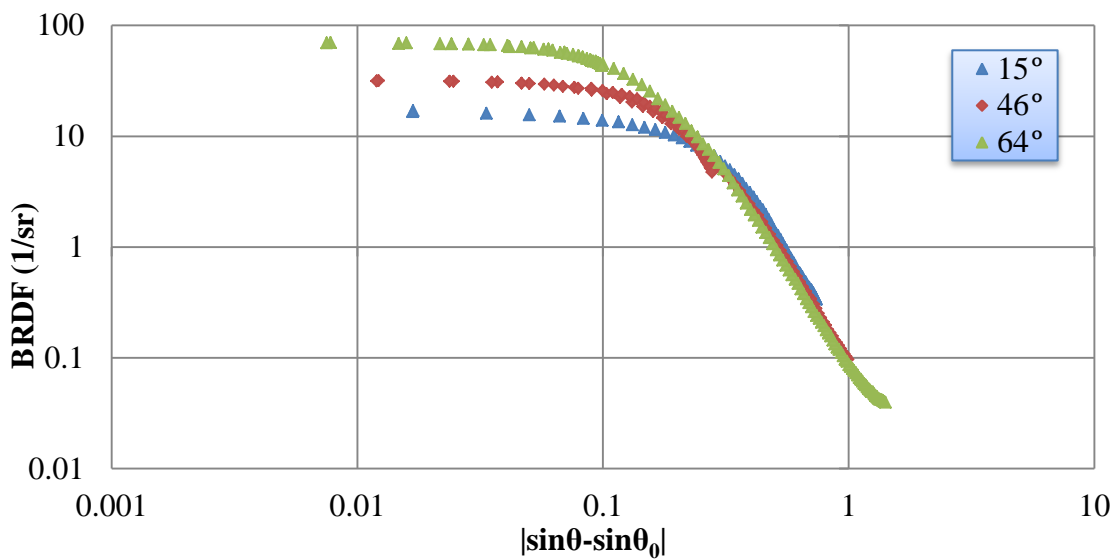


**Figure 22** Comparison of the BRDF with the three different incident angles, expressed by the log-log plot for Sample C (6  $\mu\text{m}$ ).  $\theta_0$  for 45° incident angle was modified to 46° and  $\theta_0$  for 60° incident angle was modified to 64°

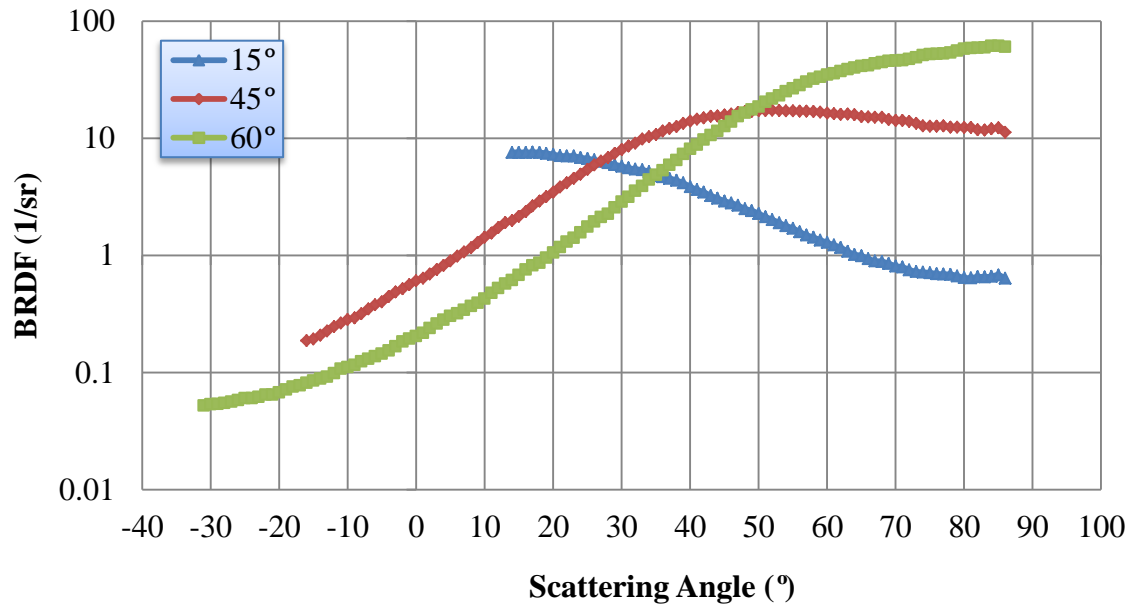


**Figure 23** Comparison of the BRDF with the three different incident angles in Sample D

(12  $\mu\text{m}$ )

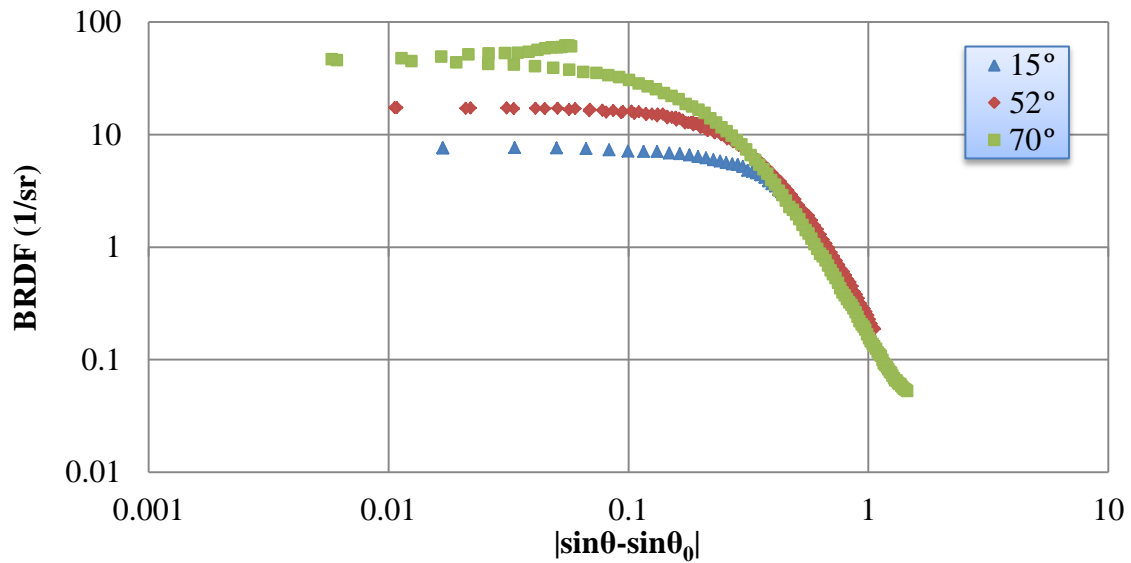


**Figure 24** Comparison of the BRDF with the three different incident angles, expressed by the log-log plot for Sample D (12  $\mu\text{m}$ ).  $\theta_0$  for 45° incident angle was modified to 52° and  $\theta_0$  for 60° incident angle was modified to 70°

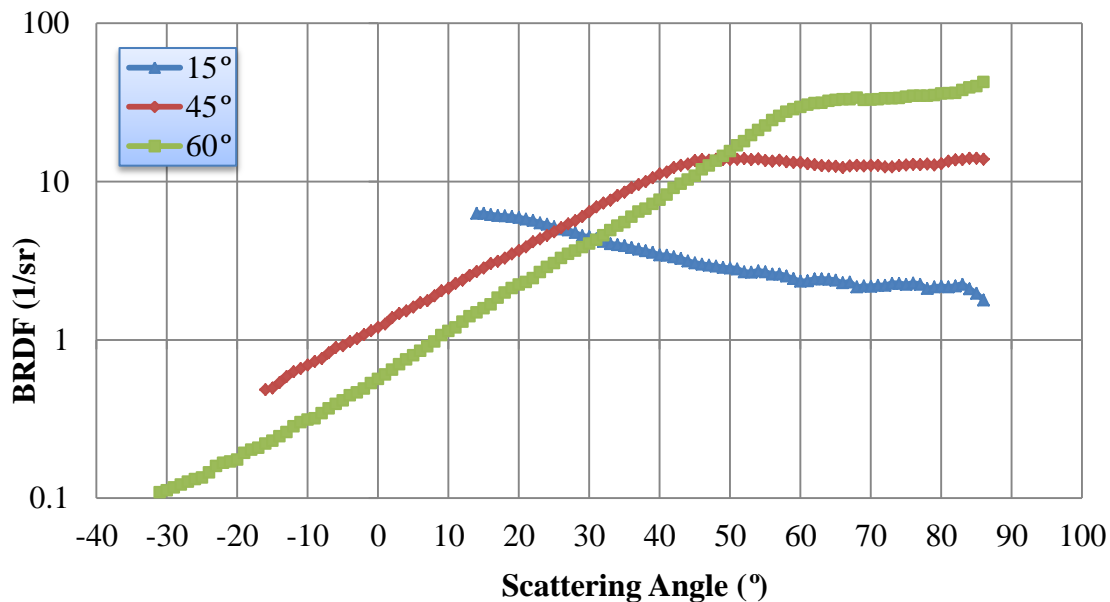


**Figure 25** Comparison of the BRDF with the three different incident angles in Sample E

(19  $\mu\text{m}$ )

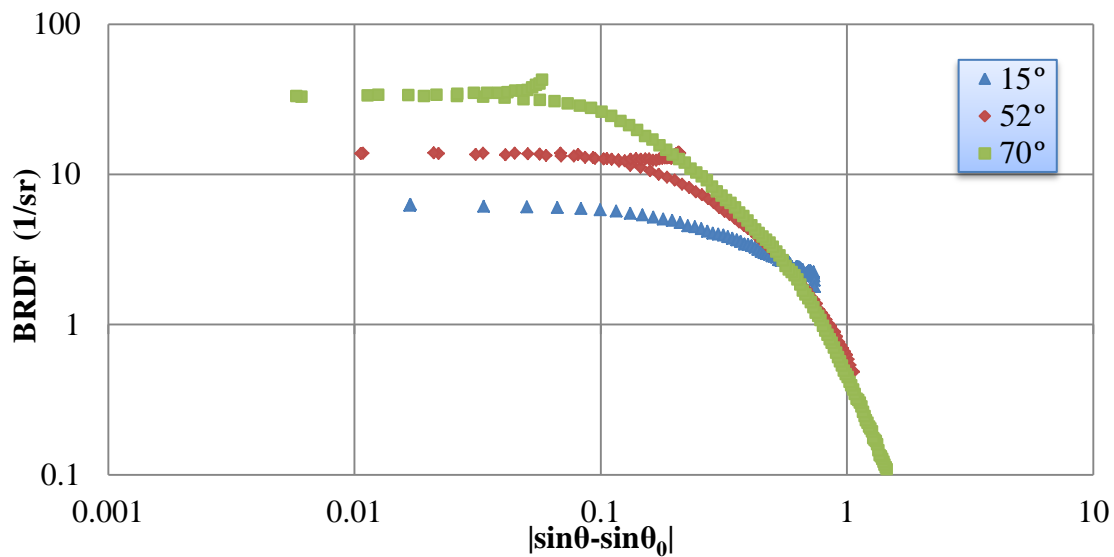


**Figure 26** Comparison of the BRDF with the three different incident angles, expressed by the log-log plot for Sample E (19  $\mu\text{m}$ ).  $\theta_0$  for 45° incident angle was modified to 52° and  $\theta_0$  for 60° incident angle was modified to 70°

These results show, as predicted, that the BRDF is affected by the incident angle orientation. In addition, the BRDF increased when the incident angle also increased regardless of the surface roughness of the sample. Also, the peak scattering angle is shifted to a higher angle away from the specular angle when the surface roughness is increased and the incident angle is higher, and some branches appear for large micro-scale rough samples such as samples D and E.

#### 4.3 Scattering effects with respect to the surface roughness

In this section, the scattered light profiles of the five different samples having a wide range of roughness values are described. Each graph compares the BRDF of five samples keeping the incident angle a constant.

As can be seen from Figure 27, the BRDF decreased when the scattering angle increased regardless of the surface roughness. The BRDF graph shows a more gentle declining slope when the surface roughness is increased.

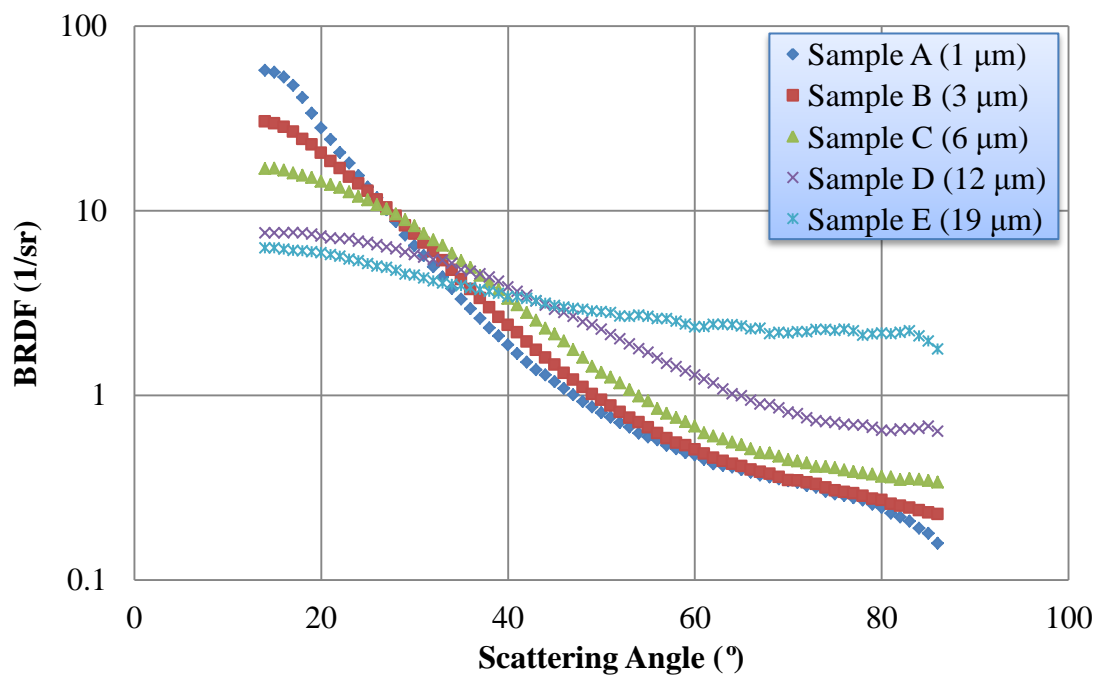
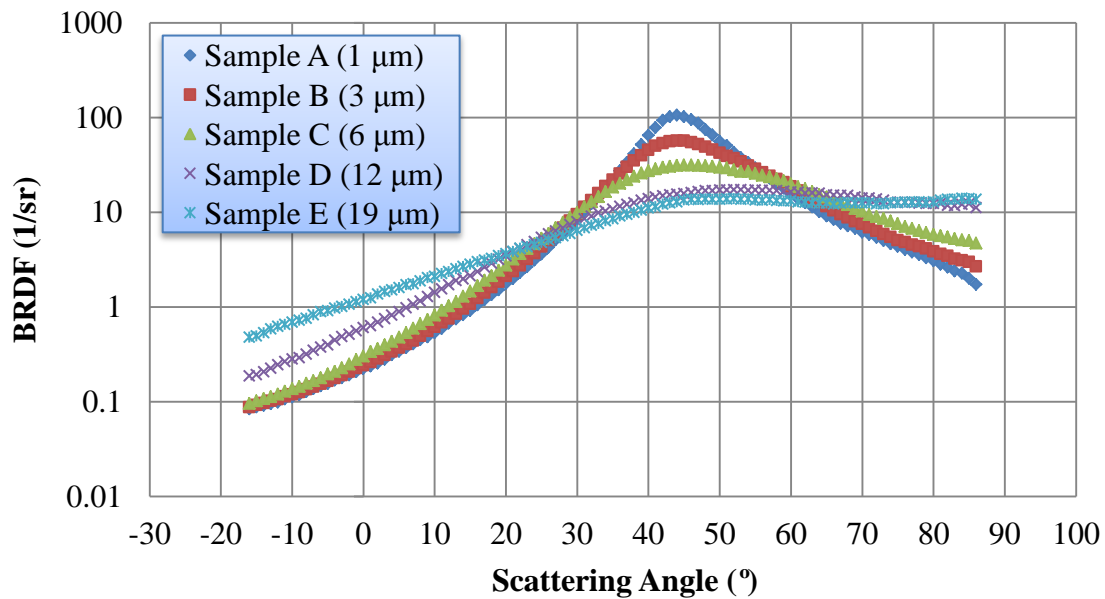


**Figure 27** Comparison of the BRDF for samples with a wide range of surface roughness for a 15° incident angle

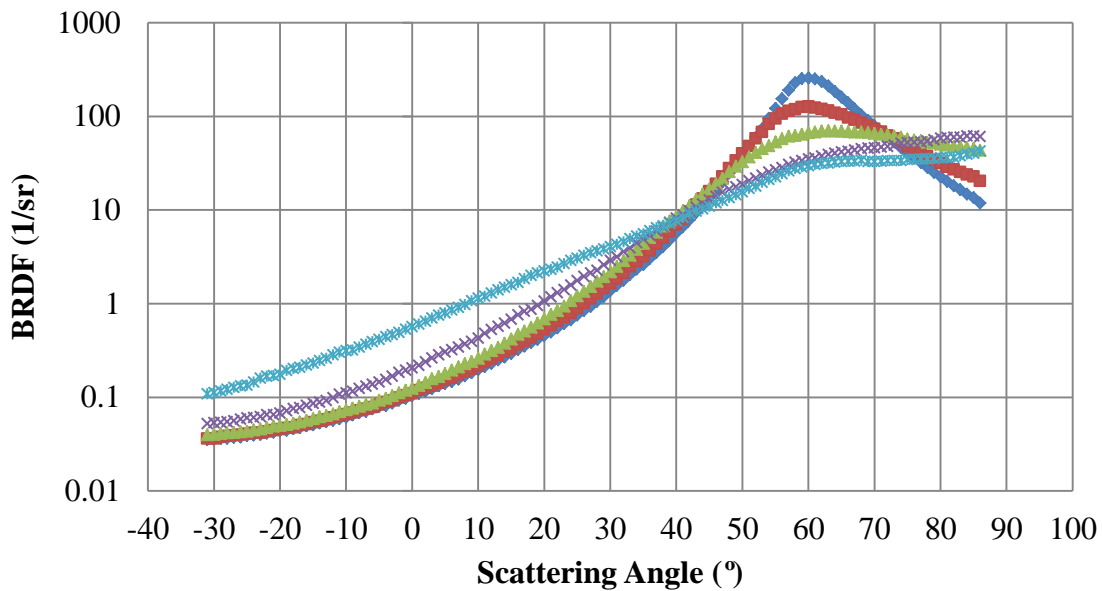
Figure 28 shows the BRDF graphs with respect to the roughness of the sample surface when the incident angles are  $45^\circ$  and  $60^\circ$  respectively. The BRDF values of samples A, B, and C obviously decreased based on the BRDF peak value as shown in Figure 28 (a). However, the BRDF of sample D changed slightly after the geometrical specular angle. The BRDF graph of sample E shows the flat portion away from the  $60^\circ$  scattering angle.

When the incident angle is  $60^\circ$ , the BRDF values of samples A and B are obviously decreased in both the back and front scattering direction based on the  $60^\circ$  as shown in Figure 28 (b). The BRDF values of sample C shows a small decrease after  $60^\circ$ . On the other hand, the BRDF of samples D and E continuously increased when the scattering angle increased regardless of the geometrical specular angle.

These results show, as predicted, that the BRDF is affected by the surface roughness of samples. The peak value of the BRDF is larger at the geometrical specular angle when the roughness becomes smaller. In contrast, the BRDF values are relatively large according to the increasing surface roughness when the scattering angles are away from the geometrical specular angle to around  $\pm 15^\circ$  regardless of the incident angle.



(a)



(b)

**Figure 28** Comparison of the BRDF for samples with a wide range of surface roughness for (a) 45° and (b) 60° incident angles



As previously mentioned in discussing the analyzed specular angle in section 4.2, the geometrical specular angle of some samples is shifted according to the surface roughness and the incident angle. When the incident angle is  $15^\circ$ , the BRDF value decreased with respect to the surface roughness at the specular region. However, the BRDF has a gentle declining slope away from the specular region when the surface roughness is increased as shown in Figure 29.

As can be seen from Figure 30, the peak value of BRDF at the specular angle is also bigger when the roughness becomes smaller at the  $45^\circ$  incident angle. In samples D and E, the BRDF graph after the specular region is separated by the back and front scattering direction at the  $60^\circ$  incident angle as shown in Figure 31. On the other hand, the specular region at large surface roughness is wider than the small surface roughness.

Through Figure 30 and Figure 31, we could predict that the specular reflection occurs usually at small roughness. On the other hand, the diffuse reflection appears more often at large roughness. Through the data of samples D and E, we can infer that the BRDF equation is not a good measurement for these large micro-scale roughness surfaces and for higher incident angles.

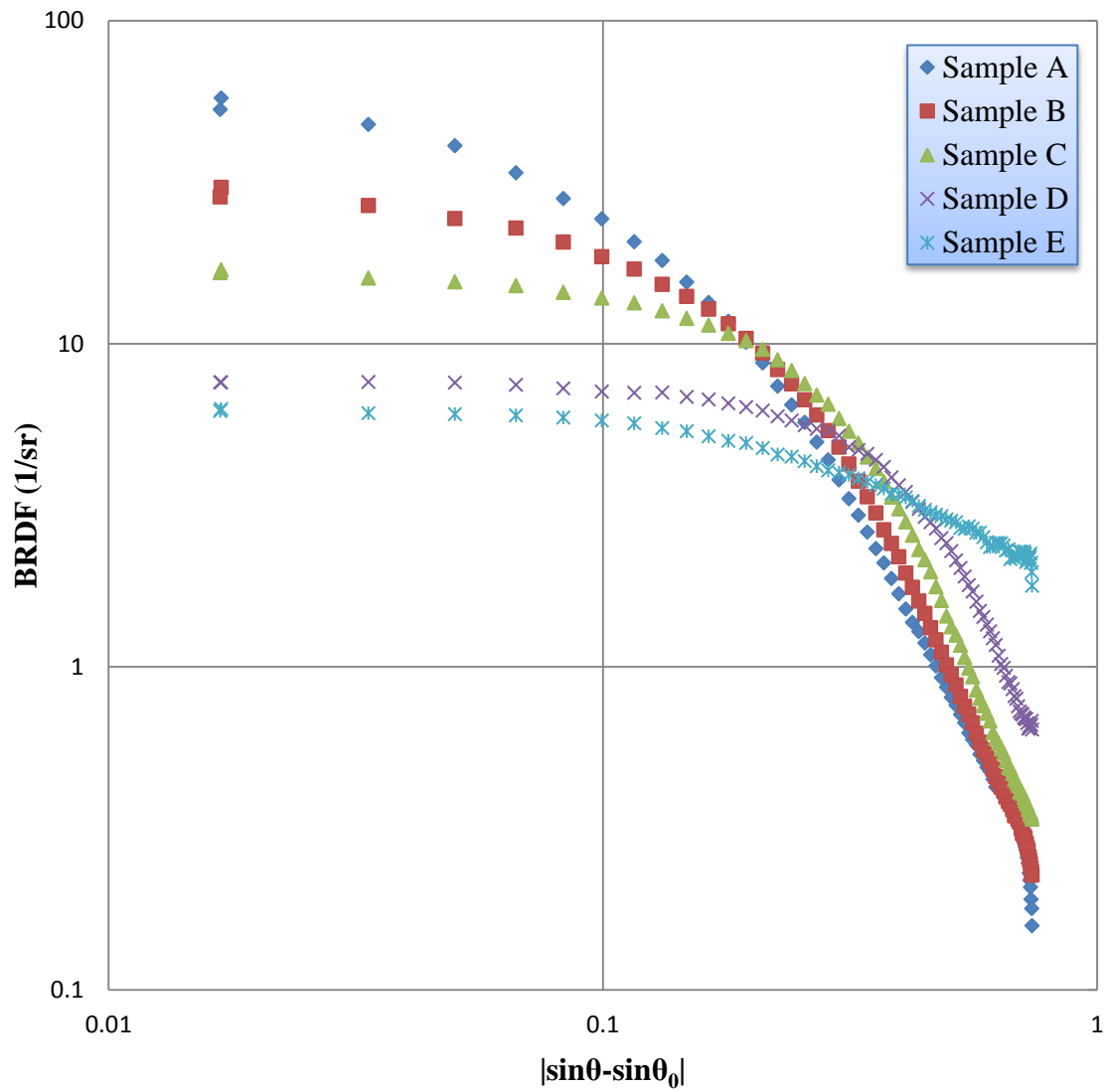


**Figure 29** Comparison of the BRDF for samples with a wide range of surface roughness, expressed by the log-log plot for 15° incident angle

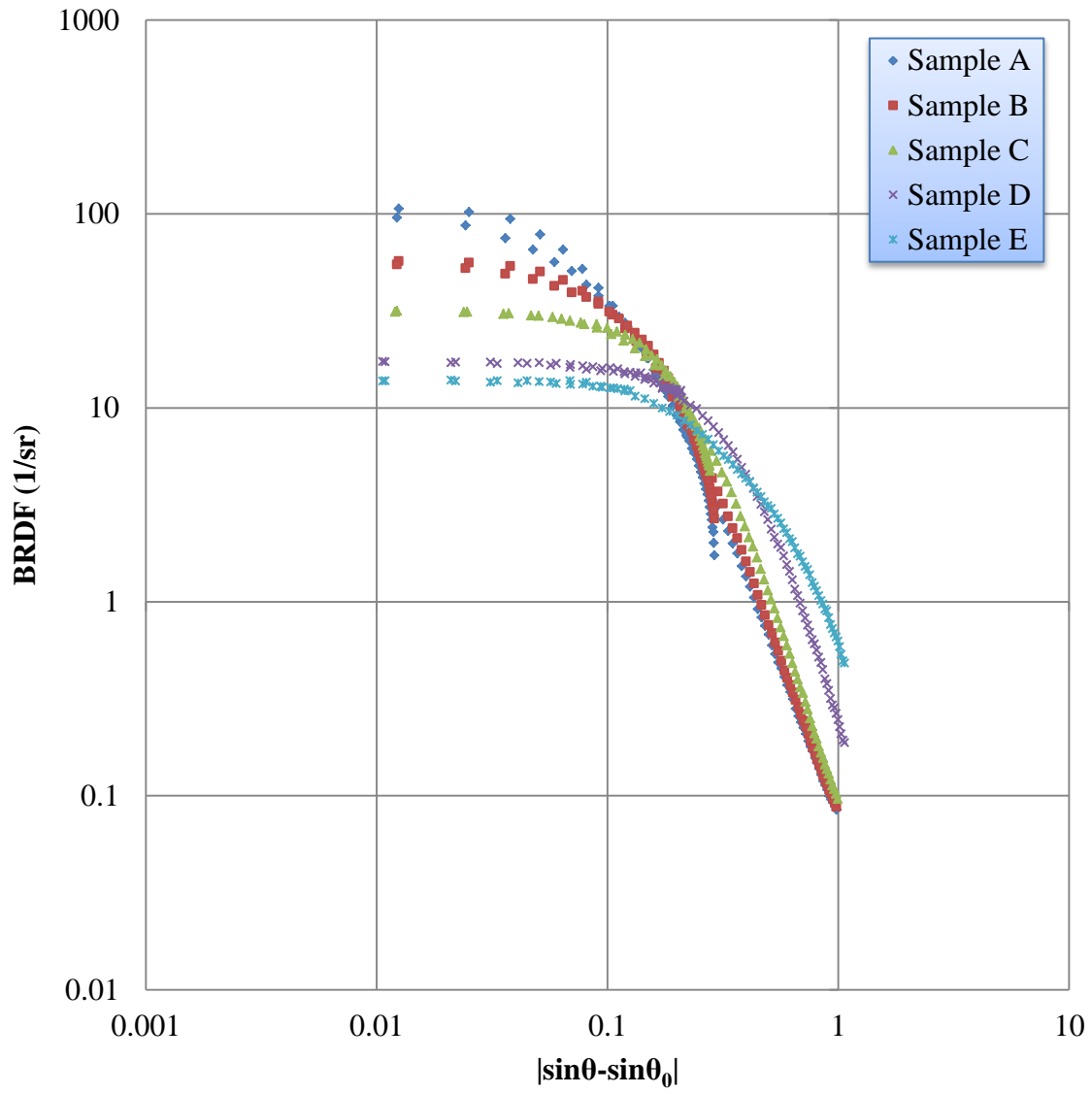


**Figure 30** Comparison of the BRDF for samples with a wide range of surface roughness, expressed by the log-log plot for 45° incident angle

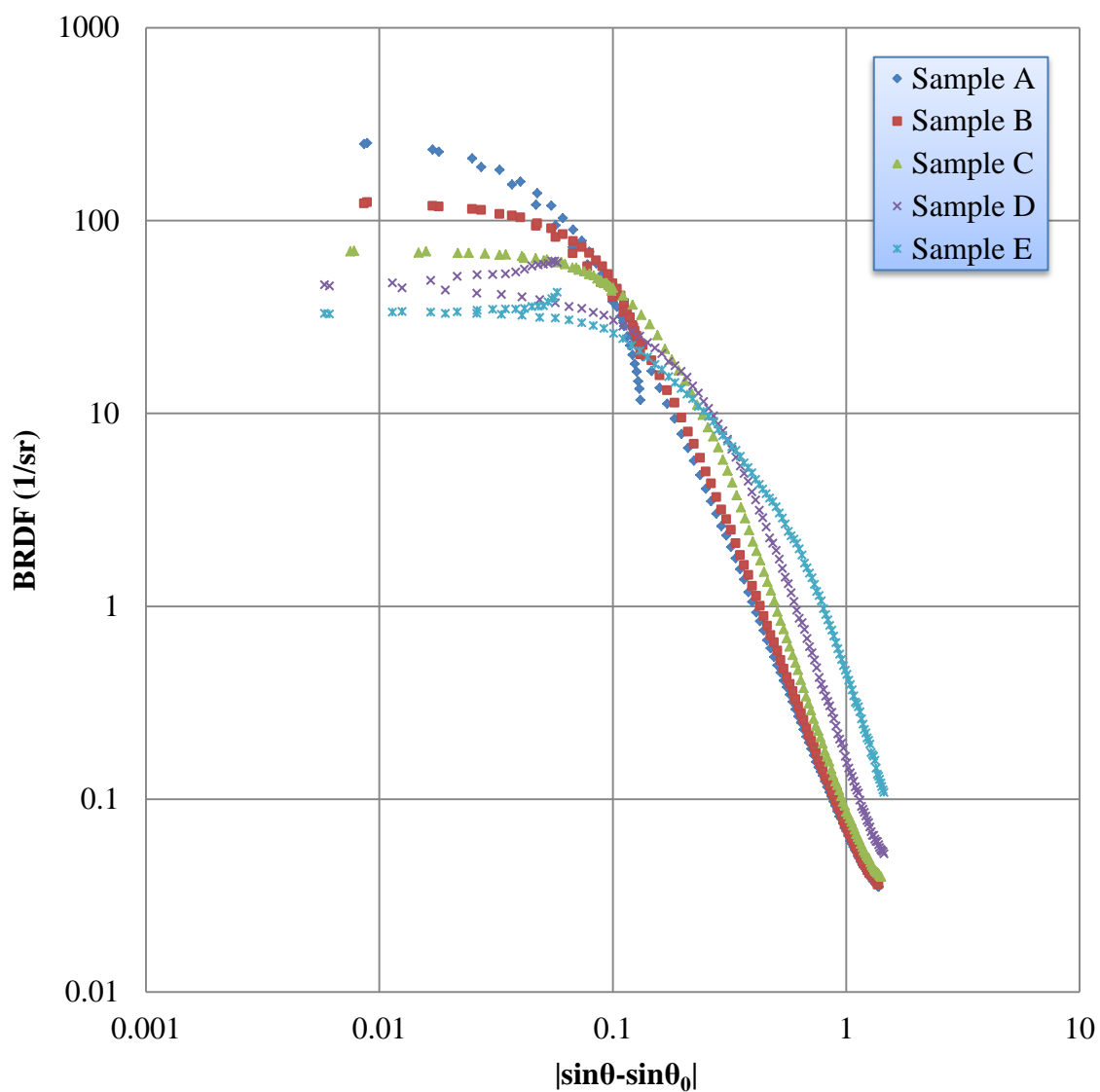


**Figure 31** Comparison of the BRDF for samples with a wide range of surface roughness, expressed by the log-log plot for 60° incident angle

Through Table 3 and Figure 32, we can know the peak value of BRDF for all samples and the relationship between surface roughness and peak scattering angle. As already mentioned, the peak scattering angle is shifted to a higher angle away from the geometrical specular angle with respect to the larger surface roughness and higher incident angle.

**Table 3** The peak value of BRDF with respect to all experimental variations

<b>Sample</b>	<b>Incident angle (°)</b>	<b>Peak scattering angle (°)</b>	<b>Peak BRDF value (<math>sr^{-1}</math>)</b>
<b>A</b>	15	15	56.3
	45	45	102.6
	60	60	255.9
<b>B</b>	15	15	29.7
	45	45	57.1
	60	60	126.9
<b>C</b>	15	15	16.9
	45	46	31.5
	60	64	69.1
<b>D</b>	15	15	7.59
	45	52	15.8
	60	70	46.1
<b>E</b>	15	15	6.29
	45	52	13.9
	60	70	32.8

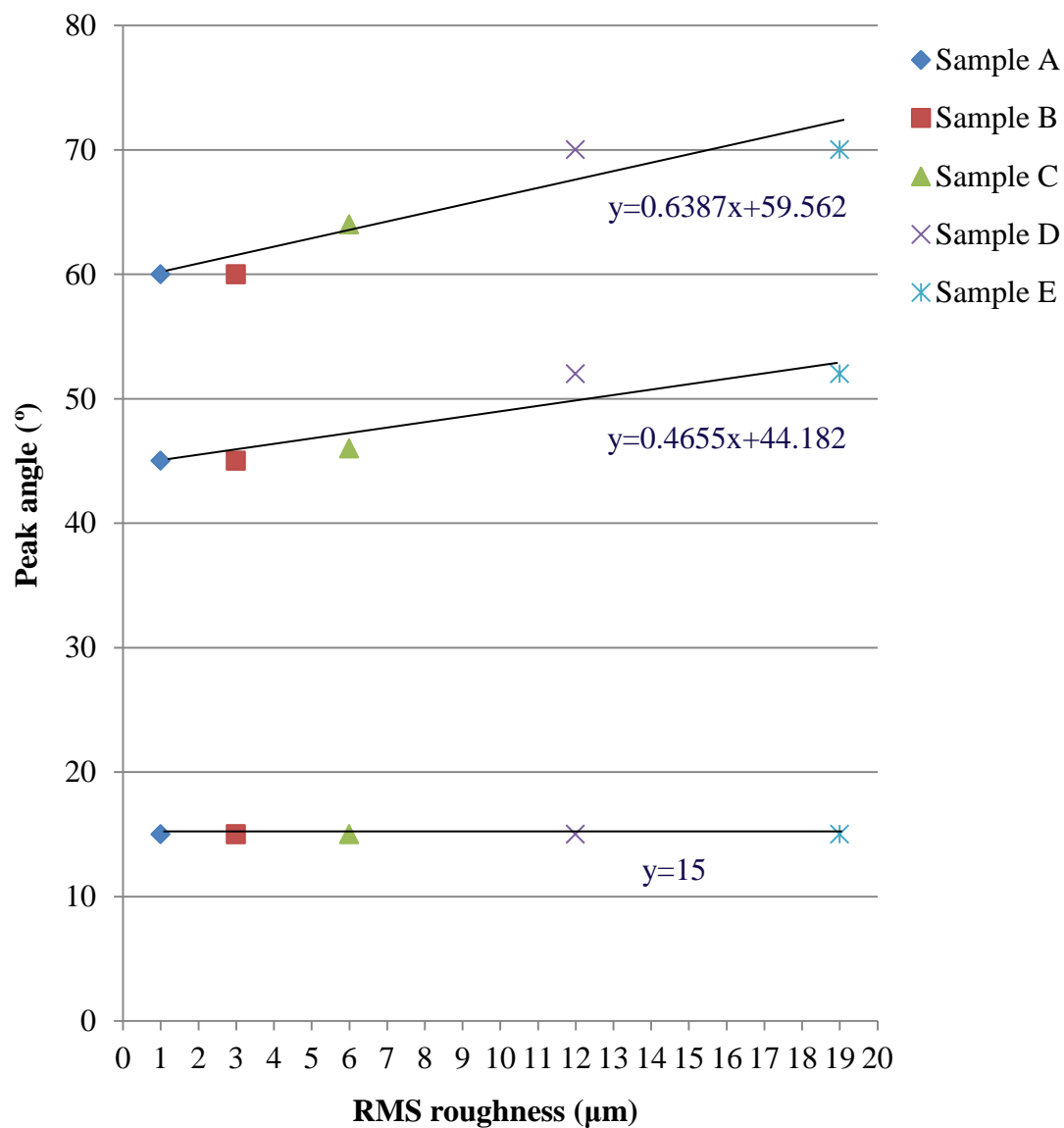


**Figure 32** Relationship between surface roughness and peak scattering angle. Samples D and E have the same peak angle.

#### 4.4 Comparison of the BRDF with the ABg model to obtain the Harvey-Shack model

The ABg scattering model is similar to the Harvey-Shack model in that it is empirically derived from measurement, and is widely used to model scatter that is created by random isotropic surface roughness. In this thesis, parameters  $b_0$ ,  $S$ , and  $L$  of the Harvey-Shack scattering model can be derived from the ABg model parameters.

To derive the ABg model, a “MS Excel Add In” was used. Because the BRDF functions are not linear in the scattering angle, a curve fitting can be performed. This method can minimize the deviation between the ABg model and the measured BRDF plot. The deviation is calculated by using a formula suggested by the Excel program.

$$dev = \sum_{i=1}^{N \text{ value}} (k - BRDF_i)^2 \quad (12)$$

where the constant  $k$  is derived by  $A$ ,  $B$ , and  $g$  values using Equation 9, and the constant  $k$  is varied as long as deviation ( $dev$ ) has reached a minimum value.

In sample C at the  $60^\circ$  incident angle, there is a small deviation between the ABg model (red) and the BRDF data as shown in Figure 33. The fit parameters ( $A$ ,  $B$  and  $g$  values) of samples are shown in a box legend within each figure. On the other hand, samples D and E have large deviation from the ABg model because of the branch as shown in Figure 34 and Figure 35. As we already know about the mean of  $g$  value

(Section 2.4), the slope depends on  $g$  value. This value in the ABg model is typically between 0 and 3 [14]. However,  $g$  values at some large surface roughness and some incident angles are bigger than 3 as shown in Figure 33.

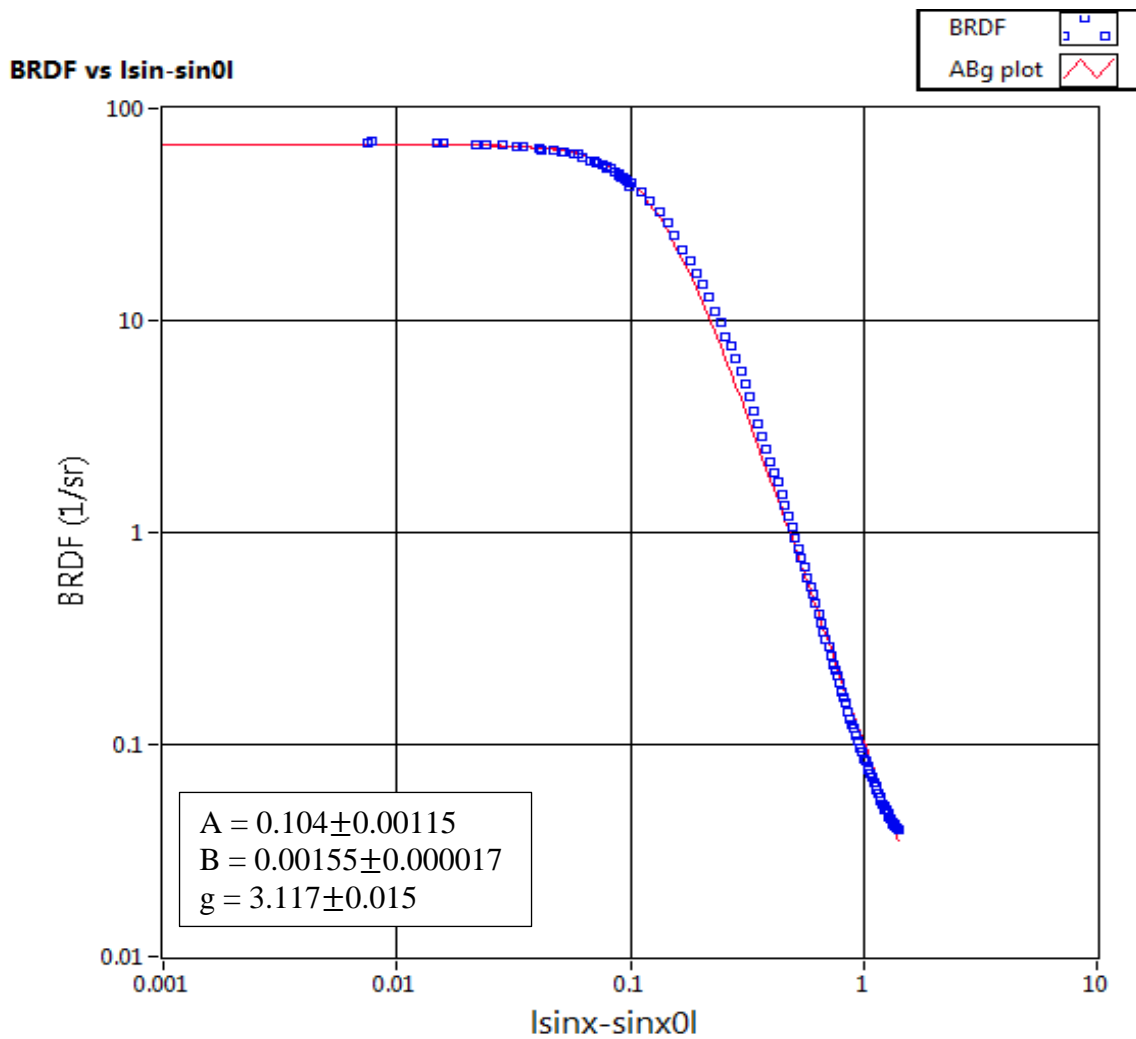


**Figure 33** Comparison between the BRDF and the ABg model of Sample C at the  $60^\circ$  incident angle



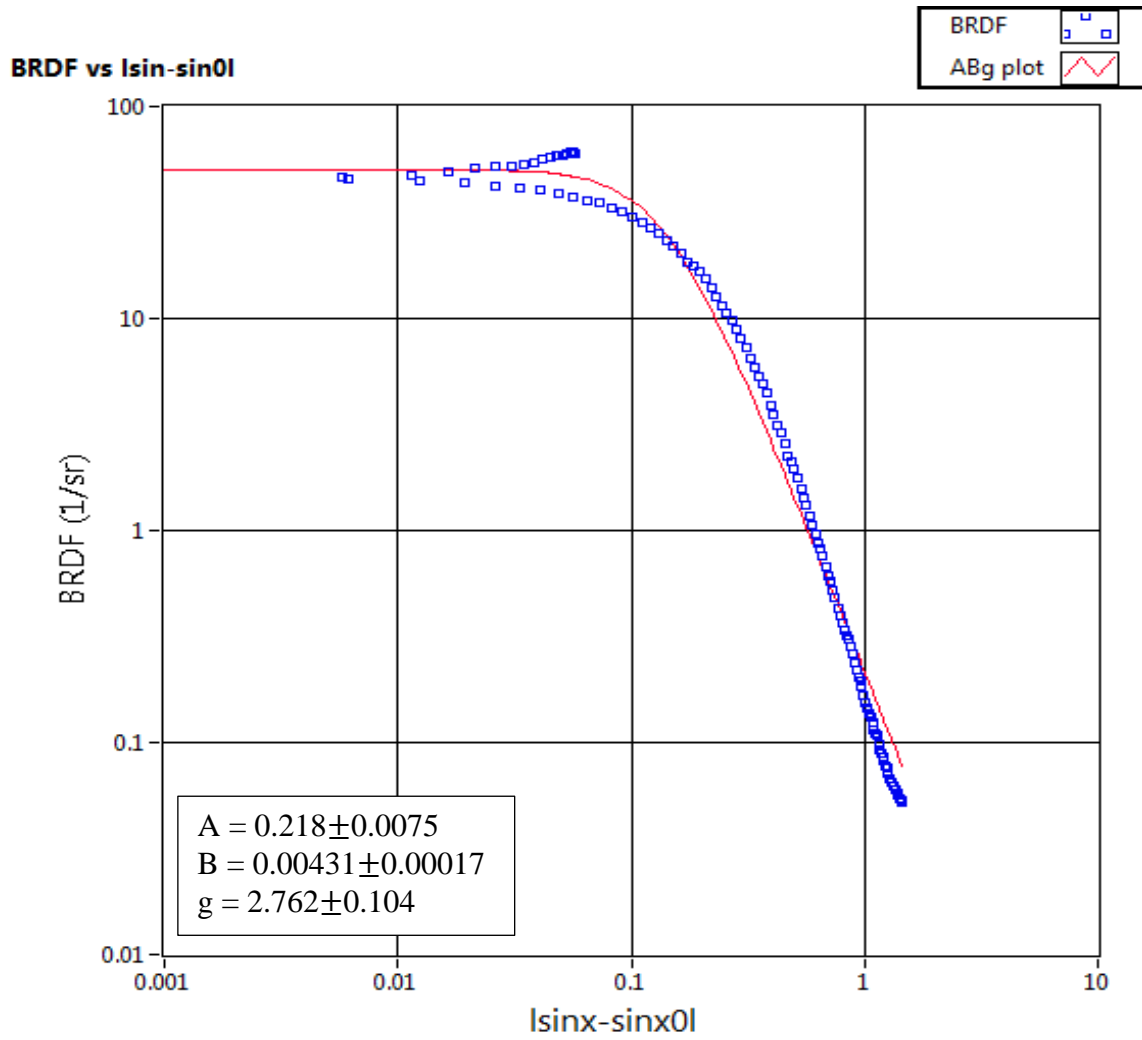


**Figure 34** Comparison between the BRDF and ABg model of Sample D at the 60° incident angle

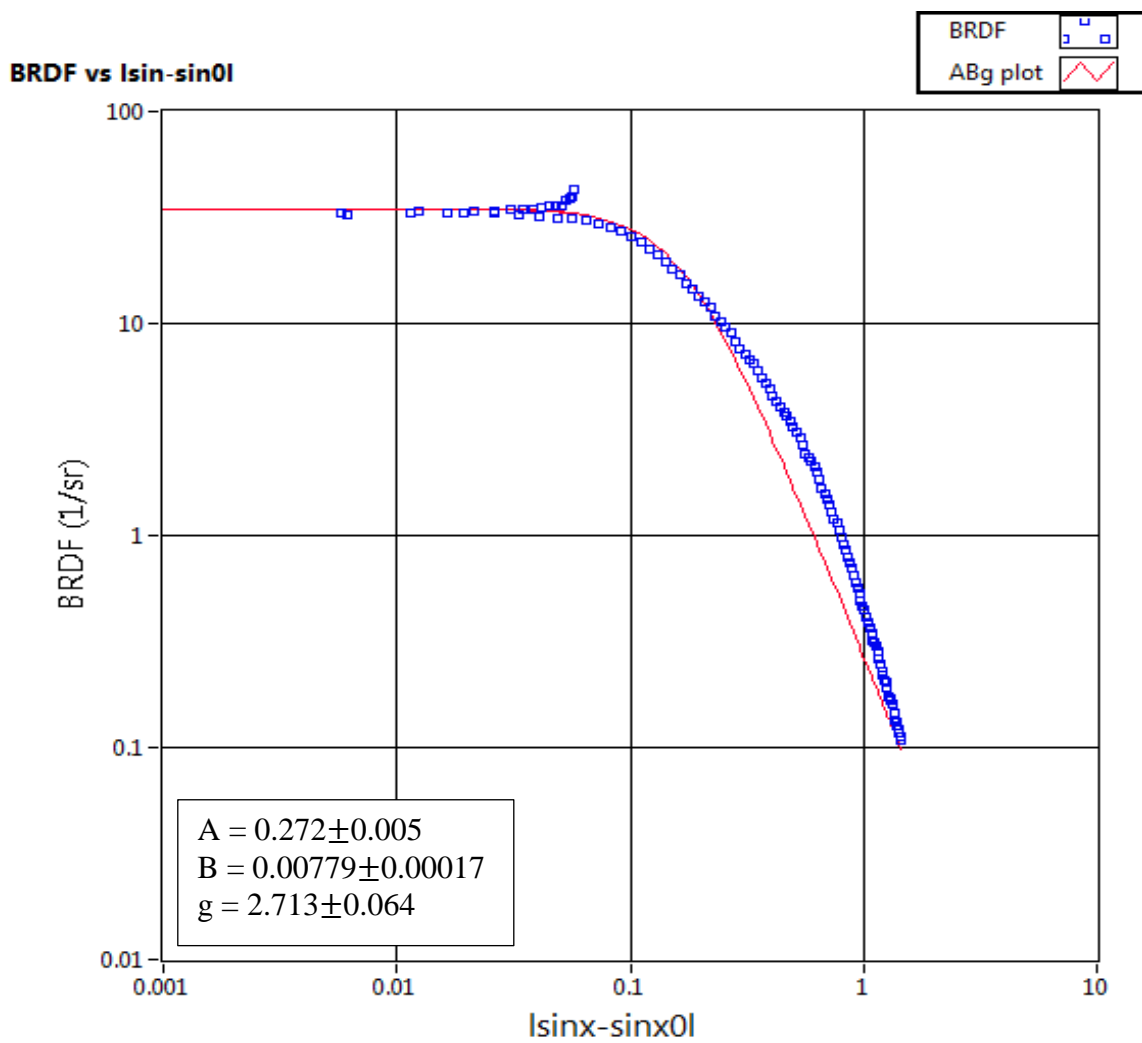


**Figure 35** Comparison between the BRDF and ABg model of Sample E at the 60° incident angle

Figure 36 (a) shows the ABg model of sample A. Figure 36 (b) and (c) show the ABg model of samples D and E with respect to the incident angle. Through the experimental results, we can predict that  $g$  values at small surface roughness are similar regardless of the incident angle. However, the large surface roughness shows the difference between the slopes.

Also, as can be seen from Appendix C, the ABg fitted model can explain the measured BRDF plot well in samples A, B, and C. So, we can predict that the parameters from these samples can be used in optical design software. However, in samples D and E, it cannot explain the branch in back scattering angle region of the measured BRDF. Because of this reason, we can predict that the ABg model may not be appropriate to use for large surface roughness and for higher incident angle.

Using the derived  $A$ ,  $B$ , and  $g$  values, the Harvey-Shack model explained in section 2.4 is defined. There is a deviation between the ABg and the Harvey-Shack model as shown in Figure 37. This deviation usually appears in the “knee” part of the graph regardless of the surface roughness and the incident angle. The Harvey-Shack models of all samples are compared with the ABg model in Appendix D.

Using the ABg and the Harvey-Shack models, we can predict that the scattering characteristics are a function of the surface roughness and the incident angle such as the BRDF graph. However, these models are also not appropriate to use for larger surface

roughness and for higher incident angles such as in samples D and E because these methods cannot explain the branch in back scattering direction. In some samples, the  $g$  value is different compared with its values described by using the smooth surface ( $\sigma_{rms} \ll \lambda$ ). These results show, as predicted, that  $g$  value could be bigger than 3 at some larger surface roughness.

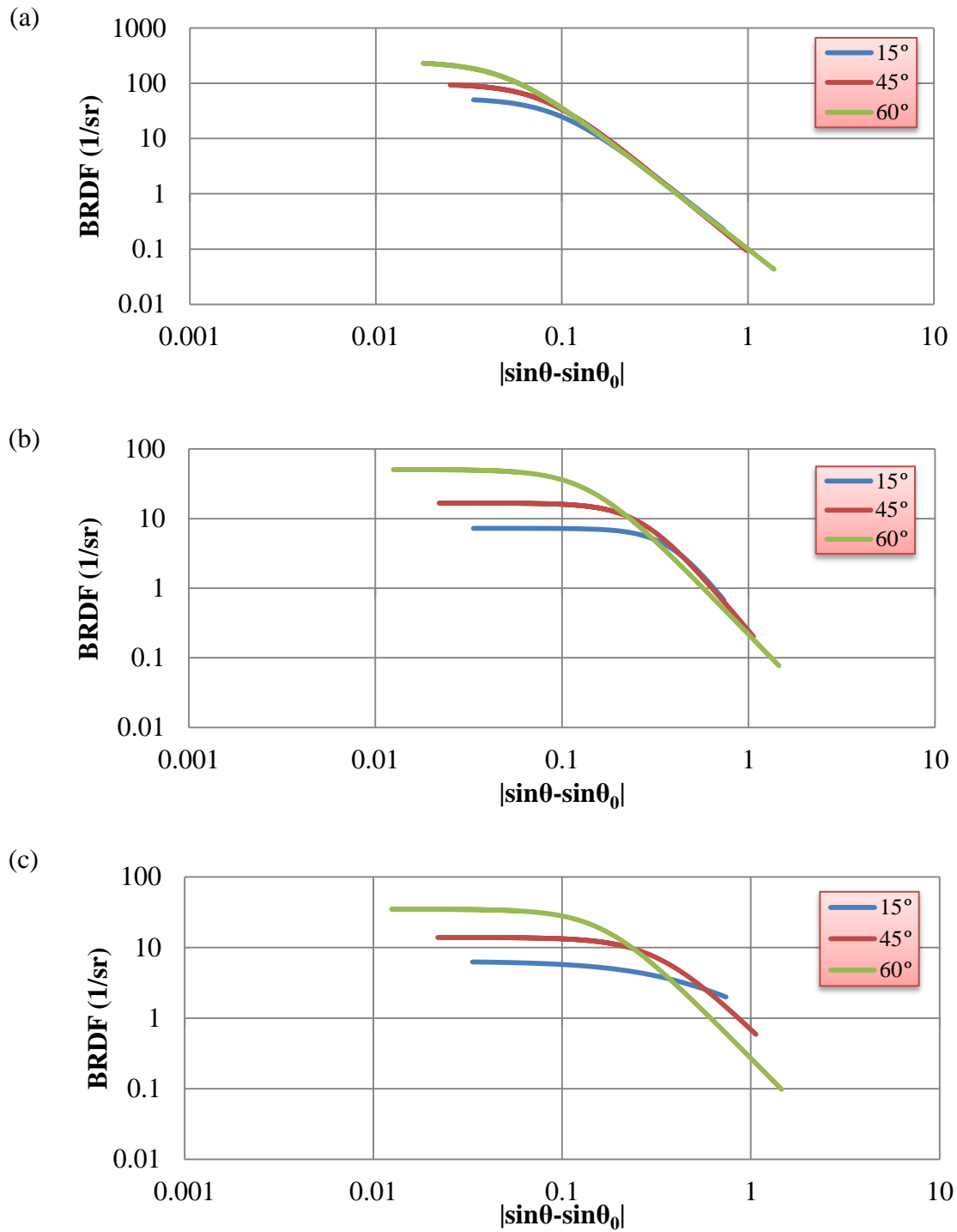


**Figure 36** Comparison of the ABg model in (a) Sample A, (b) Sample D, (c) Sample E

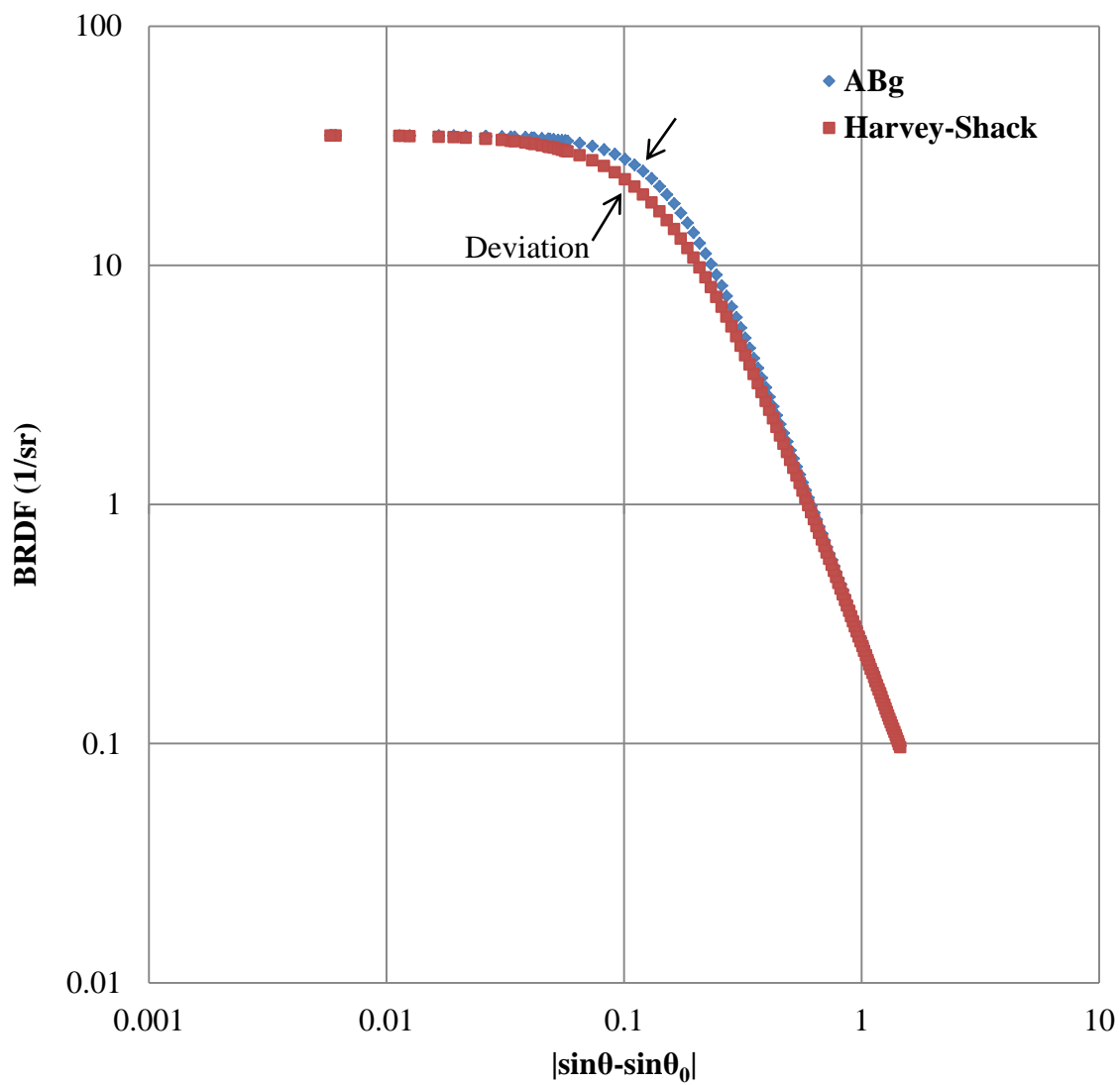


**Figure 37** Comparison of the Harvey-Shack with the ABg model of Sample E at the 60° incident angle

#### 4.5 Error analysis

The BRDF measurement variation can be examined through a simple error analysis [25]. The error equation has been found by standard error analysis, under the assumption that the four defining variables are independent of one another [26]. The total error is

$$\frac{\Delta BRDF}{BRDF} = \left[ \left[ \frac{\Delta P_s}{P_s} \right]^2 + \left[ \frac{\Delta P_i}{P_i} \right]^2 + \left[ \frac{\Delta \Omega}{\Omega} \right]^2 + \left[ \frac{\Delta \theta_s \sin(\theta_s)}{\cos(\theta_s)} \right]^2 \right]^{1/2} \quad (13)$$

The four terms in this equation represent error in the measurement of scattered power, incident power, receiver solid angle, and scattering angle respectively. In this thesis, the BRDF power is changed to the BRDF voltage already explained in section 2.3.

The third term of the error equation is related to the solid angle. In this term, uncertainties in the solid angle are caused by measurement errors of the receiver aperture radius  $r$  and the aperture to sample distance  $R$ . The third term is modified as

$$\frac{\Delta \Omega}{\Omega} = \left[ \left( \frac{2\Delta r}{r} \right)^2 + \left( \frac{2\Delta R}{R} \right)^2 \right]^{1/2} \quad (14)$$

Through the above explanations, Equation 13 is modified

$$\frac{\Delta BRDF}{BRDF} = \left[ \left[ \frac{\Delta V_s}{V_s} \right]^2 + \left[ \frac{\Delta V_i}{V_i} \right]^2 + \left[ \left( \frac{2\Delta r}{r} \right)^2 + \left( \frac{2\Delta R}{R} \right)^2 \right] + \left[ \frac{\Delta \theta_s \sin(\theta_s)}{\cos(\theta_s)} \right]^2 \right]^{1/2} \quad (15)$$

where  $\Delta \theta_s$  is the tolerance of scattering angle and is in radians. In this research, the tolerance of scattering angle is  $0.5^\circ$  which is modified by the radian, 0.00873. The aperture radius is 1.025 mm and the tolerance,  $\Delta r$ , is 0.01 mm. The distance between the aperture and sample is 54.96 mm and the tolerance,  $\Delta R$ , is 0.05 mm.  $\Delta BRDF/BRDF$

has no units. The total error is affected by the scattering angle because  $\Delta BRDF/BRDF$  value depends on the variable values such as the scattered voltage and scattering angle.

The average error of the BRDF is calculated using the sum of total error according to each scattering angle. When the BRDF error is estimated, we can observe that  $\Delta BRDF/BRDF$  becomes bigger when the scattering angle is away from the specular angle. Also, the solid angle error is the largest source of overall error. Table 4 shows the total BRDF error of all samples and all incident angles. As can be seen from Table 4, the average error of the BRDF is around 3% regardless of the surface roughness and the incident angle.

**Table 4** The average error of BRDF data for all samples and incident angles

Incident angle Sample	15°	45°	60°
Sample A	0.03423	0.03262	0.03187
Sample B	0.03410	0.03134	0.03023
Sample C	0.03299	0.03058	0.02957
Sample D	0.03418	0.03122	0.02986
Sample E	0.03421	0.03108	0.03048



## 5. CONCLUSIONS

This study has been a general investigation of surface scatter phenomena with respect to the five different samples. These samples covered a range of surface roughness, with the most rough being micro-scale roughness. In addition, samples contained isotropic textures.

This thesis used the BRDF measurement because it is commonly used to quantify scattered light patterns from surfaces. By using the measured BRDF data of the experimental samples, the ABg and the Harvey-Shack scattering models are used to define the surface characteristics of samples. Experimental verification of these models has been mostly demonstrated for smooth surfaces ( $\sigma_{rms} \ll \lambda$ ). However, we used these scatter measurement methods to verify whether these are appropriate for defining the surface scattering characteristics of micro-scale rough surfaces ( $\sigma_{rms} \gg \lambda$ ) and to get the parameters for use in optical design software.

Through the experimental results, we can predict that the BRDF values are affected by the incident angle and surface roughness. Experimental verification of the thesis samples was defined such that the peak value of BRDF is increased when the incident angle is also increased regardless of the surface roughness and that the peak BRDF value of small surface roughness is larger than its values of large surface

roughness at the same incident angle. These characteristics are similar to the smooth surface cases.

As surface roughness increases, the scattering angle of peak BRDF value shifts to larger scattering angles away from the geometrical specular angle when the surface roughness is larger than sample C. However, when the surface roughness is larger than sample D or E, we could not define the specular angle precisely because the BRDF values are increased continuously or values are not decreased away from the geometrical specular angle to large scattering angle. These characteristics result in a branch between the back and front scattering direction.

Using the measured BRDF data, the parameters in the ABg model can be derived. The model curve fits well for small surface roughness among all five experimental samples regardless of the incident angle. On the other hand, there exists a large deviation between the ABg model and the measured BRDF data at large surface roughness such as in samples D and E. Also, the parameters in the Harvey-Shack model can be derived from the ABg model parameters. Between these two models, the deviation exists at the “knee” part of the log-log BRDF graph in all samples.

These observed results show that the peak value of BRDF is shifted to a larger scattering angle direction according to the increasing surface roughness. Also, we can understand that the specular reflection occurs more often at small surface roughness; on

the other hand, the diffuse reflection appears more at large surface roughness. Through large micro-scale rough surface sample such as samples D and E, we can see that the BRDF and ABg model are not appropriate to define the surface characteristics of the large micro-scale roughness. Also, we could predict that the surface texture can affect the scatter characteristics especially for the large micro-scale surface roughness.

In order to use scattering measurements to characterize large micro-scale surface roughness, a new theory or analysis method must be developed to analyze the scattering characteristics of surface. If so, standards for the micro-size roughness can be established to define the various surface characteristics.

## 6. FUTURE WORKS

The following suggestions about this thesis are made for further research in the area of the surface scatter investigation:

1. Continue the theoretical development on the scattering characterization of large micro-scale rough surfaces. This should include establishing a new theory or analysis method for defining surface characteristics. The wavelength of the light source could also be increased so that roughness/wavelength ratio places the sample characteristic in an appropriate range. This would be an important contribution to understanding the scattering phenomena of large micro-scale rough surfaces.

2. Equip the goniometer scattering measurement system with a stepper motor for measuring the scattering angle automatically. This can reduce the measuring time and provide more precise data.

3. Try to measure the scatter phenomena of anisotropic rough surfaces. The analyzed data in this thesis are only applied to isotropic surfaces. Therefore, the anisotropic surface should be analyzed to define the various scattering characteristics.

## LIST OF REFERENCES

- [1] Ament, W. S., "Toward a Theory of Reflection by a Rough Surface," Proc. IRE 41:142-146 (1953)
- [2] Twersky, V., "On Scattering and Reflection of Electromagnetic Waves by Rough Surfaces," IRE trans., 81-90 (1957)
- [3] Bennet, H. E., and J. O. Proteus, "Relation between Surface Roughness and Specular Reflection at Normal incidence," J. Opt. Soc. Am. Vol51: 123-129 (1961)
- [4] Beckman. P., and Spizzichino, A, "The Scattering of Electromagnetic Waves form Rough Surfaces," A Pergamon Press Book, (1963)
- [5] F. E. Nicodemus, "Geometrical Considerations and Nomenclature for Reflectance," U.S. NBS Monograph 160 (1977)
- [6] Ross McCluney, "Introduction to Radiometry and Photometry," Artech House, INC., (1994)
- [7] Edward F.Zalewski, "Chapter 24. Radiometry and photometry in Handbook of Optics, volume II," McGrawHill INC (1995)
- [8] Lisa M. Farrier, "Influence of surface roughness on the specular reflectance of low gloss coating using bidirectional reflectance measurements," Thesis, Air Force Research Laboratory (2006)
- [9] John C.Stover, "Chapter 26. Scatterometers in Handbook of Optics, Volume II," McGrawHill INC (1995)

- [10] J. C. Stover, "Optical scattering, measurement and analysis, 3rd edition," Bellingham, WA: SPIE Optical Engineering Press (2012)
- [11] Photon Engineering, "Stray Light: Reality Collides with Theory," College of optical sciences. (2009)
- [12] J. E. Harvey, "Light Scattering Characteristics of Optical Surfaces," PhD Dissertation, University of Arizona, (1976).
- [13] Laser 2000, "FRED User Manual," Laser 2000 Gmbh, (2007)
- [14] ASAP, "Technical Guide: Scattering ASAP," Breault Research Organization, INC, Tucson, AZ 85715 (2012)
- [15] Sam Richardson, "Characterization of Surface Degradation by Laser Light Scattering," S-DLE Center laboratory
- [16] Engineering, Photon, "Stray Light: Reality Collides with Theory," College of Optical Sciences, (2009)
- [17] William S. Bickel, "Optical system for light scattering experiments," Applied Optics, Vol 18: No. 11, 1707-1709 (1979):
- [18] Rosana Montes, Carlos Ureña. "An Overview of BRDF Models," University of Granada, LSI Technical Reports: 26 pages (2012)
- [19] Thomas A. Germer, Clara C. Asmail, "A goniometric optical scatter instrument for bidirectional reflectance distribution function measurements with out-of-plane and planimetry capability," Proc. SPIE 3141: 220-231 (1997)
- [20] U. Akgun, W. Anderson, A. S. Ayan, E. Gulmez, M. Miller, Y. Onel, I. Schmidt, D. Winn, "CMS- -HF PMT Test and Quality Control System," University of Iowa, Iowa

City, USA , Iowa State University, Ames, USA , Bogazici University, Istanbul,  
Turkey, Fairfield University, Fairfield, USA

[21] Jared M. Maxson, “Using a Lock-In Amplifier,” Lehigh University Department of  
Physics, Feb 14(2008)

[22] Stanford Research Systems, “Model SR830 DSP Lock-In Amplifier manual,”  
October (2011)

[23] National Instruments, “User guide and specifications NI USB-6008/6009 manual,”  
Feb 12 (2012)

[24] Zygo Corporation, “NewView 6200 & 6300 Operating Manual,” February (2006)

[25] Fredick M. Cady, Donald R. Bjork, Jeffrey Rifkin, John C. Stover. “BRDF error  
analysis,” SPIE 1165: 154-164 (1989)

[26] Squires, G. L. “Practical physics,” Cambridge University Press, Cambridge,  
UK(1985)

**APPENDICES**



## APPENDIX A

Calibration for the Neutral Density (ND) Filter

Optical density (OD) value is defined as

$$\text{Optical density (OD)} = -\log_{10}(I/I_0) \quad (12)$$

where  $I$  indicates the laser power passed through the neutral density filter, and  $I_0$  indicates the incident laser power.

**Table 5** Optical density value for each ND filter. The percent error is with respect to the given OD filter value.

<b>Incident Power</b>	524.14	Unit: $\mu\text{W}$		
<b>Number of times</b>	with ND filter	with ND filter	with ND filter	with ND filter
	<b>0.8 OD</b>	<b>1 OD</b>	<b>2 OD</b>	<b>3 OD</b>
<b>1</b>	80.7	50.1	5.04	0.512
<b>2</b>	80.3	51.4	5.16	0.511
<b>3</b>	81.2	50.7	5.08	0.519
<b>4</b>	79.2	51.1	5.11	0.513
<b>5</b>	80.1	50.5	5.16	0.518
<b>6</b>	79.2	50.3	5.02	0.508
<b>7</b>	80.6	49.2	5.06	0.516
<b>8</b>	79.5	50.6	5.18	0.506
<b>9</b>	81.2	48.6	5.16	0.516
<b>10</b>	79.5	50.4	5.08	0.512
<b>11</b>	80.3	49.2	5.16	0.507
<b>12</b>	80.1	50.2	5.14	0.516
<b>13</b>	80.2	49.4	5.03	0.512
<b>14</b>	79.7	50.7	5.18	0.509
<b>15</b>	81.1	51.3	5.14	0.517
<b>Average</b>	80.2	50.2	5.11	0.513
<b>Optical Density</b>	0.815±0.007	1.018±0.009	2.011±0.005	3.009±0.005
<b>Error (%)</b>	1.914	1.834	0.537	0.317

**Table 6** Optical density value for two ND filters. The percent error is with respect to the given OD filter value.

<b>Incident Power</b>	524.14	Unit: $\mu\text{W}$			
<b>Number of times</b>	with ND filter	with ND filter	with ND filter	with ND filter	with ND filter
	<b>2 +3 OD</b>	<b>1+3 OD</b>	<b>0.8 +1 OD</b>	<b>0.8 +2 OD</b>	<b>0.8 +3 OD</b>
<b>1</b>	0.0049	0.051	8.874	0.838	0.076
<b>2</b>	0.0051	0.048	8.724	0.846	0.085
<b>3</b>	0.0050	0.050	8.865	0.839	0.075
<b>4</b>	0.0055	0.051	8.825	0.824	0.077
<b>5</b>	0.0054	0.049	8.711	0.843	0.076
<b>6</b>	0.0049	0.051	8.689	0.848	0.085
<b>7</b>	0.0050	0.050	8.881	0.849	0.081
<b>8</b>	0.0049	0.052	8.657	0.851	0.076
<b>9</b>	0.0049	0.051	8.952	0.851	0.088
<b>10</b>	0.0052	0.051	8.788	0.852	0.085
<b>11</b>	0.0051	0.050	8.879	0.856	0.081
<b>12</b>	0.0053	0.048	8.793	0.853	0.087
<b>13</b>	0.0052	0.049	8.841	0.856	0.082
<b>14</b>	0.0054	0.051	8.745	0.854	0.084
<b>15</b>	0.0051	0.052	8.782	0.850	0.079
<b>Average</b>	0.0051	0.050	8.800	0.847	0.081
<b>Optical Density</b>	$5.010 \pm 0.005$	$4.018 \pm 0.009$	$1.775 \pm 0.012$	$2.791 \pm 0.004$	$3.810 \pm 0.005$
<b>Error (%)</b>	0.192	0.454	1.392	0.307	0.270

## APPENDIX B

LabView programming source

Main GUI for the BRDF data

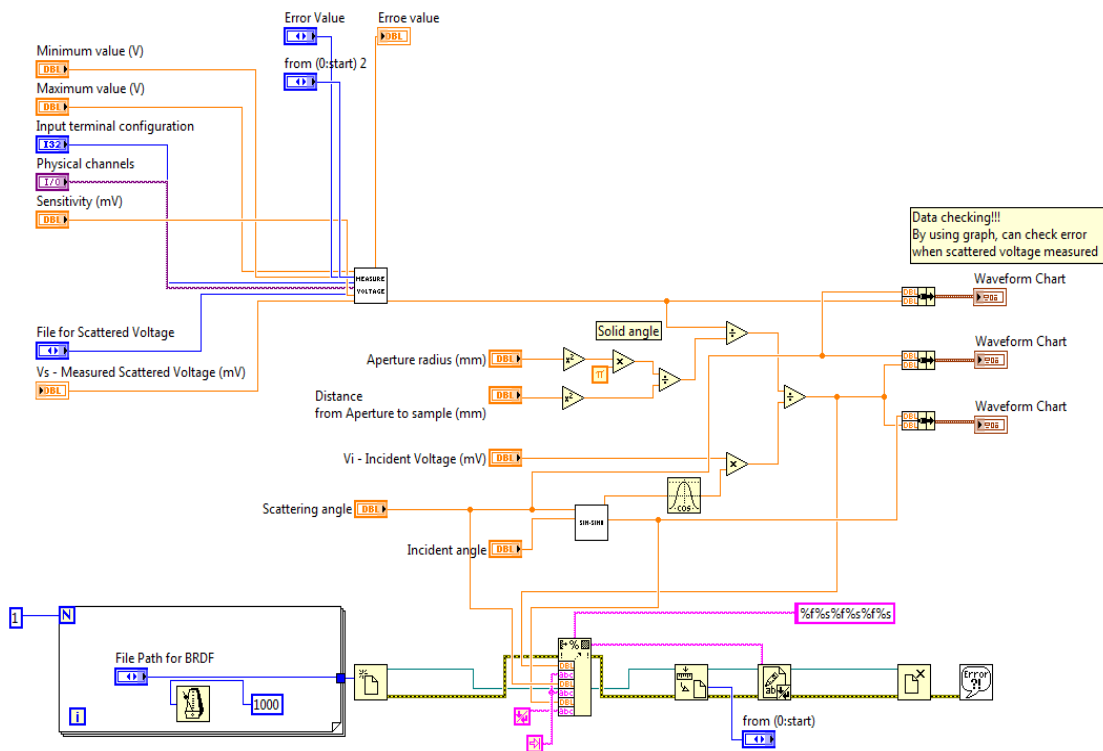


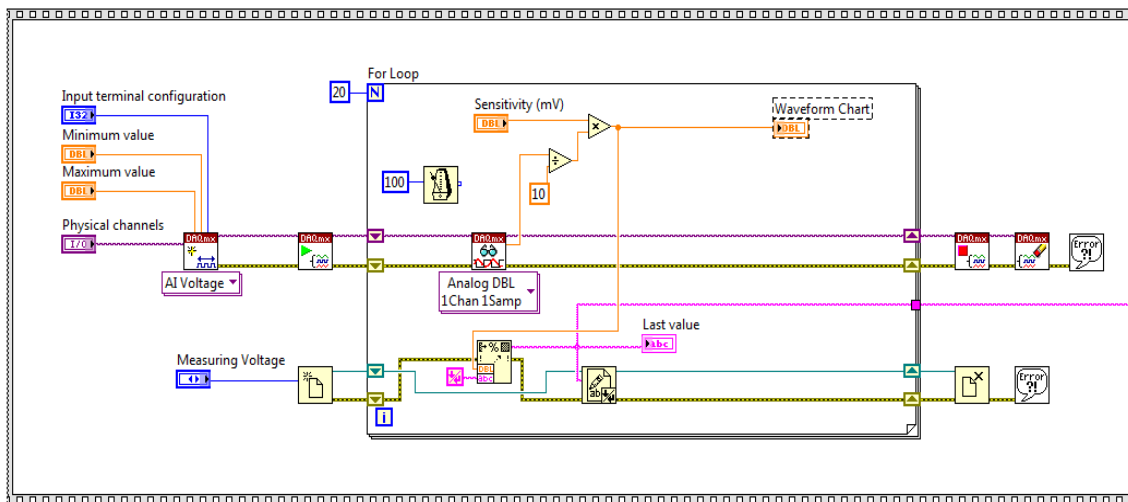
Figure 38 GUI programming source for calculating the BRDF using the scattered voltage

Sub VI's



Measured scattered voltage and error value

(Two figures are one sequence, not separated.)



(Continue...)

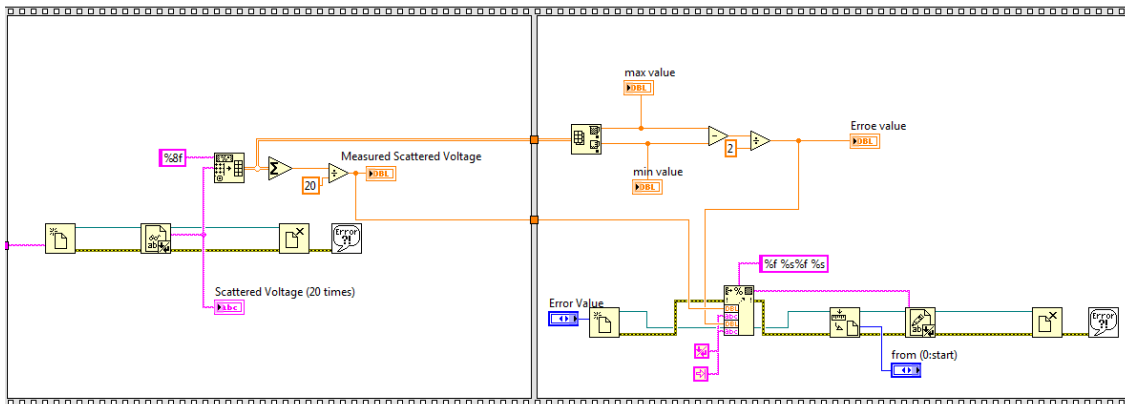


Figure 39 Sub VI for measuring the incident voltage and the scattered voltage

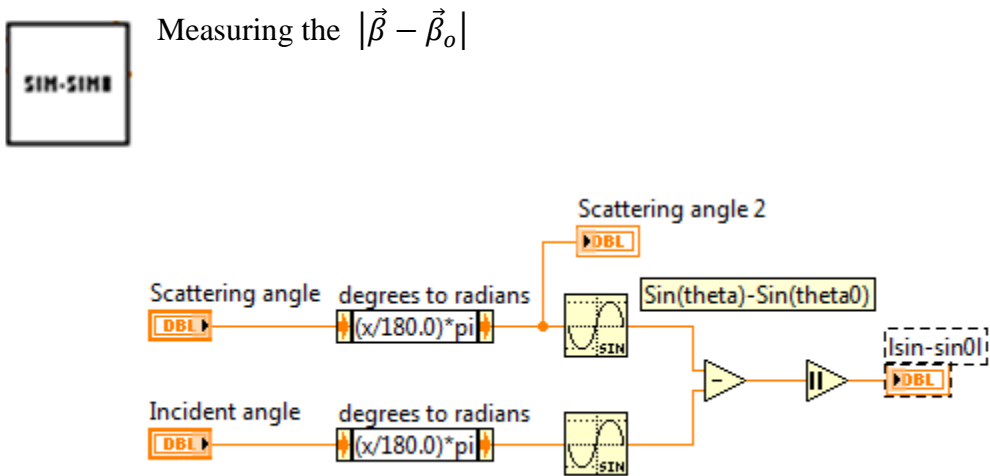
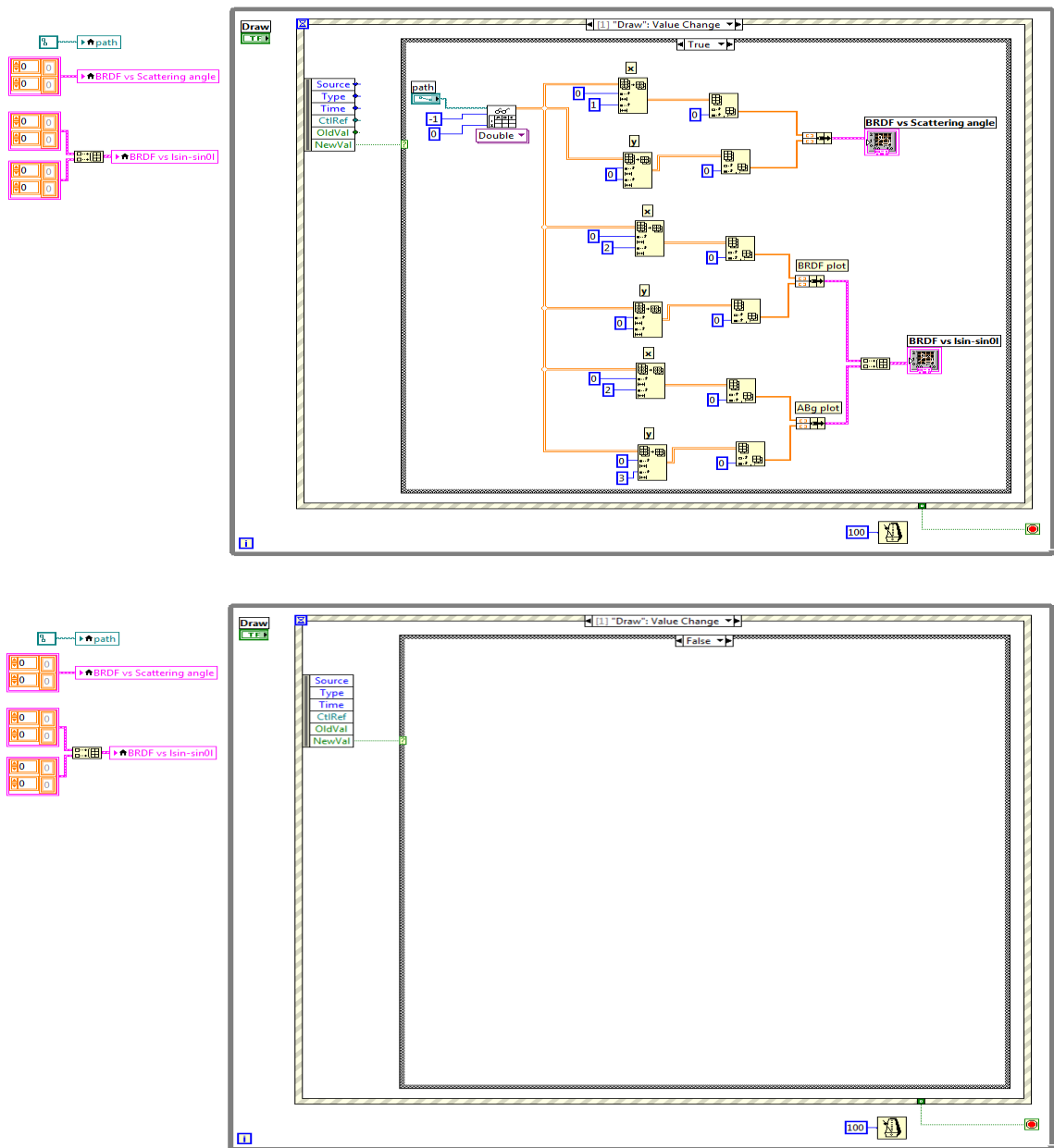
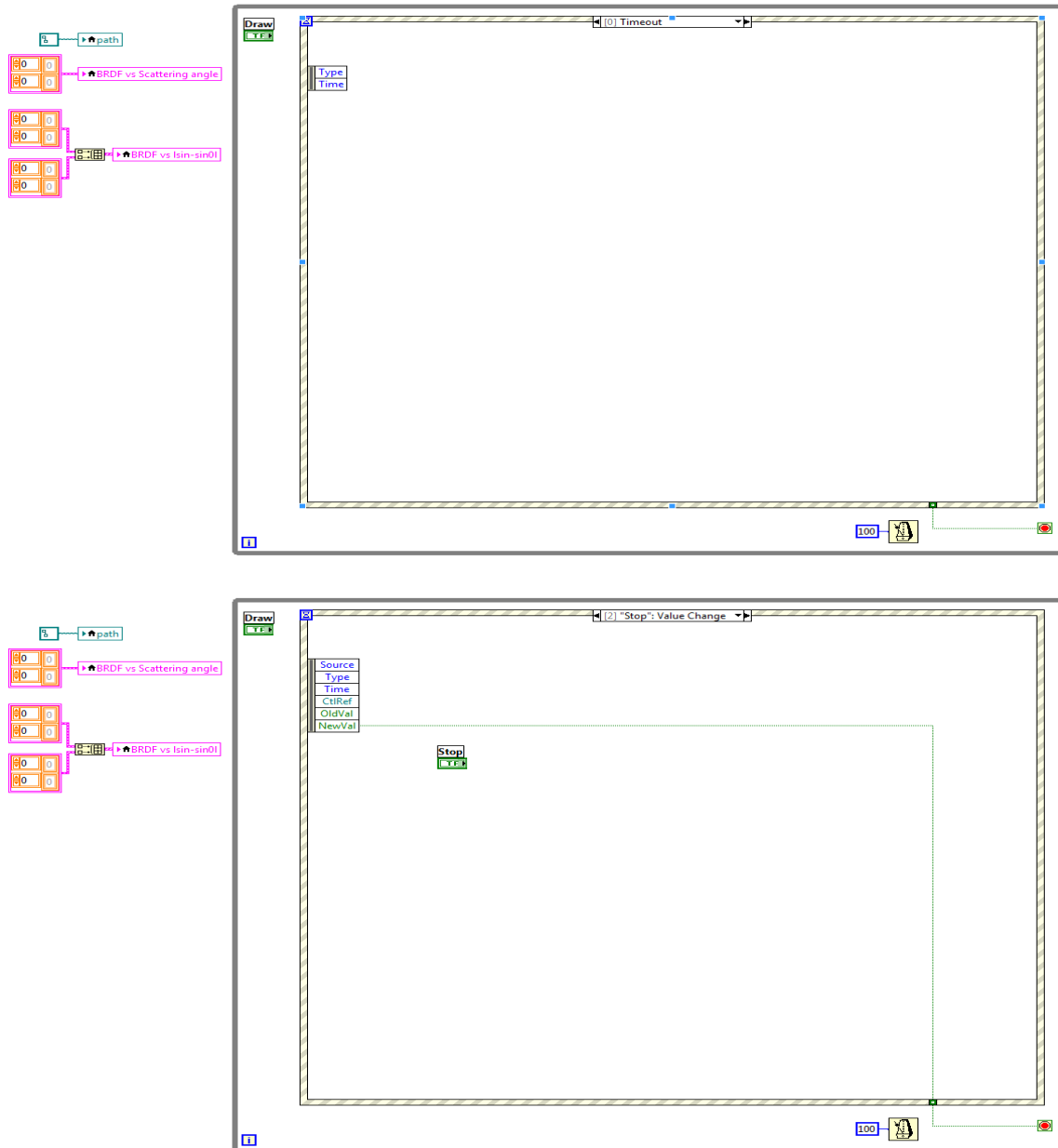


Figure 40 Sub VI for  $|\vec{\beta} - \vec{\beta}_o|$

GUI for drawing the BRDF graphs (Part A and Part B are one program)



**Figure 41** Programming source for drawing the BRDF graphs using the text file. (Part A)



**Figure 42** Programming source for drawing the BRDF graphs using the text file. (Part B)

## Front panel

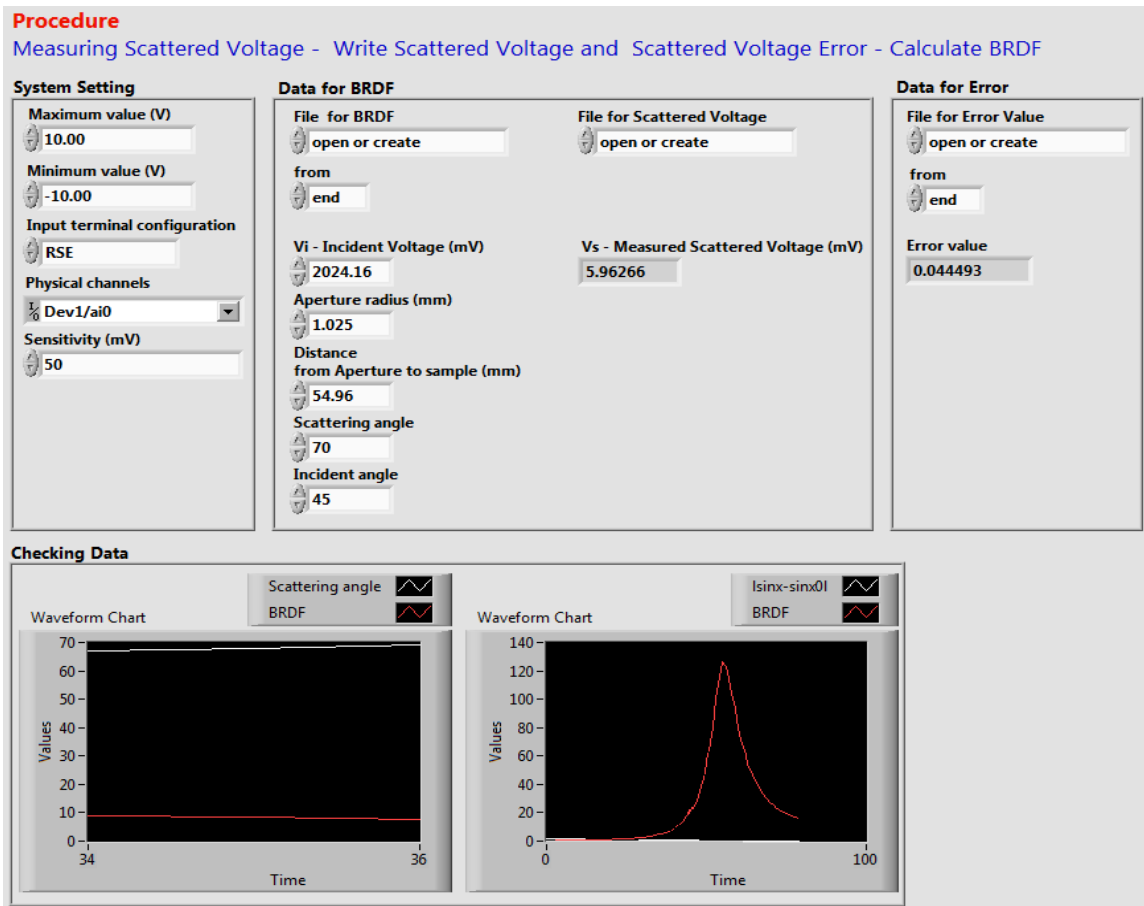


**Figure 43** Front panel of GUI for the BRDF



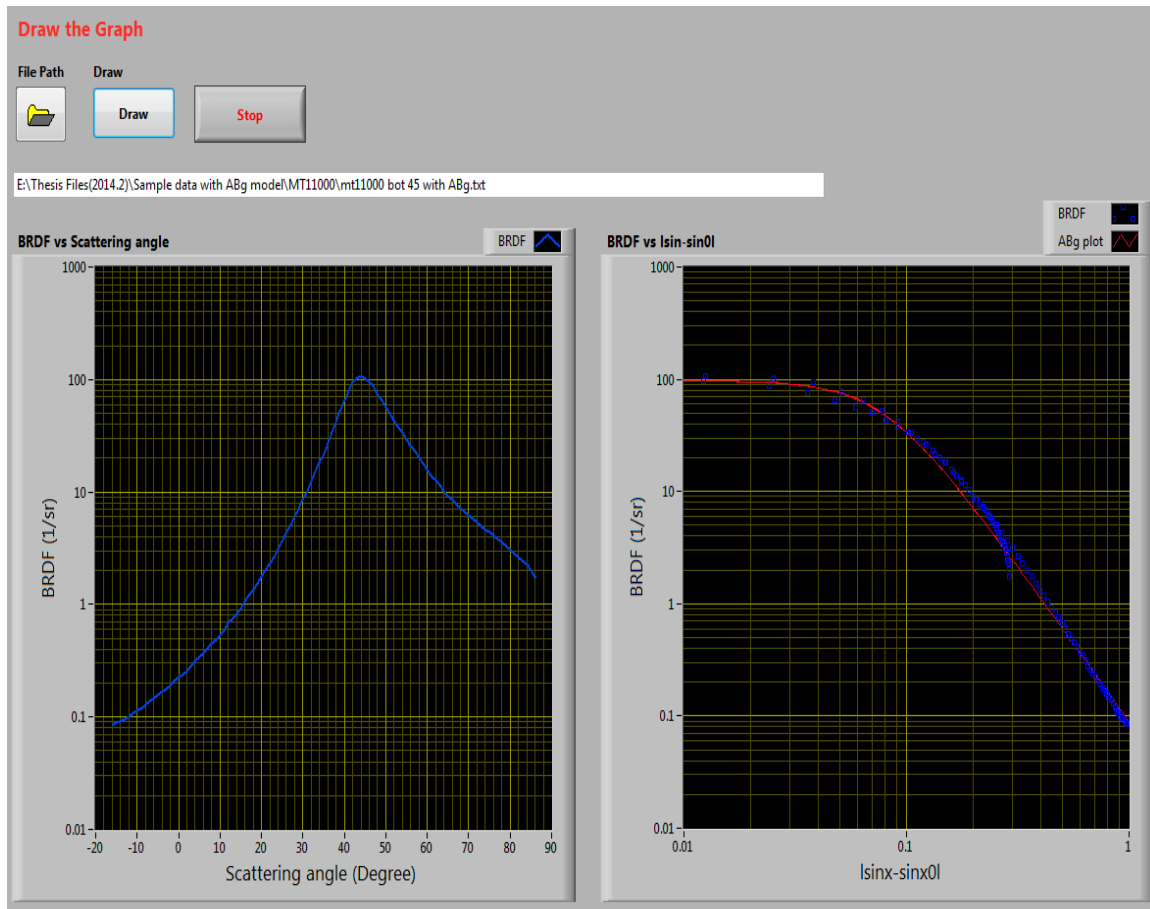


**Figure 44** Front panel of GUI for drawing the BRDF graphs

## APPENDIX C

The BRDF data fit to the ABg scattering model

This appendix contains graphs of BRDF data for all samples in this study. A fit curve of the ABg model is shown for each data set and values of A, B, and g are provided.

### Sample A

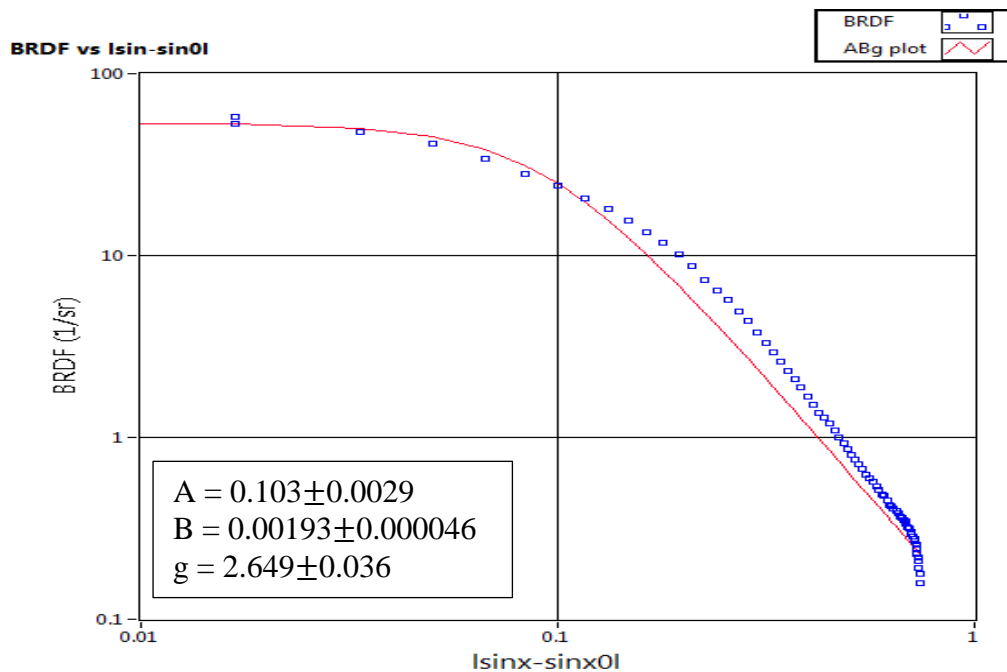


**Figure 45** The ABg model of Sample A at the 15° incident angle

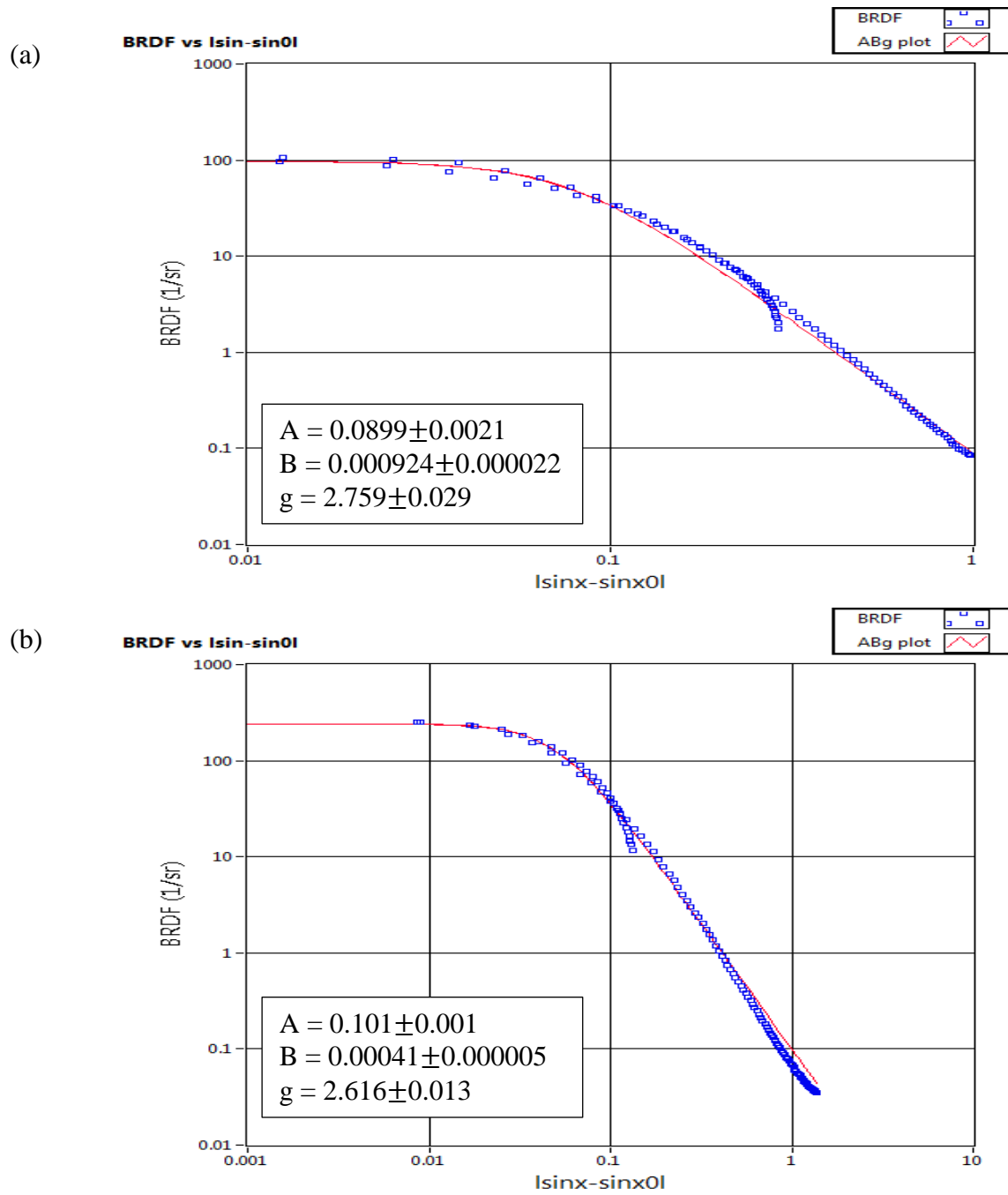


**Figure 46** The ABg model of Sample A at the (a) 45° and (b) 60° incident angles

Sample B

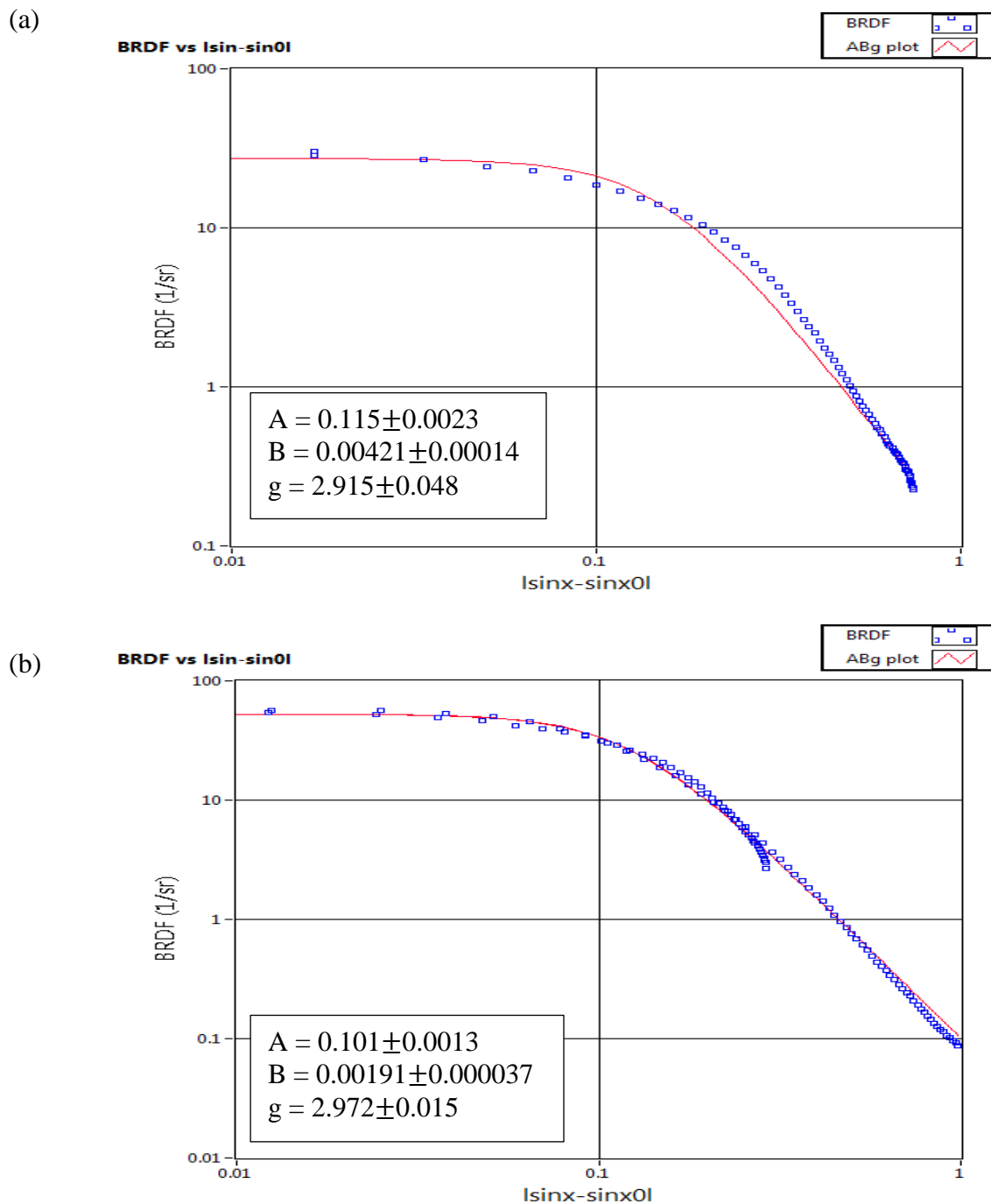


**Figure 47** The ABg model of Sample B at the (a)  $15^\circ$  and (b)  $45^\circ$  incident angles

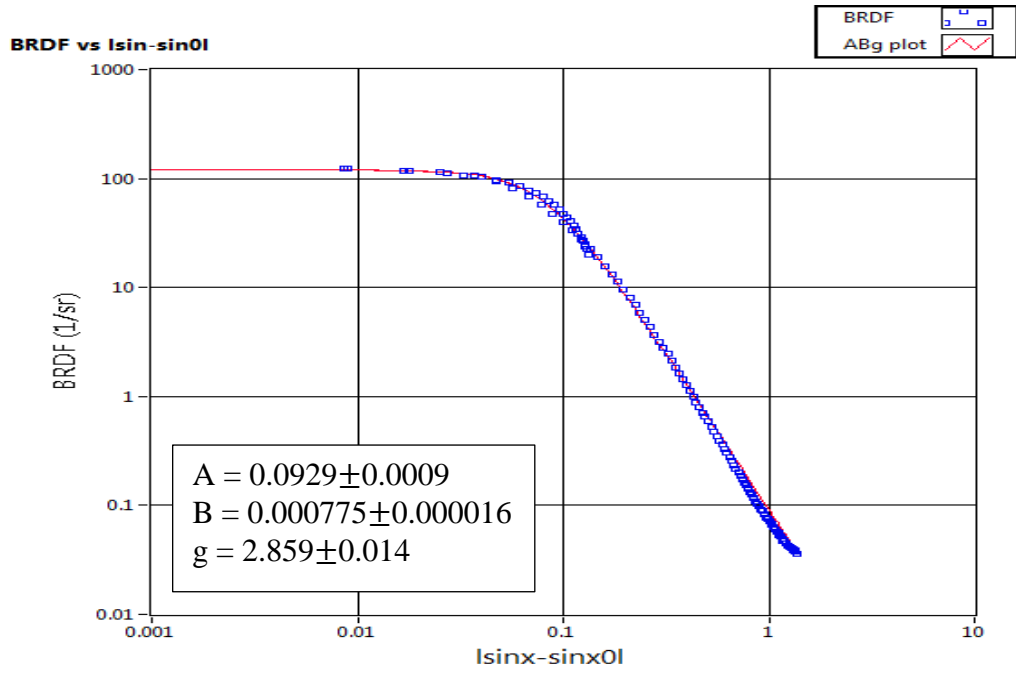


**Figure 48** The ABg model of Sample B at the 60° incident angle

### Sample C

In sample C, the geometrical specular angle is shifted from  $45^\circ$  to  $46^\circ$  and  $60^\circ$  to  $64^\circ$  respectively. The ABg models are well-fitted in the measured BRDF data compared with other samples. The g values are bigger than 3 at three different incident angle.

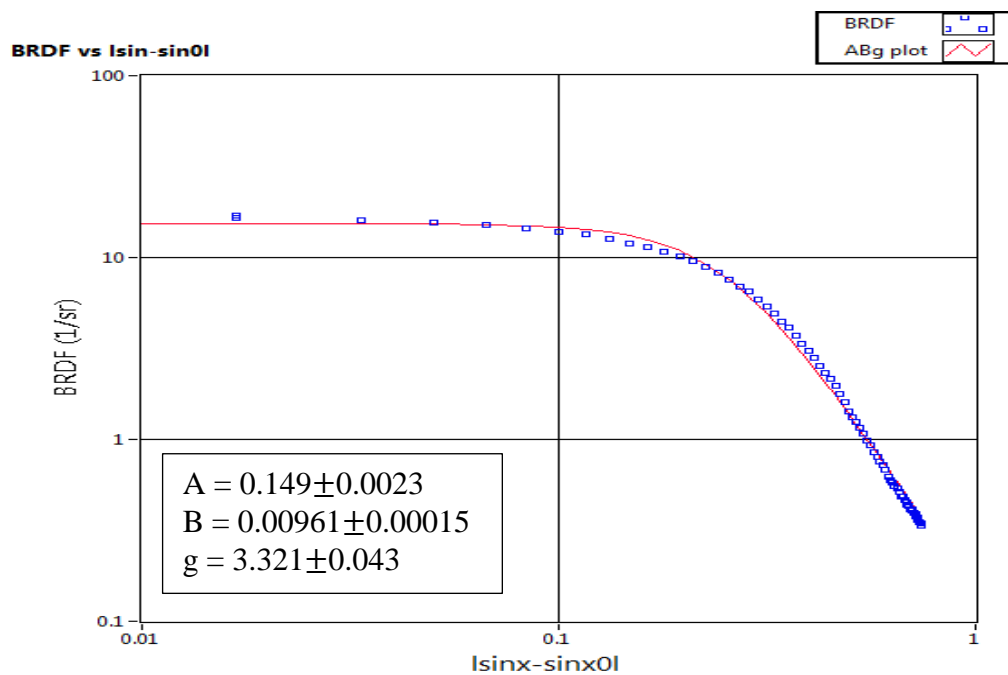


**Figure 49** The ABg model of Sample C at the  $15^\circ$  incident angle

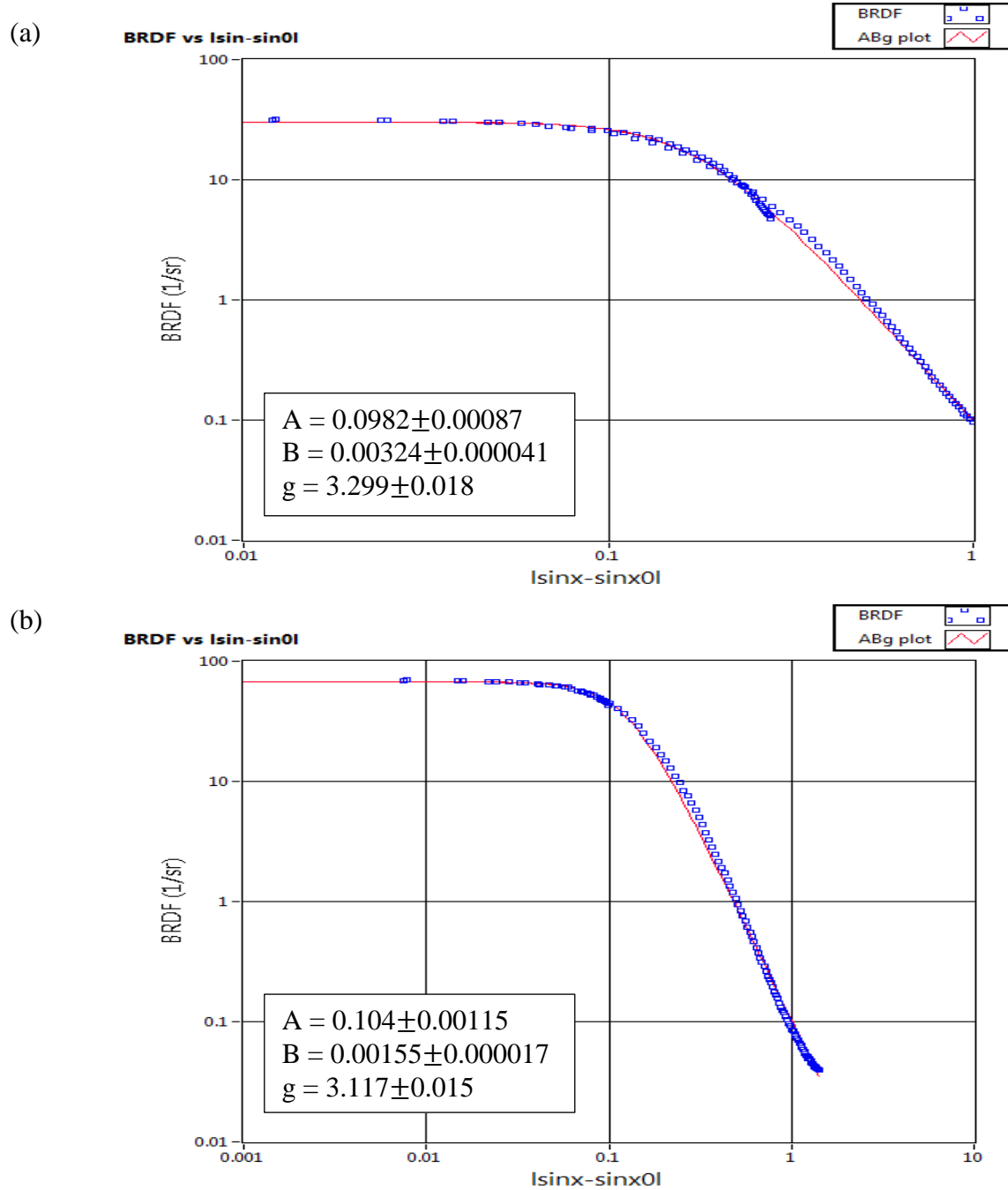


**Figure 50** The ABg model of Sample C at the (a)  $45^\circ$  and (b)  $60^\circ$  incident angles. The specular angles are shifted to  $46^\circ$  and  $64^\circ$  respectively

### Sample D

In sample D, the geometrical specular angle is shifted from  $45^\circ$  to  $52^\circ$  and  $60^\circ$  to  $70^\circ$  respectively. In the  $52^\circ$  specular angle, there is no branch, but a branch is appeared in the  $70^\circ$  specular angle. The  $g$  values at  $15^\circ$  and  $60^\circ$  incident angle are bigger than 3.

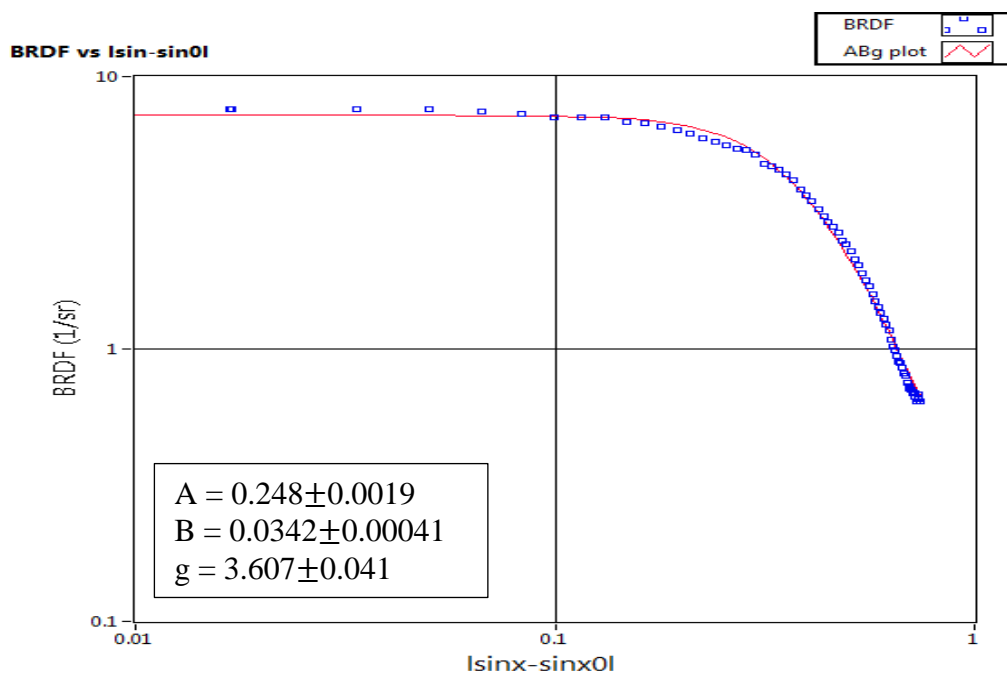


**Figure 51** The ABg model of Sample D at the  $15^\circ$  incident angle



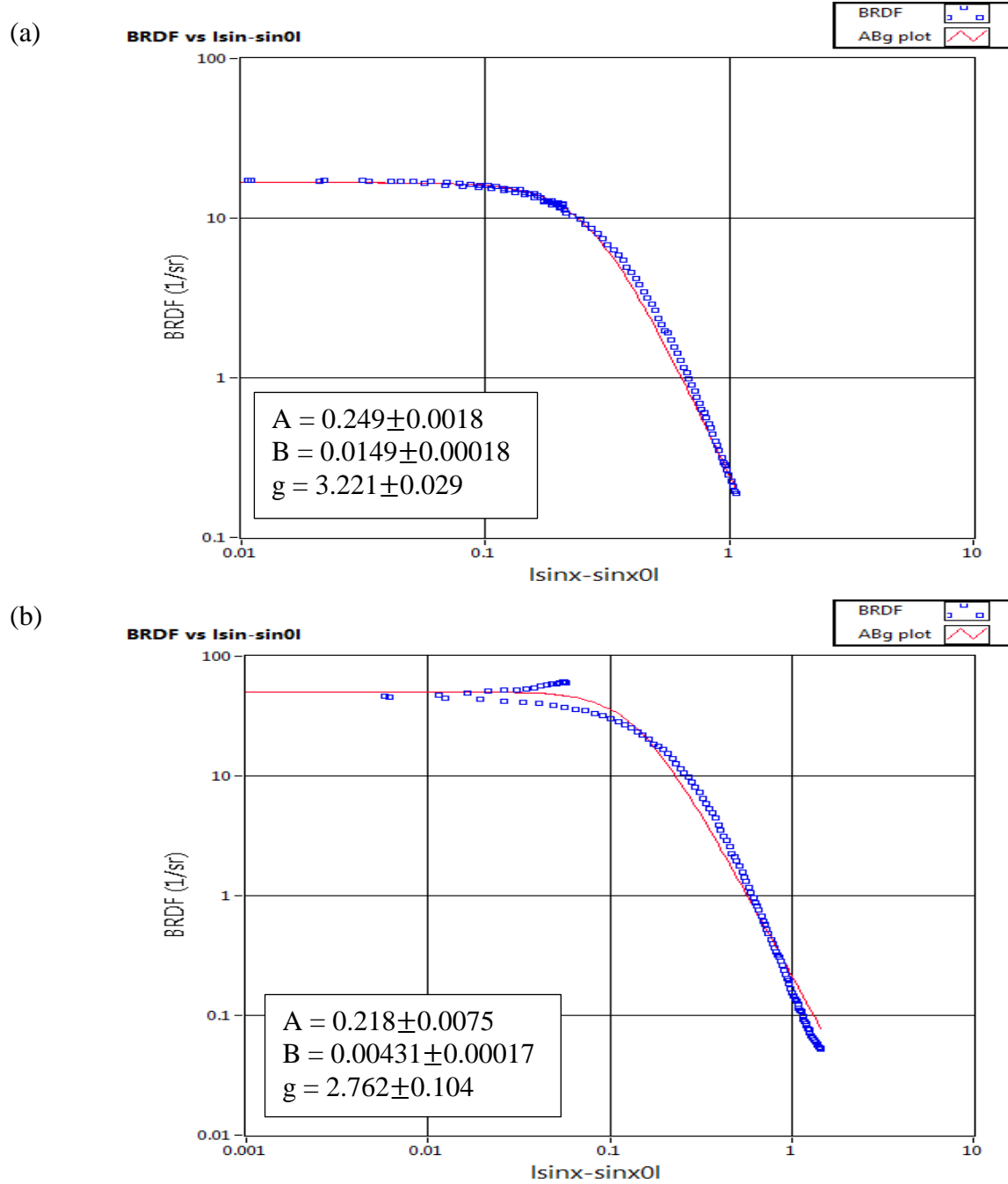


**Figure 52** The ABg model of Sample D at the (a)  $45^\circ$  and (b)  $60^\circ$  incident angles. The specular angles are shifted to  $46^\circ$  and  $64^\circ$  respectively.

### Sample E

In sample E, the geometrical specular angle is shifted from  $45^\circ$  to  $52^\circ$  and  $60^\circ$  to  $70^\circ$  respectively. After the specular angles are shifted, the branch exists at the  $45^\circ$  and  $60^\circ$  incident angles.

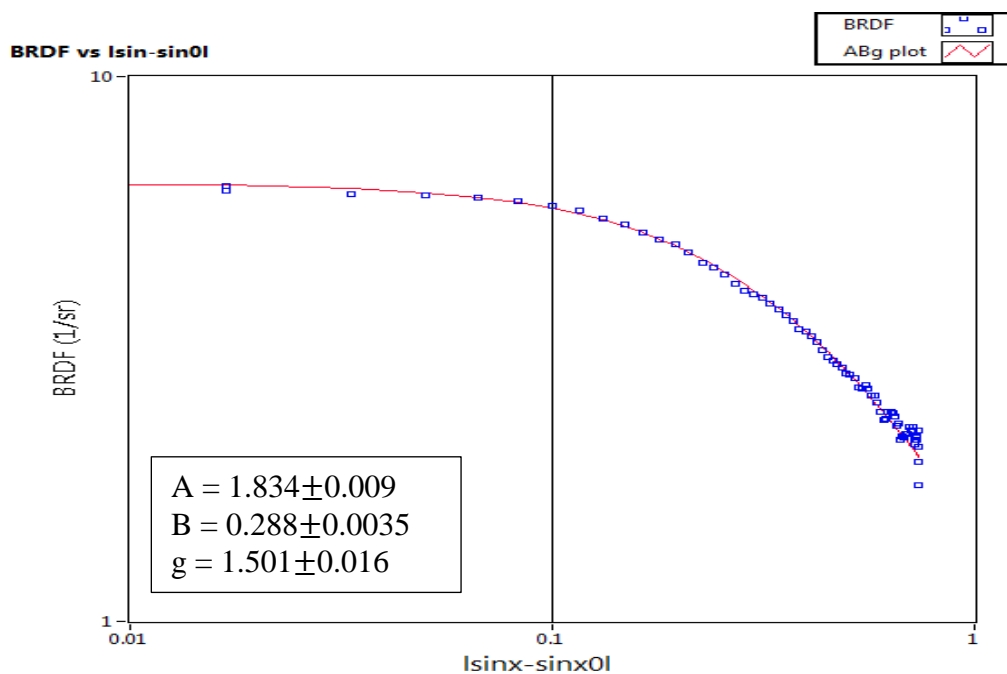


**Figure 53** The ABg model of Sample E at the  $15^\circ$  incident angle

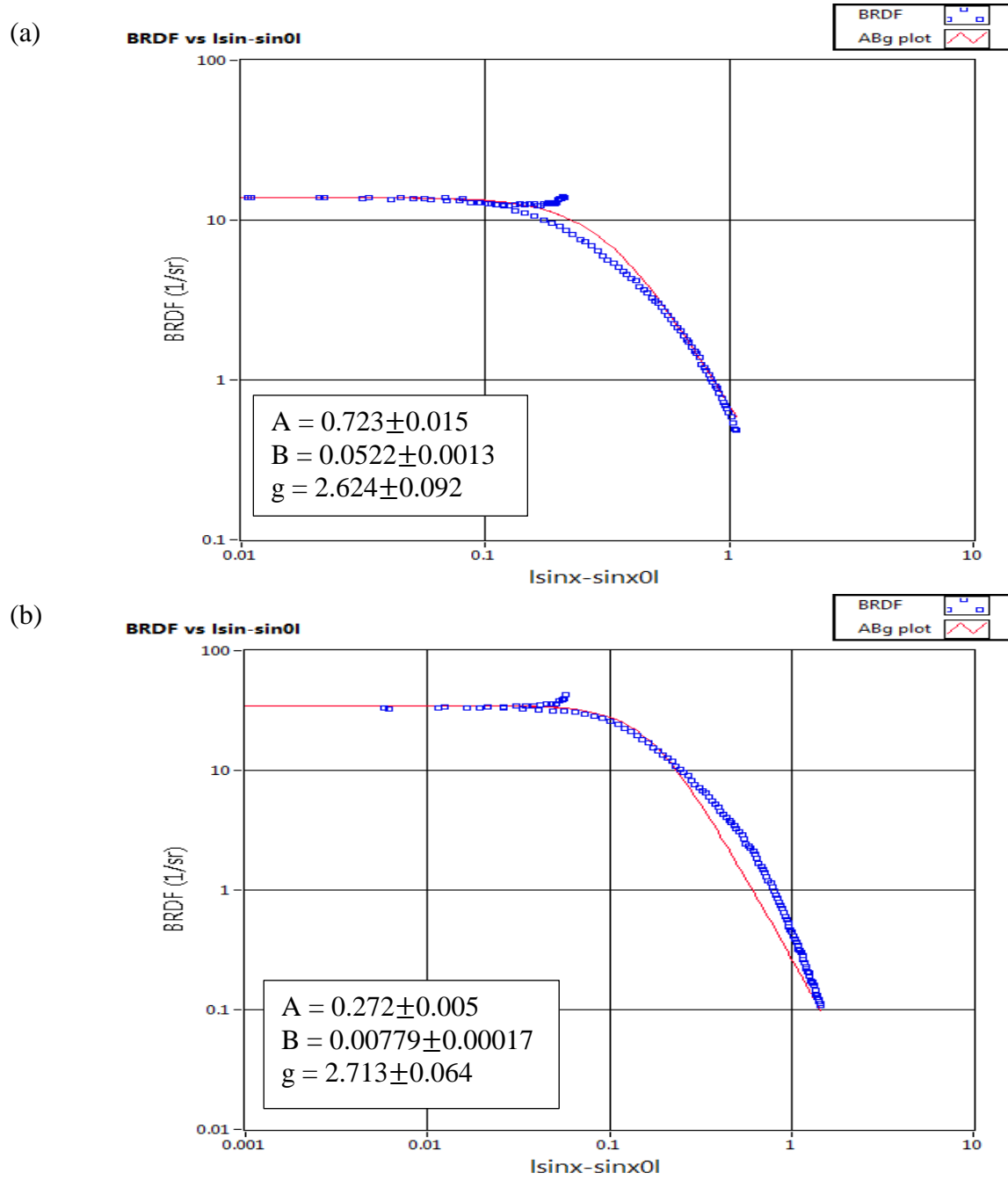


**Figure 54** The ABg model of Sample E at the (a)  $45^\circ$  and (b)  $60^\circ$  incident angles. The specular angles are shifted to  $46^\circ$  and  $64^\circ$  respectively.

## APPENDIX D

### Comparison of the ABg model with the Harvey-Shack model

In section 2.3, the Harvey-Shack scattering model is discussed. Parameters  $b_0$ ,  $S$ , and  $L$  of the Harvey-Shack model can be derived by using the ABg model parameters. There is a deviation between these two models for some of the samples studied. Graphs are shown comparing each of these BRDF models.

#### Sample A

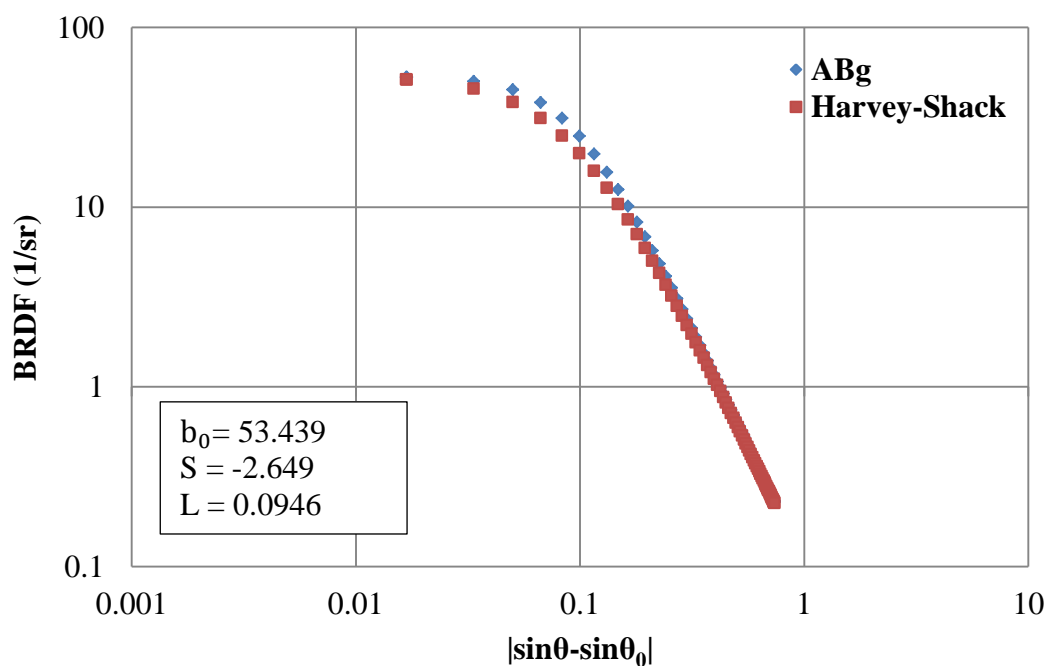


**Figure 55** Comparison of the Harvey-Shack model with the ABg model of Sample A at the  $15^\circ$  incident angle

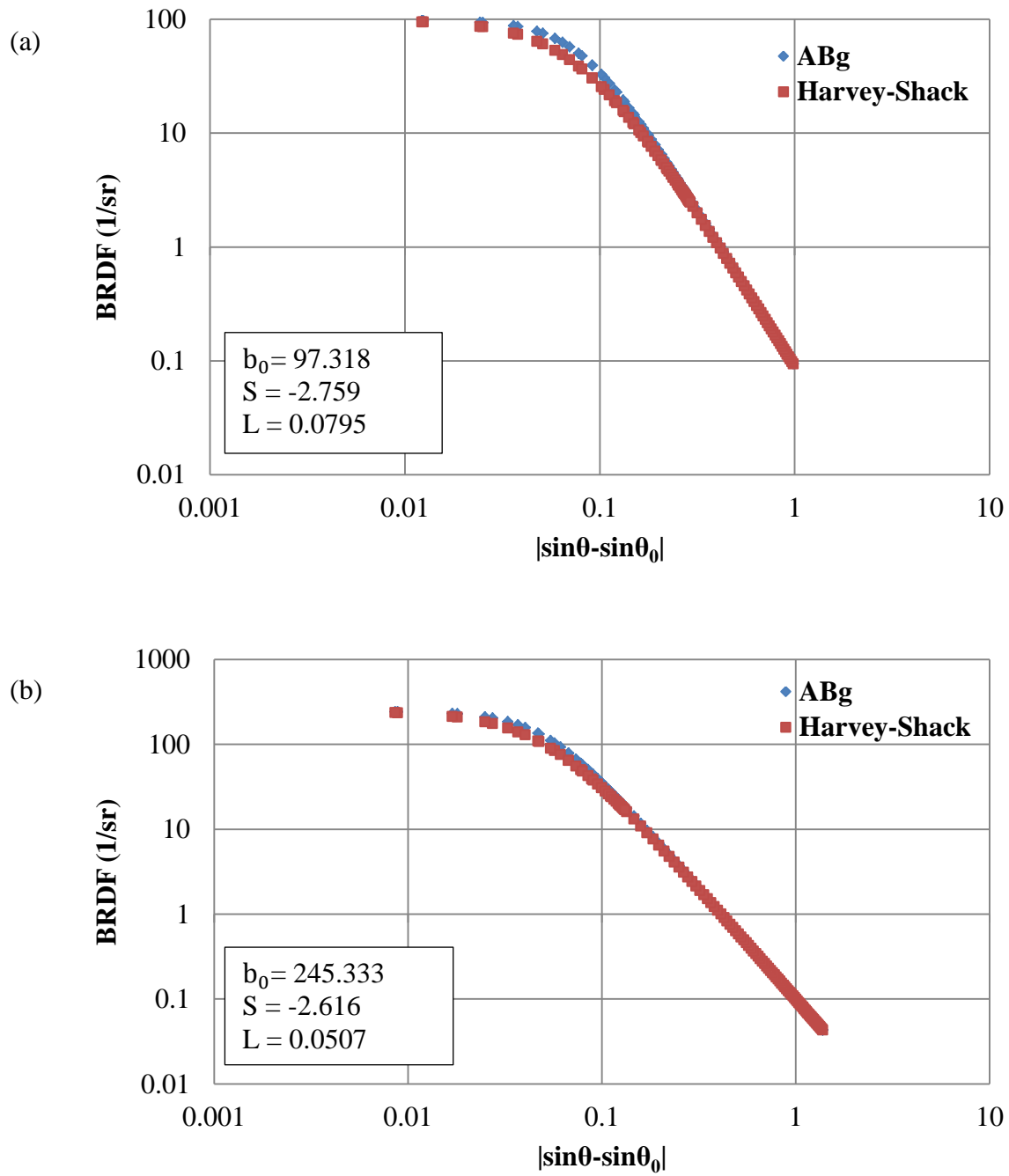


**Figure 56** Comparison of the Harvey-Shack model with the ABg model of Sample A at the (a) 45° and (b) 60° incident angles

Sample B

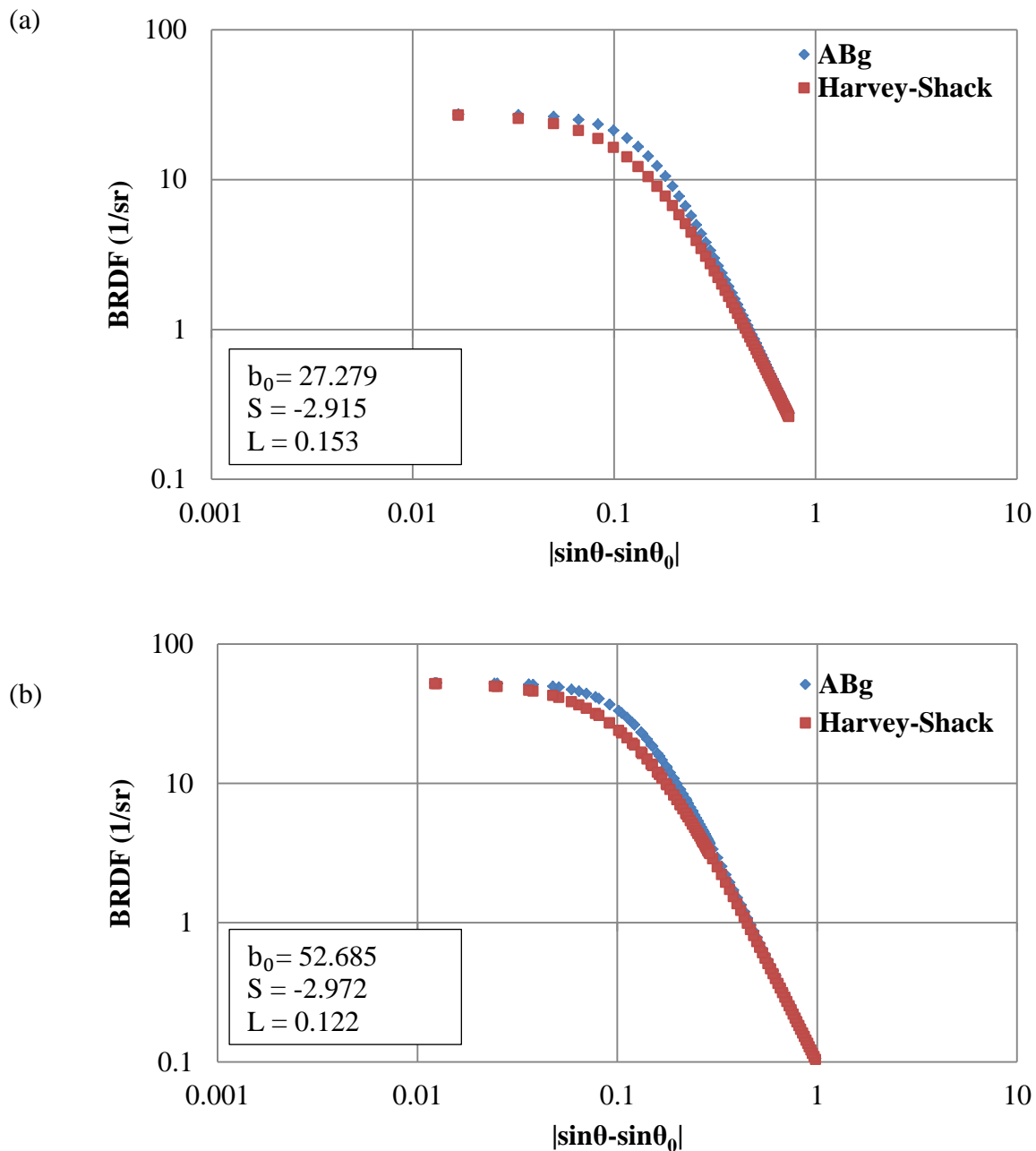


**Figure 57** Comparison of the Harvey-Shack model with the ABg model of Sample B at the (a) 15° and (b) 45° incident angles

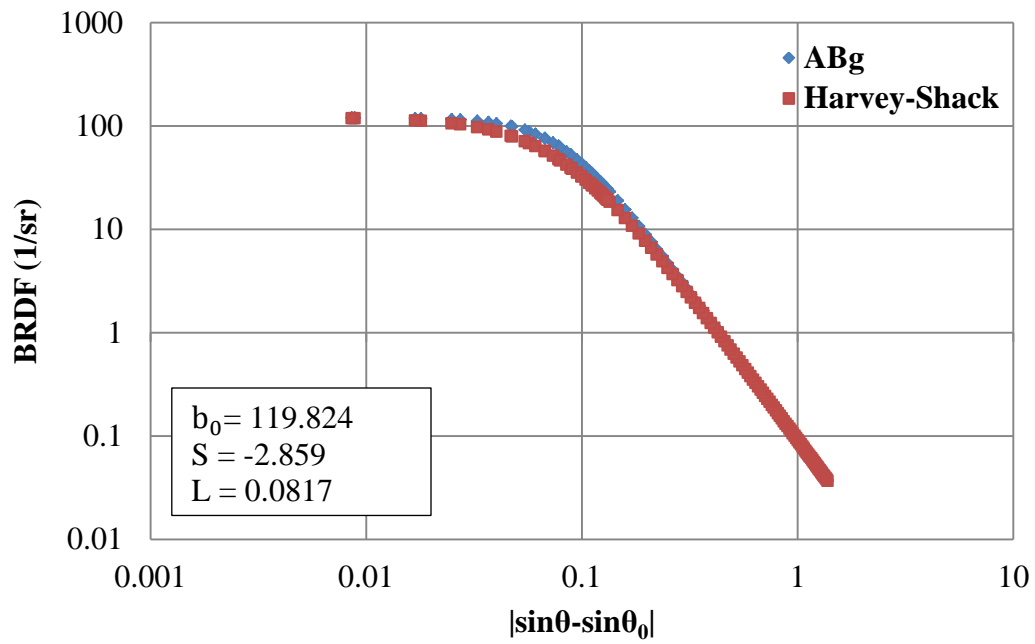


**Figure 58** Comparison of the Harvey-Shack model with the ABg model of Sample B at the 60° incident angle

Sample C

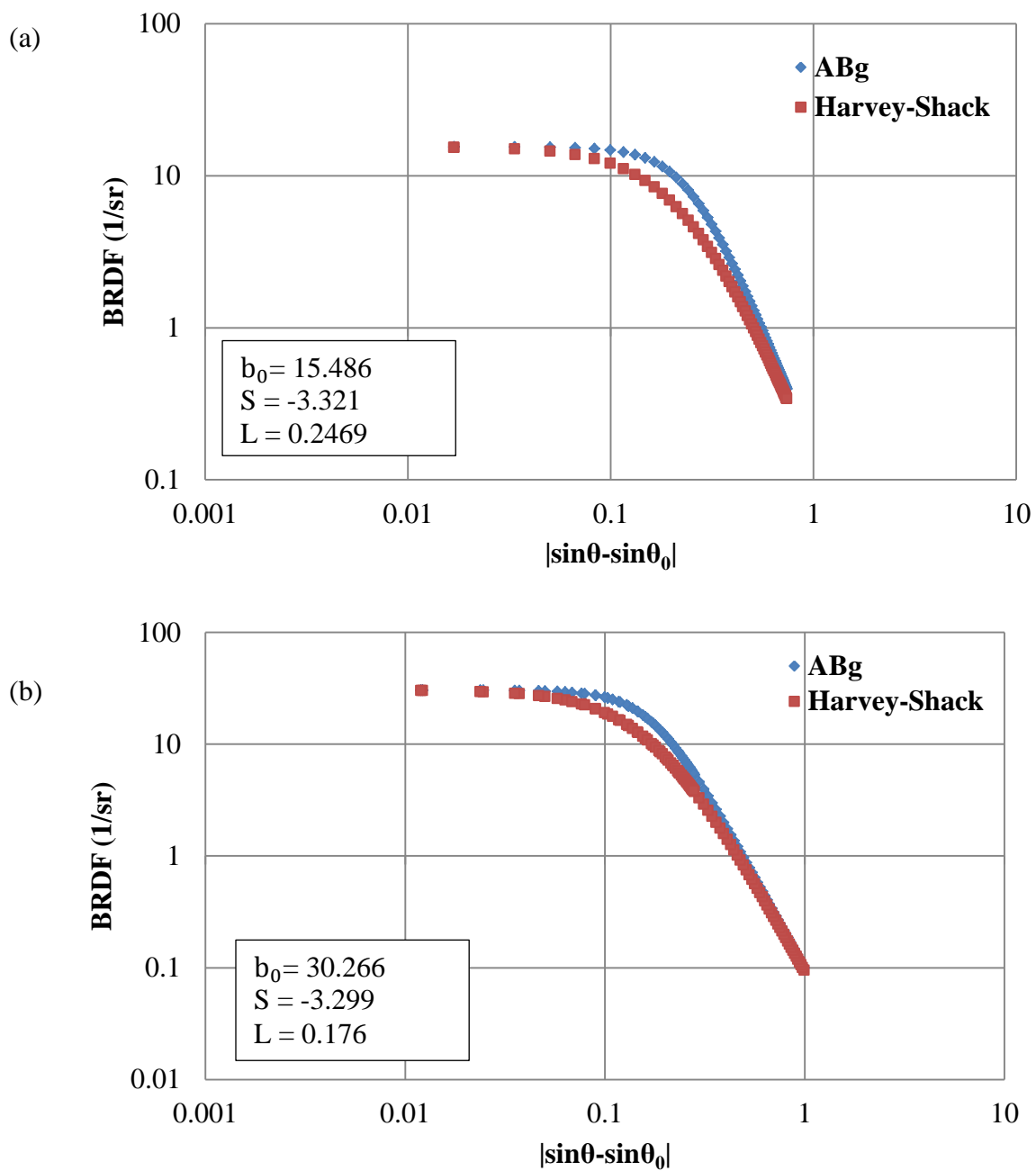


**Figure 59** Comparison of the Harvey-Shack model with the ABg model of Sample C at the (a) 15° and (b) 45° incident angles



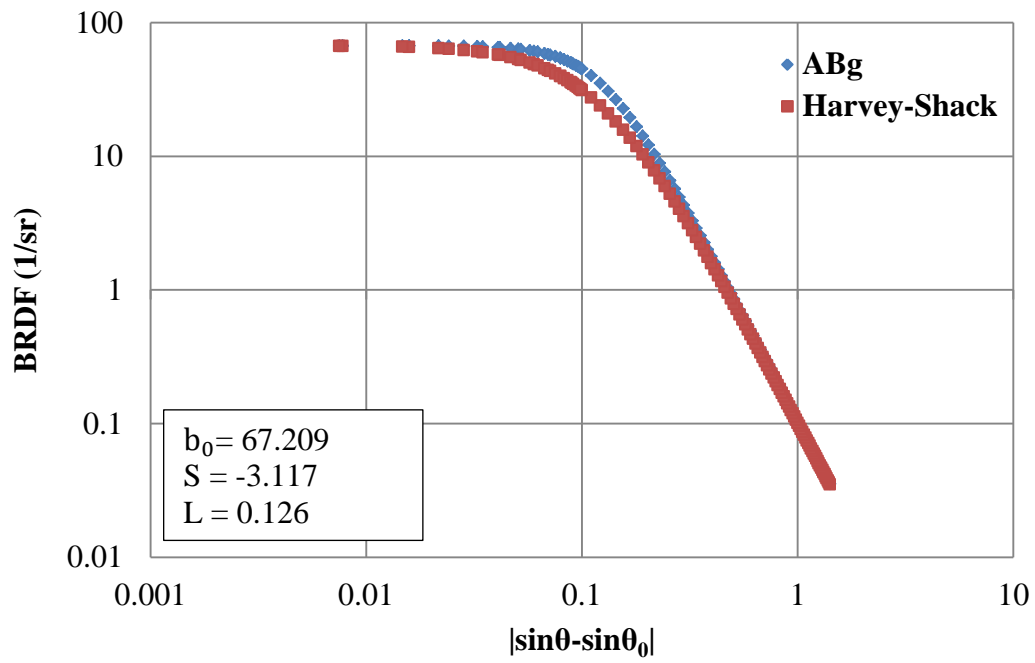


**Figure 60** Comparison of the Harvey-shack model with the ABg model of Sample C at the 60° incident angle

Sample D

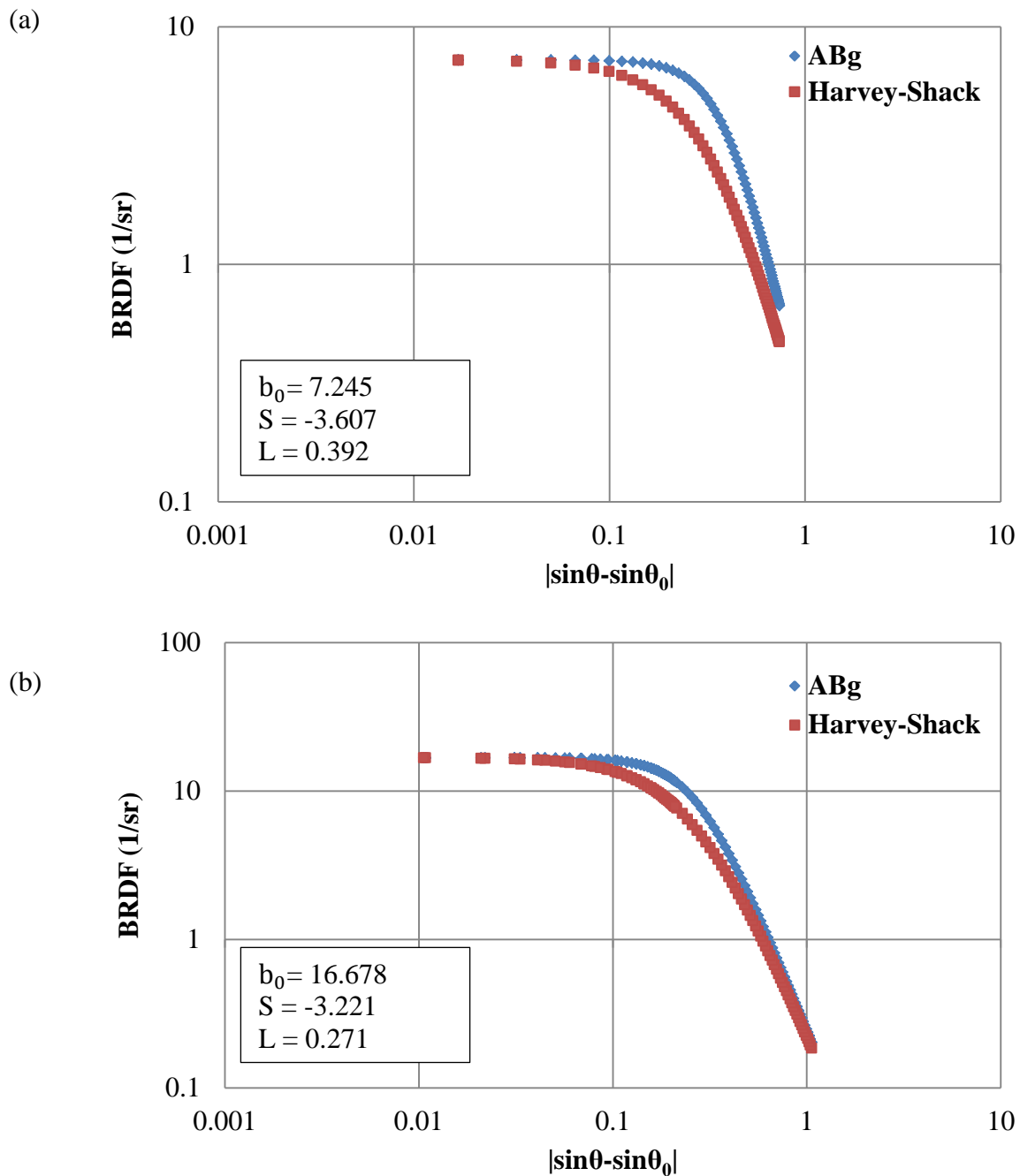


**Figure 61** Comparison of the Harvey-Shack model with the ABg model of Sample D at the (a) 15° and (b) 45° incident angles

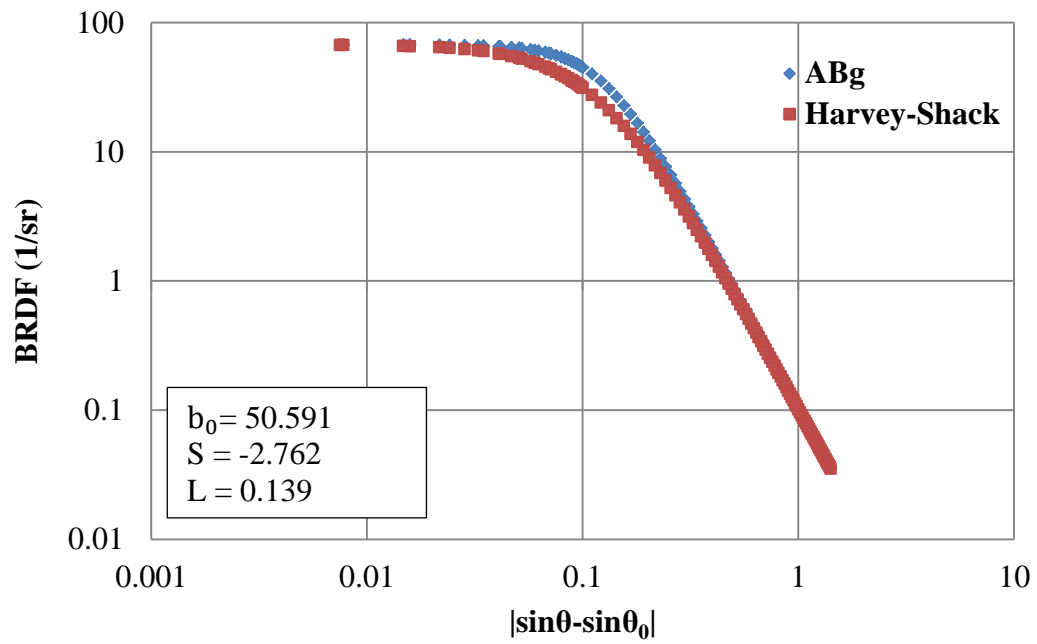


**Figure 62** Comparison of the Harvey-Shack model with the ABg model of Sample D at the 60° incident angle

Sample E

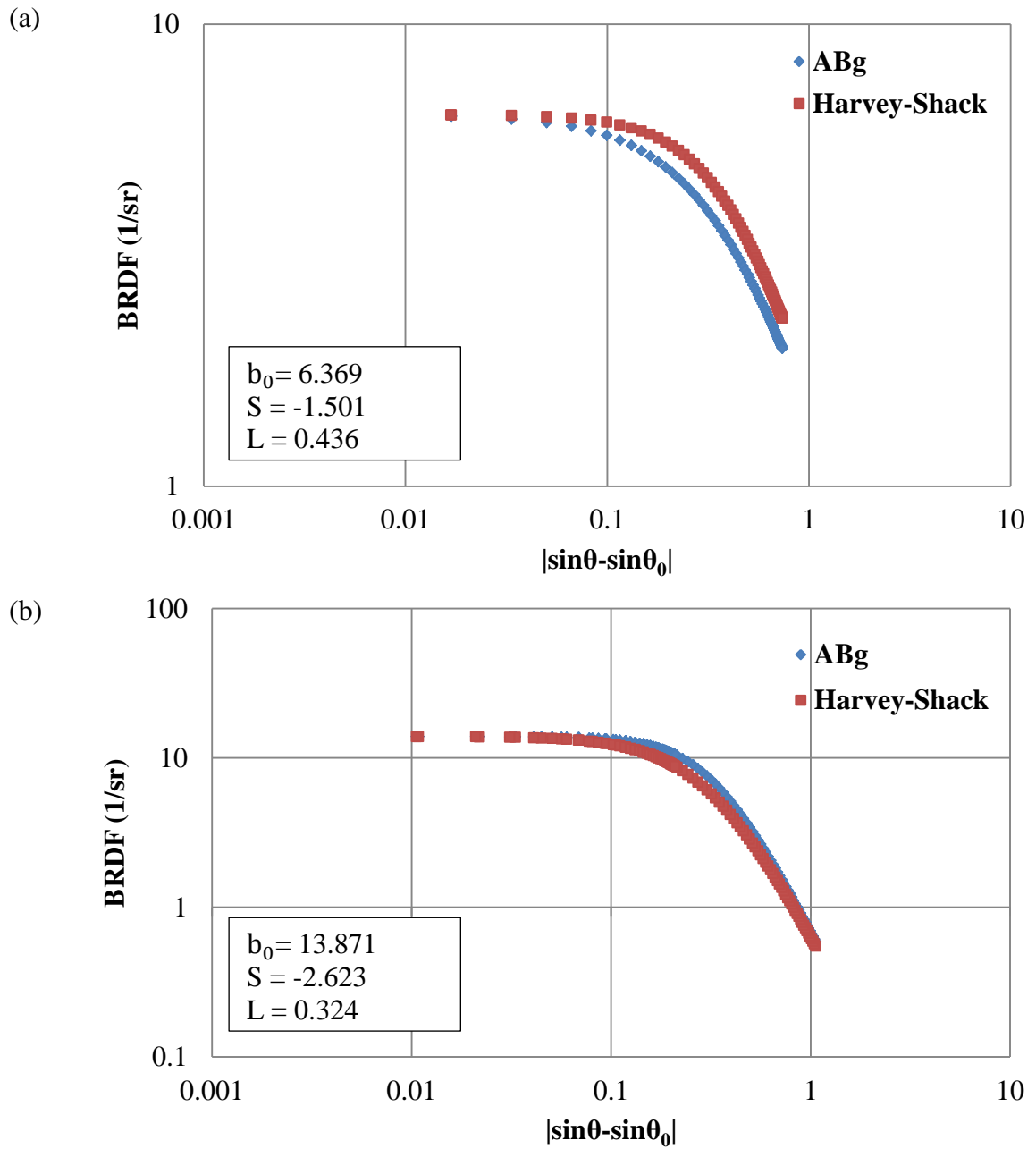


**Figure 63** Comparison of the Harvey-Shack model with the ABg model of Sample E at the (a) 15° and (b) 45° incident angles

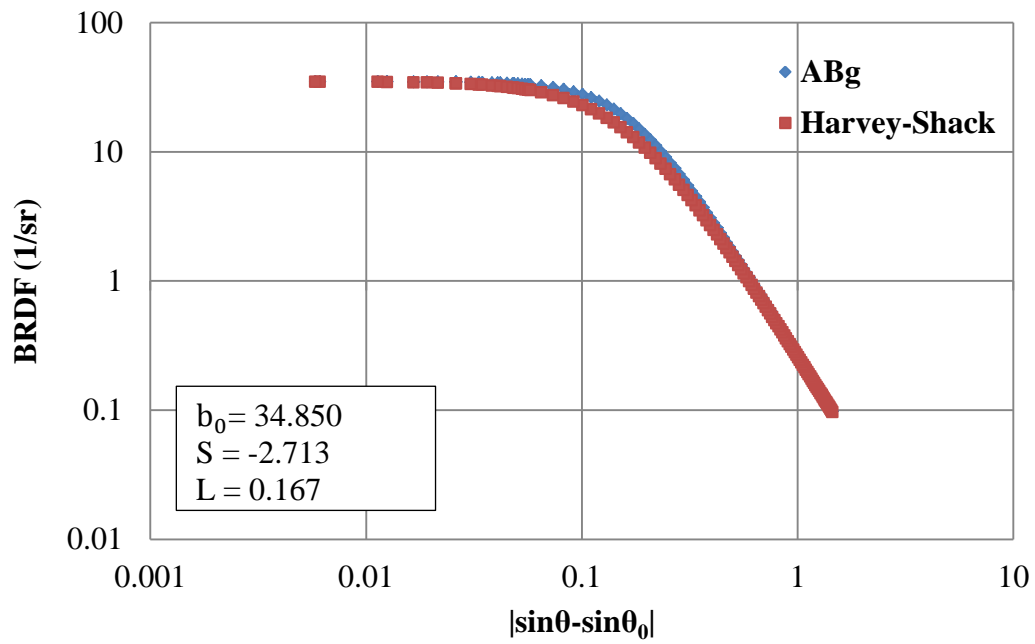


**Figure 64** Comparison of the Harvey-Shack model with the ABg model of Sample E at the 60° incident angle